

AB INITIO THEORIES OF ATOMIC SUBSYSTEMS  
IN INTERACTION WITH EXTENDED  
ENVIRONMENTS

A Dissertation

Presented to the Faculty of the Graduate School  
of Cornell University

in Partial Fulfillment of the Requirements for the Degree of  
Doctor of Philosophy

by

Jee Hye Lee

January 2013

© 2013 Jee Hye Lee  
ALL RIGHTS RESERVED

# AB INITIO THEORIES OF ATOMIC SUBSYSTEMS IN INTERACTION WITH EXTENDED ENVIRONMENTS

Jee Hye Lee, Ph.D.

Cornell University 2013

In this thesis, we present *ab initio* studies on atomic subsystems in contact with extended environments. Among a large number of systems which can be treated in the subsystem-environment framework, here we consider the two typical cases of mechanical and of electronic interaction with the environment. Specifically, we consider atomic deformations in defect-containing crystals and photo-excitation processes of solvated molecules.

In the former case, the subsystem is a group of atoms involving particular microscopic displacements, which turn out to be key ingredients in understanding structural phase transitions and glass-like low-energy excitations reported to exist in certain apparent crystalline systems. In this case, the crystal surrounding the displaced atoms makes up the the environment, which couples via effective elastic strain fields to the subsystem. The subsystem itself, then, we find can be described quite accurately by a simple model Hamiltonian which captures all of the key behaviors found in the *ab initio* calculations. This approach allows us to efficiently handle complicated environments, such as stacking faults and randomly distributed dopants, which would otherwise be impractical to study directly *ab initio*. This approach then allows us to successfully predict complex glass-like system behaviors in good agreement with experimental observations.

In the latter case of photo-excitations, we focus on non-equilibrium states

of molecules in the quasiparticle framework based on the Green's function approach within the "GW" approximation. The environment in this case is made up of the surrounding polarizable liquid molecules, which we describe in this work via one of two different approaches: the classical model of a polarizable continuum (PCM method) and the chemistry-inspired cluster expansion of microscopic polarization (a new method which we introduce here.) We show that an appropriate combination of the two embedding approaches successfully captures the environmental effect. We thus bring significant improvement to the standard PCM model in computing solvation shifts of the ionization potential, while requiring much less computational power than would direct computation with the entire environment included explicitly. In addition, our approach allows us to develop a systematic improvement over state-of-the-art PCM methods, which are highly efficient computationally. Through construction of a microscopic dielectric model for the environment based on microscopic molecular polarizations, we are able to derive a non-local dielectric description which includes short-wavelength features missing in the standard treatment of the PCM method.

## BIOGRAPHICAL SKETCH

Jeehye Lee was born on June 3, 1983 in Cheongyang, a small town of South Korea, as the eldest child of Namsook Shim and Bongho Lee. She went to the Korea Advanced Institute of Science and Technology in 2001, and there made her first step towards Physics. Her first research experience was as an undergraduate researcher studying laser modes in photonic crystals in Professor Yong-Hee Lee's group, where she learned the joy of research and then started to consider seriously becoming a physicist.

In 2005, she came to the United States to begin the Physics Ph.D. program at Cornell University. There she joined the computational physics group of Professor Tomás A. Arias and took her debut as a theoretical physicist. Her research was about theory developments and computational studies of nano-scaled systems in contact with various environments. After spending six years in the condensed matter physics, she decided to apply her skills and physical intuitions to study another physically interesting and also one of the most studied systems: Finance. She is currently working at a hedge fund company as a quantitative strategist.

To my family.

## ACKNOWLEDGEMENTS

I first thank to my family in Korea, my mom Namsook Shim and my dad Bongho Lee as well as my little brother Hyoungseok Lee, who gave me endless supports and loves from their hearts. I thank to my supervisor Professor Tomás A. Arias, who has guided me through this long journey and inspired me with his energy and brilliant research ideas. I also thank to Professor James P. Sethna and Professor Al J. Sievers for fruitful discussions and research advises.

I was lucky enough to have great colleagues, Kendra Letchworth-Weaver, Ravishankar Sundararaman and Katie Schwartz – we all know we had wonderful time together. At last, I thank to Woosong Choi, the love of my life and my soul mate.

## TABLE OF CONTENTS

Biographical Sketch . . . . .	iii
Dedication . . . . .	iv
Acknowledgements . . . . .	v
Table of Contents . . . . .	vi
List of Tables . . . . .	viii
List of Figures . . . . .	ix
<b>1 Introduction</b> . . . . .	<b>1</b>
1.1 Overview . . . . .	4
1.1.1 Structural deformations in layered complex oxide superlattices . . . . .	4
1.1.2 Two-level transitions in minimally disordered doped crystals . . . . .	5
1.1.3 Efficient modeling of electronic response functions through dielectric description of environments . . . . .	6
1.2 Theoretical backgrounds . . . . .	8
1.2.1 Density functional theory . . . . .	8
1.2.2 Quasiparticle calculation - GW approximation . . . . .	10
<b>2 Structural phase transitions in Ruddlesden-Popper phases</b> . . . . .	<b>14</b>
2.1 Introduction . . . . .	14
2.2 Computational details . . . . .	16
2.3 $\text{Sr}_2\text{TiO}_4$ , $n = 1$ phase . . . . .	19
2.4 $\text{Sr}_{n+1}\text{Ti}_n\text{O}_{3n+1}$ , $n > 1$ phase . . . . .	21
2.5 Approach to the bulk behavior . . . . .	25
2.6 Experimental signatures . . . . .	28
2.7 Conclusion . . . . .	30
<b>3 Ab Initio Identification of Two-Level States in a Minimally Disordered Crystals: Prediction of Density of Two-Level States</b> . . . . .	<b>31</b>
3.1 Introduction . . . . .	31
3.2 Material description . . . . .	34
3.3 Background . . . . .	36
3.4 Initial ab initio investigation . . . . .	38
3.5 Multiple-minima induced by external strain . . . . .	41
3.6 Di-substitutions as two-level centers . . . . .	43
3.7 Landau analysis . . . . .	47
3.8 Spectral properties of the di-substitution . . . . .	49
3.9 Statistical Analysis of Strain Distribution . . . . .	50
3.10 Conclusion . . . . .	57



<b>4</b>	<b>Efficient treatments for solvent environments in excited state calculations: GW for solvated systems</b>	<b>59</b>
4.1	Introduction . . . . .	60
4.2	Continuum environment approaches . . . . .	62
4.2.1	Overview of joint density-functional theory (JDFT) . . . . .	63
4.3	Molecular embedding methods . . . . .	65
4.4	Quasiparticle calculations within continuum embedding . . . . .	68
4.5	Cluster-expanded electronic response . . . . .	71
4.6	Test on the cluster expansion method for the electronic response function . . . . .	74
4.7	Summary . . . . .	76
<b>5</b>	<b>Application to solvated organic molecules</b>	<b>78</b>
5.1	Overview of embedded GW method . . . . .	79
5.2	Calculations . . . . .	81
5.2.1	Computational Details . . . . .	81
5.2.2	Summary of studies . . . . .	82
5.3	Environmental effects on the equilibrium state . . . . .	83
5.4	GW in vacuum . . . . .	88
5.5	GW within polarizable continuum models . . . . .	89
5.6	Molecular embedding for the excited states . . . . .	94
5.7	Analysis of the solvent response function . . . . .	97
5.8	Summary . . . . .	103
<b>6</b>	<b>Summary/Future Works</b>	<b>105</b>
	<b>Bibliography</b>	<b>109</b>
<b>A</b>	<b>Two-level states Hamiltonian construction</b>	<b>116</b>
<b>B</b>	<b>Frequency Integral of GW method</b>	<b>121</b>

## LIST OF TABLES

2.1	<i>Ab initio</i> prediction for critical strain $\epsilon_c$ of each RP- <i>n</i> phases . . .	23
2.2	Ginzburg-landan expansion coefficients . . . . .	27
3.1	Bulk properties computed within various theories . . . . .	36
3.2	Landau expansion coefficients . . . . .	48
4.1	IP and HOMO-LUMO gap for five H <sub>2</sub> O cluster computed within DFT and COHSEX . . . . .	76
5.1	DFT results for IP computed within various embedding approaches . . . . .	87
5.2	IP of molecules in gaseous phase computed within DFT and GW	88
5.3	IP of solvated molecules computed within GW with continuum embedding . . . . .	91
5.4	IP shifts computed within GW under continuum embedding . .	93
5.5	IP of H <sub>2</sub> O molecule computed either within DFT or GW under various embedding approaches . . . . .	96
5.6	IP shift of H <sub>2</sub> O molecule computed either within DFT or GW under various embedding approaches . . . . .	96
5.7	IP shifts computed within molecular, continuum, and a non-local dielectric model embedding . . . . .	102

## LIST OF FIGURES

2.1	Schematic figure of $n = 2$ RP phase . . . . .	15
2.2	Structural phase diagram of RP-n phase . . . . .	18
2.3	Rotational angles and transition energies versus epitaxial strain . . . . .	20
2.4	Schematic view of deformation near stacking faults . . . . .	22
2.5	<i>Ab initio</i> and model predictions of layer-dependent rotation angles . . . . .	23
2.6	Critical strain $\epsilon_c$ for various RP phases . . . . .	24
2.7	Model prediction of rotation angles . . . . .	28
2.8	<i>Ab initio</i> prediction of out-of-plane lattice constant change under epitaxial strain . . . . .	29
3.1	Measured TLS optical density of states . . . . .	37
3.2	Schematic sketch of two-level states . . . . .	37
3.3	Local minima configurations for nine defect cell . . . . .	40
3.4	Local minima configurations in bulk BaF <sub>2</sub> under strain . . . . .	42
3.5	Local minima configurations of di-defect cell . . . . .	44
3.6	Atomic displacements and transition energies under various strain . . . . .	45
3.7	Energy asymmetry under tensile strain . . . . .	46
3.8	TLS excitation energies under various strains . . . . .	51
3.9	Interaction energy of substitutions . . . . .	53
3.10	Cumulative probability distribution of normal strain . . . . .	53
3.11	Cumulative probability distribution of shear strain . . . . .	54
3.12	Calculated TLS density . . . . .	56
4.1	Configuration of five H <sub>2</sub> O cluster . . . . .	75
5.1	Electrostatic potential induced by continuum environment . . . . .	85
5.2	Coupling potential between solute and solvent under orbital-free embedding . . . . .	86
5.3	Screened potential fluctuations for H <sub>2</sub> O molecule in gaseous phase and solvated within continuum embedding . . . . .	90
5.4	Screened Coulomb potential of solvated H <sub>2</sub> O calculated within molecular embedding approach . . . . .	95
5.5	Comparison of solvent response functions (weighted average) computed under continuum or molecular embedding approach . . . . .	99
5.6	Comparison of solvent response functions (diagonal components) computed under continuum or molecular embedding approach . . . . .	100
5.7	Enlarged view of solvent response functions (diagonal components) computed under continuum or molecular embedding approach . . . . .	101
A.1	Contour plot of tunneling barrier under anisotropic normal strain . . . . .	119
A.2	Contour plot of asymmetry under anisotropic shear strain . . . . .	120

B.1	Screened Coulomb energy computed at various imaginary frequency . . . . .	125
-----	---	-----

## CHAPTER 1

### INTRODUCTION

A desire to understand phenomena in nature and the physics behind them has existed since the beginning of science in ancient Greek society. In fact, the origin of the word “atom” comes from the Greek word “atomos,” which means “indivisible,” as the concept of an indivisible unit of matter was first proposed by the Greek philosophers. The human ambition to investigate nature beyond our eyes’ ability to see has led to the development of measurement tools – for instance, microscopy and spectroscopy – which opened the door to science at, or even beyond, the scale of atoms and electrons. The deeper understanding of nature, made possible by the evolution of technology, has changed and will continue to change our everyday lives: the foundation of all electronic devices is the quantum mechanics theory of semiconductors and electron transport; wireless networks and remote controlling devices are based on our understanding of electromagnetic waves; ongoing studies on sustainable energy resources, such as fuel cells and solar cells, involve investigations of chemical compounds and their reaction mechanisms.

As the theoretical counterpart to experimental measurements, *ab initio* simulation has arisen as a powerful alternative to explore the land of new phenomena and materials. “*Ab initio*” means “from the beginning” in Latin and usually refers to computational techniques to solve many-body problems of interacting electrons without any parameter-fitting. A substantial number of *ab initio* theories have been developed, such as quantum Monte Carlo[87, 30] and Hartree-Fock[97, 6], to name a few, among which density functional theory[44] has been an especially popular choice for its relatively low computational costs

and its ability to study extended systems. Within the framework introduced by Kohn and Sham[55], the interaction between electrons in density functional theory is characterized by an effective potential, and the many-body problem of interacting electrons is reduced to the single particle Schrodinger's equation. With the development of key techniques for evaluating the effective potential, such as pseudopotentials[84, 18] and approximate exchange-correlation functionals[79, 80, 9], density-functional theory requires lower computational costs[63] than any other *ab initio* method and shows excellent performance in computing various material properties, ranging from electronic band structures to elastic moduli.

Although such "computer experiments" have been successful in studying a vast number of physical systems – topological insulators[111, 112], graphene[59], glasses[20, 90], and DNA chains[99], to name a few interesting examples – the rapid scaling of the computational cost with system size is still a barrier to studying real-world examples. Even for density functional theory, which is considered the most effective among the *ab initio* methods, the computational costs become prohibitive for systems containing more than about one thousand electrons. Consequently, the application of *ab initio* theories is limited mostly to systems as small as atomic clusters and molecules, or to purely periodic systems with relatively small unit cells. For large systems containing more than a thousand atoms, which are considered infinitesimal on an experimental scale, preferable choices for simulations are empirical methods such as molecular dynamics[10, 66] or Monte Carlo methods, which rely on interatomic potential models and thus miss quantum-level effects.

Recently there have been a number of theoretical attempts to overcome this

technical obstacle, including the linear scaling method[96, 98] with the use of sparse density matrices and localized basis sets, and hybridization of classical models with *ab initio* simulations. In this thesis, we focus on the latter approach, which can be implemented in various ways, depending upon how the hybridization is implemented. For example, a classical model can be constructed based on *ab initio* results, with this model applied to the simulation of much larger systems. Or, one could employ a multiscale modeling technique in which the macroscopic and microscopic features, representing two subsystems (one containing relatively few atoms capturing the key microscopic features, and one containing the “environment” of the microscopic system), with the larger subsystem treated with an empirical model and the microscopic subsystem treated with an *ab initio* theory. An example of the former approach is an *ab initio*-based pair potential model[93, 28], which is often employed in molecular dynamic simulations as a way to mimic *ab initio* calculations for large systems. The latter approach has been widely used in a substantial number of quantum chemistry calculations for systems dissolved in liquid environments, which are characterized by the dielectric parameter field known as the polarizable continuum model[22, 29, 103].

In this thesis, we explore atomic subsystems in contact with extended environments under various circumstances – including defects interacting with strain fluctuations and molecules in liquid environments – all of which are difficult to treat with the standard, straight-forward *ab initio* calculations because of the numbers of atoms involved. In the succeeding chapters, we demonstrate the applicability of this methods-hybridization approach to a wide variety of systems: we consider crystalline structures, disordered crystals, and liquid systems, while studying a range of phenomena including elastic and electronic in-

teractions, for both ground- and excited-state properties.

## 1.1 Overview

### 1.1.1 Structural deformations in layered complex oxide superlattices

In the second chapter of this thesis, we explore strained complex oxide crystals with periodically repeated planar defects. Complex oxides, which are composed of alternate layering of transition metal oxide planes, exhibit a wide variety of superlattice structures associated with rich material properties such as ferroelectricity and superconductivity. A substantial part of these superlattices still remain unexplored on the theory side because of the complicated structural phase diagrams arising from distinct orderings of oxide layers. We choose a simple prototype structure of such superlattices, the Ruddlesden-Popper phase (RP- $n$ ), and propose a research method to systematically study the effect of superlattice interfaces on properties of complex oxides. The Ruddlesden-Popper phase, expressed in the chemical formula  $A_{n+1}B_nO_{3n+1}$ , has a whole series of structures with different phase numbers  $n$  ranging from 0 (A-oxide) to  $\infty$  (bulk ABO perovskite structure). This unique series of structures represents a physical interpolation between layered superlattices and bulk structures, for which we find an equation of the state within our effective model.

Specifically, in this case we study octahedral deformations in various RP- $n$  phases of strontium titanate under epitaxial strain. Based on the *ab initio* simulation results, we develop a model Landau Hamiltonian to describe the struc-



tural phase transition accounting for both epitaxial strains and interactions between superlattice interfaces. In the continuum limit, we obtain from the model Hamiltonian an analytic expression of the structural phase boundary, which is consistent with our existing *ab initio* data and which allows extrapolation beyond the simulation limit through to the bulk phase.

### **1.1.2 Two-level transitions in minimally disordered doped crystals**

In the third chapter, we explore the quantum-tunneling of atomic displacements in disordered crystals with randomly distributed defects. The study of such disordered crystals is suggested by spectroscopic measurements of materials showing the presence of a two-level systems, a key ingredient in explaining the properties of glasses. Such two-level states (formed by multiple local minima in the potential energy surface of the system) result, for example, in finite entropy of glassy systems at zero temperature. Although the concept of such two-level systems has been successful in explaining distinctive thermal properties of glass materials, the *ab initio* investigation of two-level states, to date, has been done for only a few glassy systems, with analyses relying only upon *qualitative* signatures of the multiple minima.

Here, we present a detailed *quantitative* investigation of two-level states with full *ab initio* calculations of a candidate glassy fluorite system. We considered this type of doped crystal because it is mildly disordered (no topological disorder in the lattice, only substitutional disorder), so that the phase space to be explored is relatively small compared to more traditional glassy systems with

amorphous structures.

Similar to our aforementioned work on Ruddlesden-Popper phases of complex oxides, we construct a Landau Hamiltonian based on *ab initio* simulation results of the local atomic structure of defects subject to local chemical strains, showing that relatively small fluctuations in local strain induce two-level systems in the target fluorite system. Building on this Hamiltonian, we then develop a statistical model to reproduce the effects of fluctuations in local chemical strain on the resulting two-level systems. In this model, we compute the long-range components of chemical strains with an interatomic potential model, with the total strain computed as a superposition of strains from randomly distributed chemical dopants. This methods-hybridization treatment of the *ab initio* theory, the statistical model and the interatomic potential model successfully predicts the spectral properties of the target system in excellent agreement with spectroscopy measurements.

### **1.1.3 Efficient modeling of electronic response functions through dielectric description of environments**

In the last two chapters of this thesis, we explore excited states of molecular systems in contact with dielectric environments with the many-body perturbation theory (MBPT) GW method, combined with effective dielectric models to characterize surrounding liquid solvent environments. In contrast to the two previous studies described above, in which the coupling to the environment is primarily *elastic* in nature, the final two research chapters focus on *electrostatic* coupling in the context of liquid solvent environments.

For these studies, we consider organic molecules dissolved in liquid water because such systems represent prototypical solvated systems and are common subjects for excited-state calculations. The present state-of-the-art for the treatment of such systems is the “polarizable continuum model”, a mean-field characterization of the environmental screening effect which is completely devoid of atomic details. To date, all previous work with this continuum model have employed excited state methods based on fluctuations in the total charge densities of the solvated molecule (e.g., time-dependent DFT [TDDFT]), and no attempt has been made to our knowledge to explore its use with more detailed excited-state methods.

In this work, we take the polarizable continuum method (PCM) beyond TDDFT and explore its use with Green’s function based description for excited states within the GW approximation. We also go beyond PCM and explore the chemistry-inspired molecular response model for the environment. We then demonstrate the reliability of the continuum model combined with the GW method by comparing the results with these two solvent models, and show how one can improve significantly upon the PCM by fitting the high-frequency (low wavelength) tail of its response function to that of the molecular response model.

## 1.2 Theoretical backgrounds

### 1.2.1 Density functional theory

Density functional theory is one of the most widely used electronic structure methods for solving many-body problems for interacting systems of electrons. As opposed to other methods, such as Quantum Monte Carlo[87, 30] or the quantum-chemistry coupled cluster method (CC)[85, 54], most of which compute the many-body wave functions explicitly and thus are relatively expensive, density functional theory employs an auxiliary *single-particle* Hamiltonian to solve for the ground-state energy and the electron density of the interacting system.

The modern formulation of the density functional theory is based on the two famous results[63], the Hohenberg-Kohn theorem and the Kohn-Sham *ansatz*. P. Hohenberg and W. Kohn, in their paper[44] written in 1964, showed that the electron density is the fundamental variable and sufficient to determine all the ground-state properties of a given system. The Hohenberg-Kohn theorem states the following.

(I) For any system of interacting particles, the full many-body ground state is a unique functional of the ground state electron density  $n(r)$ .

(II) There always exists an energy functional  $E[n]$  of the electron density whose global minimum gives the exact ground-state energy and electron density of the interacting system.

(III) The energy functional has the form,

$$E[n] = G[n] + \int dr^3 V(r)n(r) + \frac{1}{2} \int \int dr^3 dr'^3 \frac{n(r)n(r')}{|r - r'|}, \quad (1.1)$$

where  $G[n]$  is a universal functional (completely independent of the physics or chemistry of the system under study, metal, insulator, semiconductor, molecule, etc.) that describes the internal energies of the interacting electrons.

The Hohenberg-Kohn theorem by itself, however, does not provide a direct way to study system properties by only looking at the electron density. Although the electron density is a sufficient variable to describe the ground state of any interacting system, the explicit form of the energy functional is not known in terms of the electron density. The kinetic energy, for instance, can be only determined in terms of the wave functions, derivatives of wave functions in particular, and it follows immediately that the exact functional would not be expressible in terms of the electron density in any closed form.

Such deficiencies in the density-based description were overcome by W. Kohn and L. J. Sham[55], who introduced an *ansatz* employing an auxiliary system – a system of non-interacting electrons with the same ground-state density but moving in some effective potential – which, according to the Hohenberg-Kohn theorem, guarantees an exact determination of the original ground state. In the Kohn-Sham *ansatz*, the many-body problem of the interacting particles is replaced by the single-body problem of non-interacting particles under the effective external potential  $V_{eff}$  as follows,

$$\left( -\frac{1}{2}\nabla^2 + V(r) + V_{eff}[n(r)] \right) \psi_i(r) = \epsilon_i \psi_i(r), \quad n(r) = \sum_i |\psi_i(r)|^2$$

$$V_{eff}[n(r)] = V_{xc}[n(r)] + \int dr'^3 \frac{n(r')}{|r - r'|} \quad (1.2)$$

where  $V_{xc}[n(r)]$  is the exchange-correlation potential reproducing the many-body interaction in the auxiliary system. By solving these equations self-consistently, one obtains the ground-state electron density and energy of the original interacting system, with an accuracy limited only by any approxima-

tions made in expressing the exchange-correlation potential in some closed form to enable practical calculations.

## 1.2.2 Quasiparticle calculation - GW approximation

In spite of its success in computing the ground state properties for a vast ranges of material, density-functional theory, by its very construction as a ground-state theory, gives no direct information about excited states. Nonetheless, some properties, such as band-structures (which are, formally speaking, single-particle excitations) are often computed within density-functional theory with surprisingly good results, but with certain well known failures, such as the band gap (HOMO-LUMO gap in the case of molecules). Indeed, the Kohn-Sham band gap in the local density approximation is typically 30-50% underestimated with respect to the experimental values, as the exchange-correlation potential  $V_{xc}$  in DFT is not designed to compute such single-particle excitations.

As an effort to overcome such shortcomings of DFT, the quasiparticle formalism based on the single-particle Green's function, as formulated by Hedin[40] and Hedin and Lundqvist[41], has been proposed as a promising candidate method to capture the physics underlying electronic excitations. The key quantity in the calculation of quasiparticle energies within this framework is the non-local energy-dependent operator  $\Sigma(r, r'; \omega)$  representing the self-energy of the particle as it interacts with the perturbation introduced by itself. Within Hedin and Lundqvist's formulation, this quantity then enters into the following quasiparticle equation[45],

$$(T + V_{ext} + V_H)\psi_{nk}(r) + \int dr' \Sigma(r, r'; E_{nk})\psi_{nk}(r') = E_{nk}\psi_{nk}(r), \quad (1.3)$$

where  $T$  is the kinetic energy operator,  $V_{ext}$  is the external potential,  $V_H$  is the Coulomb potential, and  $\psi_{nk}$  and  $\epsilon_{nk}$  represent the quasiparticle states and energies predicted by their framework.

Evaluation of the self-energy operator  $\Sigma$ , which contains the exchange-correlation effects among electrons, is the central difficulty in quasiparticle calculations. The common approximation for the self-energy operator is to simply expand  $\Sigma$  as a series in the *screened* Coulomb interaction  $W$ . (Using the screened interaction is critical here to make the expansion useful.) Taking the leading term, which is given by Hedin as the product of the single particle Green's function  $G$  and the screened Coulomb interaction  $W$ , then gives the so-called "GW" approximation,

$$\Sigma(r, r'; \omega) = i \int \frac{d\omega'}{2\pi} e^{-i\eta\omega'} G(r, r'; \omega - \omega') W(r, r'; \omega'), \quad (1.4)$$

where  $\eta = 0^+$ , and "GW" simply refers to the two terms making up the product.

Hybertsen and Louie[45] developed practical evaluation schemes for the self-energy operator in the GW approximation and computed the quasiparticle states for a vast range of crystals, showing excellent agreements with the experimental observations. The key approximations taken in these evaluation schemes are as follows. First, (1) the single particle Green's function is evaluated using the following form in the Lehmann's representation

$$G(r, r'; E) = \sum_{nk} \frac{\psi_{nk}(r)\psi_{nk}^*(r')}{E - \epsilon_{nk} - i\eta_{nk}}, \quad (1.5)$$

where  $\psi_{nk}(r)$  is approximated as the Kohn-Sham wave function from a DFT calculation,  $\epsilon_{nk}$  is the corresponding Kohn-Sham eigenvalue, and  $\eta_{nk}$  is an infinitesimal number with sign depending on the band's occupancy. Next, (2) the screened interaction  $W$  is constructed within the random-phase approximation

(RPA) in the form,

$$W = (1 - V_c \chi)^{-1} V_c, \quad (1.6)$$

where  $V_c(r, r') = 1/|r - r'|$  is bare Coulomb kernel, and the charge-density response function  $\chi$  is evaluated as the independent particle polarizability,

$$\chi(r, r'; \omega) = 2 \sum_{cv} \frac{\psi_c^*(r) \psi_v(r) \psi_c(r') \psi_v^*(r')}{\epsilon_v - \epsilon_c - i\omega} + c.c., \quad (1.7)$$

where the  $\psi$ 's and  $\epsilon$ 's are (again) the Kohn-Sham wave functions and energies, and the subscripts  $c$  and  $v$  refer to empty ("conduction") and filled ("valence") states, respectively. These studies also observed that the true quasiparticle wave functions sufficiently resemble the DFT wave functions to further simplify the quasiparticle equation in Eq. 1.3 to

$$E_{nk}^{qp} = E_{nk}^{DFT} + \langle nk | \Sigma(r, r'; E_{nk}^{qp}) | nk \rangle - \langle nk | V_{ex}^{LDA} | nk \rangle. \quad (1.8)$$

The above equations can be simplified yet further, both to help provide physical understanding and interpretation of the various terms in the equations and, as we shall see in this thesis, to provide for a computationally expedient rough approximation which is useful in evaluating different approximation schemes. Especially, assuming that the dynamic effects are negligible, *i.e.*, the polarization is solely governed by its static components, the real part of the self-energy kernel reduces to the simplified expression below,

$$\begin{aligned} \Sigma(r, r'; E) = & - \sum_{nk}^{occ} \psi_{nk}(r) \psi_{nk}^*(r') W(r, r'; \omega = 0) \\ & + \frac{1}{2} [W(r, r'; \omega = 0) - V_c(r, r')] \delta(r - r'). \end{aligned} \quad (1.9)$$

The first term above now represents the screened exchange interaction of the quasiparticle with the valence electrons, and the second term represents



the Coulomb potential due to the rearrangement of electrons, which is typically called the correlation hole. This static approximation of the GW self-energy, which is referred to as the static COHSEX (“correlation-hole, screened-exchange”) approximation, was proposed by Hybertsen and Louie[45] as a useful reference point for understanding physics of the self-energy operator. Although the static COHSEX approximation overestimates self-interaction effects, it contains the essential features such as the local screening effects, and has been widely used as a reliable simplified form of the self-energy to test the convergence of numerical techniques for use in GW calculations.

CHAPTER 2  
STRUCTURAL PHASE TRANSITIONS IN RUDDLESDEN-POPPER  
PHASES

We present a systematic *ab initio* study of anti-ferrodistortive (AFD) order in Ruddlesden-Popper (RP) phases of strontium titanate,  $\text{Sr}_{1+n}\text{Ti}_n\text{O}_{3n+1}$ , as a function of both compressive epitaxial strain and phase number  $n$ . We find all RP phases to exhibit AFD order under a significant range of strains, recovering the AFD order of bulk  $\text{SrTiO}_3$  with the scaling  $\sim 1/n^2$ . A Ginzburg-Landau Hamiltonian including inter-octahedral interactions allows us to embed the *ab initio* behavior of these crystalline units into much larger systems by coupling them to long-range elastic fields. This approach allows us to study, with *ab initio* accuracy, systems far too large to study directly with *ab initio* computational methods. We find that this embedding approach reproduces our *ab initio* results well, opening a pathway to understanding other nanostructured perovskite systems as well.

## 2.1 Introduction

Superlattices originating from various oxide perovskites are of great interest due to their rich properties. As examples,  $\text{Sr}_2\text{RuO}_4$  of the  $n = 1$  Ruddlesden-Popper (RP) family exhibits unconventional superconductivity[47], ferroelectricity in multicomponent superlattices made of different perovskites ( $\text{BaTiO}_3$ ,  $\text{SrTiO}_3$  and/or  $\text{CaTiO}_3$ ) can be tuned by controlling the mixing ratio [71, 52], and, recently, even a superconducting two-dimensional electron gas has been observed at the interface of the  $\text{SrTiO}_3/\text{LaAlO}_3$  superlattice[8].

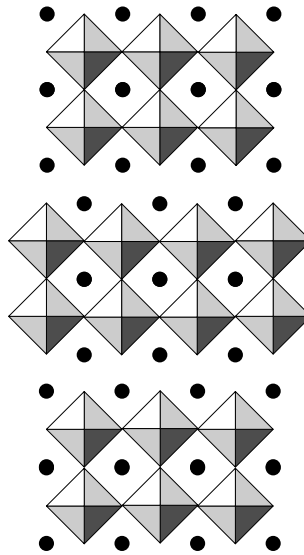


Figure 2.1: Schematic picture of  $n = 2$  RP phase ( $A_3 B_2 O_7$ ). Black circles for A sites, squares for  $BO_6$  octahedra.

The Ruddlesden-Popper series of structures,  $A_{n+1}B_nO_{3n+1} = (ABO_3)_n(AO)$  (or, “RP- $n$ ”) for  $n = 1, 2, \dots$ , is the simplest prototype of such nano-ordered superlattices, consisting of a set of AO stacking fault planes interspersed regularly between every  $n$  layers of bulk perovskite octahedra[89]. The RP- $n$  series most successfully synthesized to date is that of strontium titanate, with phases up to  $n = 5$  reported to have been grown controllably with molecular beam epitaxy(MBE)[102]. The  $n = \infty$  end member of the series, bulk  $SrTiO_3$ , is also of great interest in its own right, with highly tunable properties such as strain-switchable ferroelectricity[38], and even metallic and superconducting behavior under doping with oxygen vacancies[31, 56].

Despite its technological and scientific potential, the RP- $n$  series of strontium titanate remains relatively unexplored. Bulk  $SrTiO_3$  exhibits a rich strain-

temperature structural phase diagram including both anti-ferrodistortive (AFD) and ferroelectric (FE) ordering and various combinations thereof[58], with non-FE AFD order present at zero strain and temperature. In contrast, previous *ab initio* work has found there to be *no* AFD order at zero strain and temperature in the RP- $n$  series for  $n = 1, 2$ , with the expected bulk-like order only occurring in  $n = 3, 4, 5$  [26, 70]. However, the associated phase transitions with strain, the underlying driving forces, the scaling of the behavior with  $n$ , and the nature of the large- $n$  limit are not fully understood.

This work addresses the above open issues by employing the *ab initio* approach to study the AFD rotational transition as a function of both distance between stacking faults  $n$  and *epitaxial strain* (biaxial strain applied in the plane of the SrO stacking faults). Such epitaxial strain is now accessible experimentally, with substrates available to provide a substantial range of strains to tune the material properties of strontium-titanate structures[58, 76, 108]. For this initial study, we here focus on compressive strains, which favor AFD order with the rotation axis perpendicular to the stacking fault planes. This allows us to investigate the transition to bulk behavior with increasing  $n$ , while freeing us from having to consider the more complex configurations associated with the multiple, in-plane rotational axes favored by tensile strains.

## 2.2 Computational details

All *ab initio* calculations below employ the density-functional theory framework[77] within the local-density approximation (LDA) and represent the ionic cores with norm-conserving Kleinman-Bylander pseudopotentials[53], includ-

ing as valence orbitals Sr (4s,4p,4d,5s), Ti (3s,3p,3d,4s,4p), and O (2p). A plane-wave basis with a cutoff energy of 30 H expands the Kohn-Sham orbitals, and Monkhorst-Pack meshes[67] of  $2 \times 2 \times 2$  or  $2 \times 2 \times 1$  (for RP- $n$  structures of  $n \leq 2$  or  $n \geq 3$ , respectively) sample the Brillouin zone. Finally, the resulting energy functional is minimized by the analytically continued conjugate gradient method[5] within the DFT++ software[48].

We employ supercells composed of two bulk regions, containing  $n$  strontium titanate bulk layers each, along with two extra SrO stacking fault layers. To properly represent AFD order, each bulk layer contains two structural units of strontium titanate with in-plane lattice vectors along  $[110]$  and  $[1\bar{1}0]$  direction. To represent epitaxial strain, we fix the in-plane lattice parameter  $a$  and relax the out-of-plane lattice constant  $c$ . All calculations minimize the electronic wave functions to within  $10 \mu\text{H}$  of the Born-Oppenheimer surface, the ionic coordinates until all forces on individual atoms  $|F|$  are less than  $0.1 \text{ mH/B}$ , and the out-of-plane strain until it is determined to within  $\pm 0.2\%$  ( $1 \text{ H} \approx 27.21 \text{ eV}$ ,  $1 \text{ B} \approx 0.0529 \text{ nm}$ ).

With the ultimate goal of comparing *ab initio* results to experiments on epitaxially strained thin films, we define epitaxial strains as  $\epsilon \equiv (a - a_B)/a_B$ , where  $a_B = 3.8376 \text{ \AA}$  is the equilibrium lattice constant for cubic (non-rotated) bulk  $\text{SrTiO}_3$  within our computational framework. We find that small- $n$  phases under sufficiently low compressive strains either exhibit  $00c^-$  AFD order[34] with an out-of-plane rotation axis (Ccca symmetry for  $n \geq 2$ ; Cmca for  $n = 1$ ) or remain as a high-symmetry phase (I4/mmm). To obtain reliable transition points for low- $n$  phases and to extract information about bulk  $\text{SrTiO}_3$  that can be connected directly to our results at low  $n$ , we sometimes enter regions of phase

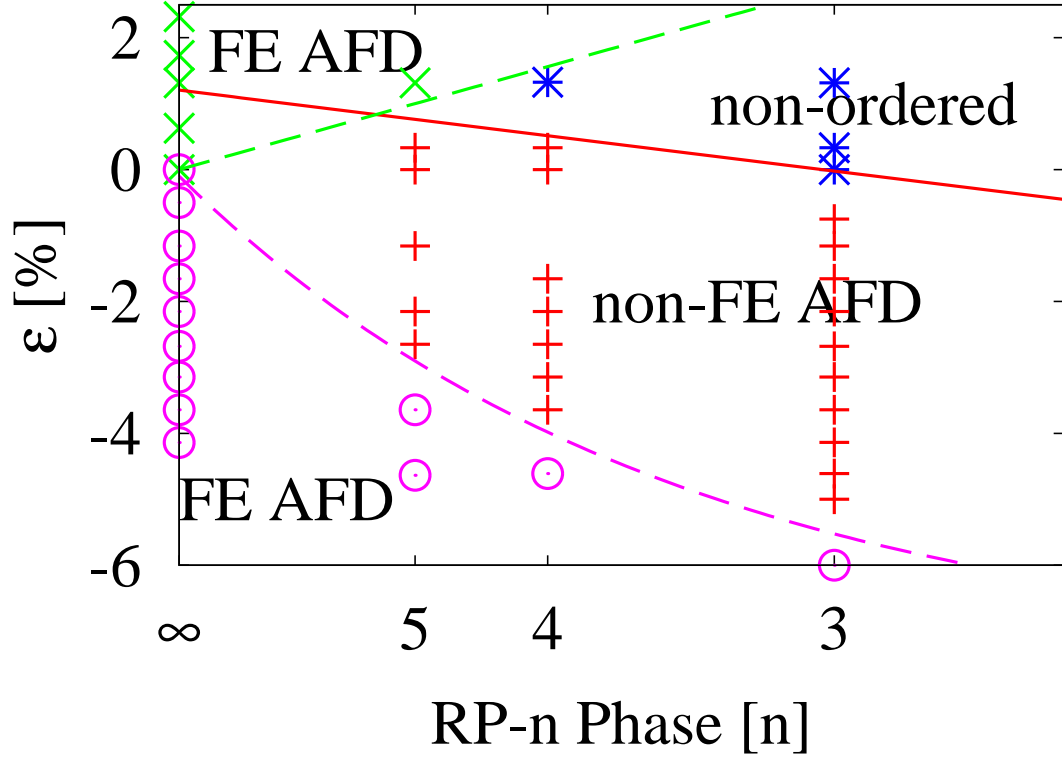


Figure 2.2: Structural phase diagram of  $\text{Sr}_{n+1}\text{Ti}_n\text{O}_{3n+1}$  as a function of epitaxial strain and  $n$ : in-plane FE AFD order ( $\times$ ), out-of-plane FE AFD order ( $\circ$ ), out-of-plane non-FE AFD order ( $+$ ), high-symmetry phase( $*$ ), non-FE AFD to high-symmetry phase boundary studied in the text (solid line), additional phase boundaries (dashed lines).

space where the material exhibits other instabilities. Figure 2.2 summarizes the phase space we considered and the phases we found in each region. Under sufficiently high compressive or tensile strains, AFD and FE orders coexist in the large- $n$  phases with the order parameters oriented along either the out-of- or in-plane directions, respectively, just as in bulk strontium titanate[58].

Concerned here only with the transition between the out-of-plane non-FE AFD phase and the high-symmetry phase, for the calculations below, we suppress FE order and in-plane AFD order by imposing both  $C_2$  and mirror symmetry about the out-of-plane direction. As shown in Figure 2.2, the ground-state

phases near the phase boundary of our interest are free of these suppressed orders, thus the imposition of the above symmetry restrictions does not affect the central conclusions below.

### 2.3 $\text{Sr}_2\text{TiO}_4$ , $n = 1$ phase

As a first look at the AFD phase transition under strain, we begin by noting that, by the symmetries of the  $00c^-$  AFD ordering, a single rotation angle  $\theta$  serves to define the state of rotation for each layer of octahedra. In a very simple picture in which the magnitude of the rotations in all layers in each bulk region are the same (as is the case for the  $n = 1, 2$  phases), we would have a single order parameter and the usual Landau form for the free energy,

$$F(\theta) = \frac{1}{2}A\theta^4 + \alpha(\epsilon - \epsilon_c)\theta^2 + F_0, \quad (2.1)$$

where both  $A$  and  $\alpha$  are positive, and  $\epsilon_c$  is the critical strain of the transition, with the well-known solution that the ordered phase obtains for  $\epsilon < \epsilon_c$ , with a nonzero rotation angle  $\theta^2(\epsilon) = \alpha(\epsilon_c - \epsilon)/A$  and an energy difference relative to the high-symmetry state ( $\theta = 0$ ) of  $\sqrt{\Delta F(\epsilon)} = \alpha(\epsilon_c - \epsilon)/\sqrt{2A}$ . Thus, the *square* of rotation angle and the *square-root* of the energy difference should both vanish linearly as  $\epsilon$  approaches  $\epsilon_c$  from below. (Here and below we regard compressive strains as  $\epsilon < 0$ .)

Figure 2.3 shows that the above Landau model agrees well with our full *ab initio* results for the  $n = 1$  RP phase, which are consistent with the classic signature of a second-order phase transition: the vanishing of the order parameter (and energy cost) at the transition point. (The space groups indicate the possibility of such a transition.) The extrapolated values for the critical strain from

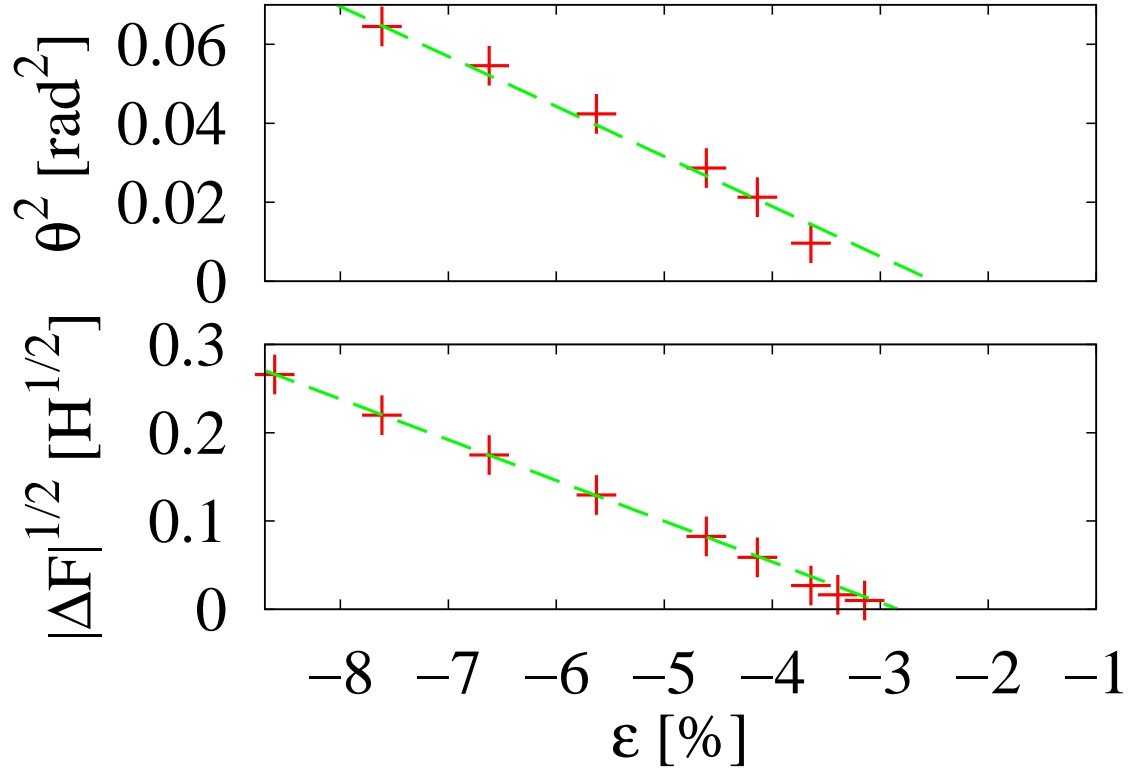


Figure 2.3: Square of rotational order parameter,  $\theta^2$ , versus epitaxial strain  $\epsilon$  (upper panel); square-root of transition energy,  $\sqrt{\Delta F}$ , versus epitaxial strain  $\epsilon$  (lower panel): *ab initio* results (crosses), linear fits (dashed lines).

the two observables,  $\theta^2$  and  $\sqrt{\Delta F}$ , are in surprisingly good agreement for such a simple model, -2.2% and -2.8%, respectively. In either case, it is clear that the critical strain is significantly below zero, consistent with the lack of observation of AFD rotational order in the  $n = 1$  phase near zero strain in previous *ab initio* work[26]. As we now show, the critical strain passes through zero and becomes positive with increasing  $n$ , eventually approaching a value associated with bulk SrTiO<sub>3</sub>.



## 2.4 $\text{Sr}_{n+1}\text{Ti}_n\text{O}_{3n+1}$ , $n > 1$ phase

For  $n > 1$ , multiple perovskite layers exist between faults and different rotation angles become possible for each layer (except for the  $n = 2$  phase where, by symmetry, the two layers have exactly opposite rotation angles). Figure 2.5 displays the rotation angles in each layer for the  $n = 5$  phase at zero strain. These data exhibit a general trend we see in all of our data, namely that the rotation angles are smaller near the SrO stacking faults and approach the expected bulk value toward the center of the bulk regions. Associated with this, we find an enhanced stretching of the octahedra neighboring the stacking faults (see Figure 2.4), resulting in rumpling of the SrO layers. We also find off-center motion of the titanium ions of these octahedra toward the fault layers such that each region of bulk material, and thus the entire structure, exhibits no net ionic electric dipole moment. This suggests that near the SrO stacking faults the boundary octahedra prefer stretching and formation of an ionic electric dipole moment over rotation as a way to relieve compressive stress, ultimately suppressing the rotational instability near the faults.

To locate the AFD transition, for the order parameter  $\theta$ , we take the rotation angle of one of the central one or two perovskite layers, and extrapolate the linear behavior of  $\theta^2$  (which shows less numerical scatter than that for  $\sqrt{\Delta F}$ ), identifying the horizontal intercept as the critical strain[1]. Figure 2.6 displays the resulting critical strains for  $n \geq 2$  (and bulk strontium titanate,  $n = \infty$ , with the same symmetry constraints described above to lock in non-FE AFD order near the critical point) as a function of  $1/n^2$ . With increasing  $n$ , the critical strain steadily increases toward the bulk value as the RP- $n$  phases become more like bulk  $\text{SrTiO}_3$ . The *positive* critical strain for  $n \geq 3$  establishes that AFD order

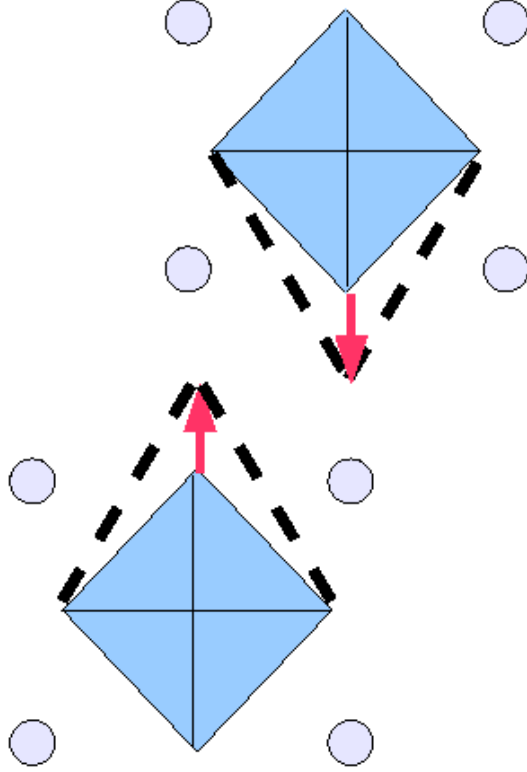


Figure 2.4: Schematic view of octahedral deformation near the stacking faults. Arrows refer to displacement of the oxygen atoms relative to the equilibrium positions.

would exist for  $n \geq 3$  phases when grown on a bulk strontium titanate substrate ( $\epsilon = 0\%$ ). The *negative* values for  $n = 1$  and  $n = 2$  are consistent with, and explain, the lack of observation of AFD order at zero epitaxial strain in previous *ab initio* studies for the low  $n$  phases[26, 70]. Finally, the clear linear behavior in the plot indicates that the critical strain approaches the bulk value as  $1/n^2$ .

We now show that a relatively simple, modulated Ginzburg-Landau Hamiltonian captures well the nature of the second-order transition suggested by the *ab initio* calculations. We construct a modulated Ginzburg-Landau free-energy model by including both inter-octahedral interactions and a spatially-

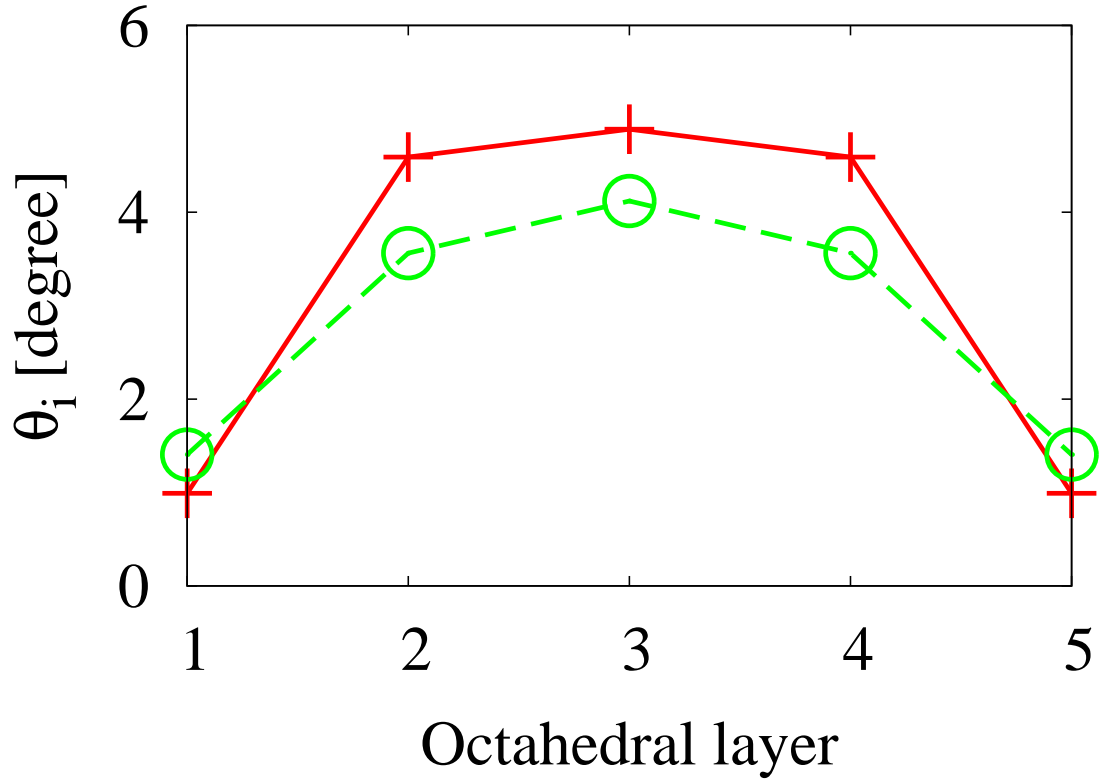


Figure 2.5: *Ab initio* (+) and Ginzburg-Landau model (o) results for layer-dependent rotation angles  $\theta_i$  versus layer position for the  $n = 5$  phase at  $\epsilon = 0.0\%$ . Lines in upper panel are guides to the eyes.

Table 2.1: Critical strain  $\epsilon_c$  of each RP- $n$  phase evaluated with the *ab initio* simulation. Data from  $n = 2$  to  $n = \infty$  are presented in Figure 2.6

Phase number $n$	Critical Strain(%)
1	$-2.83 \pm 0.01$
2	$-1.63 \pm 0.07$
3	$0.13 \pm 0.06$
4	$0.50 \pm 0.06$
5	$0.81 \pm 0.17$
$\infty$	$1.09 \pm 0.08$

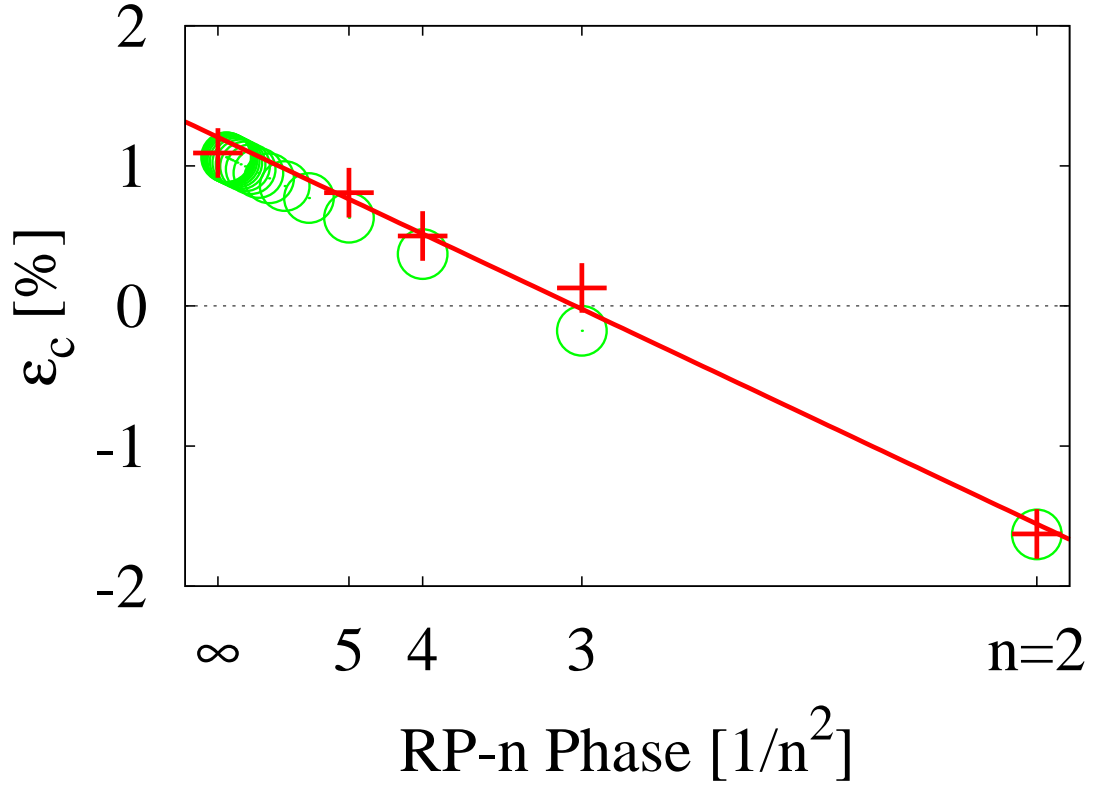


Figure 2.6: Critical strain  $\epsilon_c$  versus *inverse-square* of RP phase number  $n$ ; crosses are *ab initio* data, circles are eigenvalues of constructed Hessian in Eq. 2.3, solid line is best fit to *ab initio* data.

dependent tendency toward rotational instability,

$$F(\{\theta_i\}) = \sum_i \left\{ \frac{1}{2} A \theta_i^4 + \alpha (\epsilon - \epsilon_i) \theta_i^2 + \beta (\theta_i + \theta_{i-1})^2 \right\}, \quad (2.2)$$

where  $\theta_i$  is the octahedral rotation angle of the  $i$ -th layer,  $A$  and  $\alpha$  are defined as above (Eq. 2.1),  $\epsilon_i$  is an effective critical strain for the  $i$ -th layer. The third, inter-layer, term imposes the alternating sign ordering of the  $\theta_i$  associated with the  $00c^-$  order. This term ultimately becomes  $(\partial\theta/\partial x)^2$  in the continuum limit, as often appears in theories of twin boundaries[7]. To reflect the lessened tendency towards rotation at the interfaces,  $\epsilon_i$  should have more negative values near the stacking faults, eventually approaching the value for bulk SrTiO<sub>3</sub>  $\epsilon_c(n = \infty)$  in the center of the bulk regions. In this work, we take  $\epsilon_i$  to be the bulk value  $\epsilon_c(\infty)$  for all layers  $i$  except those neighboring the stacking faults, for which we

will take a different value,  $\epsilon_i = \tilde{\epsilon}$ , to be determined below. Reflecting these assumptions about  $\epsilon_c(n)$ , the Hessian of the free energy form in Eq. 2.1 near critical point is written as following:

$$H = \begin{pmatrix} \alpha(\epsilon - \tilde{\epsilon}) + \beta & \beta & 0 & \dots & & & & \\ \beta & \alpha(\epsilon - \epsilon_c(\infty)) + 2\beta & \beta & 0 & \dots & & & \\ 0 & \beta & \vdots & \vdots & \vdots & \dots & & \\ \vdots & \vdots & \vdots & \vdots & \vdots & \vdots & & \\ \dots & \dots & \dots & 0 & \beta & \alpha(\epsilon - \tilde{\epsilon}) + \beta & & \end{pmatrix}. \quad (2.3)$$

The standard stability analysis for this free energy is that there will be a second-order phase transition when the Hessian, evaluated at  $\theta_i = 0$  for all  $i$ , ceases to be positive definite.

## 2.5 Approach to the bulk behavior

To begin our analysis of the above free-energy form, we consider the approach to the bulk behavior. We first redefine our order parameter as the layer-dependent rotation angle,  $\tilde{\theta}_i \equiv (-1)^i \theta_i$ , following the  $00c^-$  order. Then near the center of bulk region the Hessian is expressed as

$$H = \begin{pmatrix} \vdots & \vdots & \vdots & \vdots & \vdots & \vdots & \vdots \\ \dots & -\beta & \alpha(\epsilon - \epsilon_c(\infty)) + 2\beta & -\beta & \dots & & \\ & \dots & -\beta & \alpha(\epsilon - \epsilon_c(\infty)) + 2\beta & -\beta & \dots & \\ \vdots & \vdots & \vdots & \vdots & \vdots & \vdots & \vdots \end{pmatrix}, \quad (2.4)$$

and at the continuum limit,

$$H\theta(x) = \alpha(\epsilon - \epsilon_c(\infty))\theta(x) - d^2\beta/\partial^2\theta/\partial x^2, \quad (2.5)$$

where  $\epsilon$  retains its meaning as the applied strain,  $d$  is the distance between adjacent layers and  $x$  is the position within the bulk region along the  $c$ -axis. Here, the layer-dependent rotation angle  $\tilde{\theta}_i$  has now become the smooth function  $\theta(x)$ . Finally, in passing to the continuum limit, there is a boundary condition associated with the interfaces,  $\partial F/\partial x = 0$  for  $x = 0, nd$ , which leads us to

$$\alpha(\epsilon_c(\infty) - \tilde{\epsilon})\theta(x) = d\beta\partial\theta/\partial x. \quad (2.6)$$

The critical point where this continuum Hessian ceases to be positive definite corresponds to the lowest eigenvalue of the standard one-dimensional particle-in-a-box problem of quantum mechanics with a modified boundary condition. The symmetry relation  $\theta(x) = \theta(nd - x)$  forces the eigenfunction to be  $\theta(x) = C \cos(kx - q/2)$ , for which the modified boundary condition becomes  $\alpha(\epsilon_c(\infty) - \tilde{\epsilon}) \cos(q/2) = d\beta k \sin(q/2)$ ,  $q = knd$ . Then the resulting critical strain is

$$\epsilon_c = \epsilon_c(\infty) - (\beta q^2)/(\alpha n^2), \quad (2.7)$$

where  $q$  satisfies the transcendental equation

$$\tan(q/2) = \alpha n (\epsilon_c(\infty) - \tilde{\epsilon}) / (\beta q), \quad (2.8)$$

whose solution approaches a constant,  $q \rightarrow \pi$ , for large  $n$ . The continuum limit thus reproduces exactly the  $1/n^2$  approach to the bulk value observed in the *ab initio* data. The slope  $\gamma$  observed in the *ab initio* data can now be identified as a combination of parameters from the Ginzburg-Landau Hamiltonian, namely  $\gamma = (\beta/\alpha)\pi^2$ .

Using the observed slope in the *ab initio* data as well as data from the bulk SrTiO<sub>3</sub> and  $n = 2$  phases, we now determine completely the parameters in the Ginzburg-Landau model. In the bulk phase, the last term of Eq. 2.2 vanishes due to the AFD order, and the analysis becomes identical to that for  $n = 1$

Table 2.2: Ginzburg-Landau expansion coefficients; the angle is measured in degree, the strain is measured in fraction (not percent) and the free energy is in hartree.

$A$ (H)	$\alpha$ (H)	$\beta$ (H)	$\epsilon_c(\infty)$	$\tilde{\epsilon}$
$1.13 \times 10^{-6}$	$2.43 \times 10^{-3}$	$2.72 \times 10^{-5}$	$1.09 \times 10^{-2}$	$-1.63 \times 10^{-2}$

phase, in which  $A$ ,  $\alpha$  and  $\epsilon_c(\infty)$  can all be determined from the linear fits to the  $\theta^2$  and  $\sqrt{\Delta F}$  versus  $\epsilon$  data. When  $n = 2$ , by symmetry, the Hamiltonian again assumes a form of Eq. 2.1, but with  $\tilde{\epsilon}$  instead of  $\epsilon_c(\infty)$ , so that we directly read off  $\tilde{\epsilon} = \epsilon_c(n = 2)$ . The final parameter remaining is  $\beta$ , which we determine from the above result for  $\gamma$  in terms of  $\beta$  and  $\alpha$ , taking  $\gamma$  from the slope of the best-fit line to the *ab initio* data (solid line in Figure 2.6).

The open circles in the Figure 2.6 represent the critical strains from eigenvalues of the above Hessian, with parameters extracted from the *ab initio* results as above. The linear behavior confirms our analytic prediction that the critical strain in the model approaches the bulk value as  $1/n^2$ . The Figure 2.5 presents an even more compelling case for the model. It compares *ab initio* and model-Hamiltonian results for a quantity not included in the parameter fitting at all, the layer-dependent rotation angles  $\theta_i$  for the  $n = 5$  RP- $n$  phase at  $\epsilon = 0\%$  strain. The agreement is impressive considering the simplicity of the model and the fact that the model is not fit to these quantities.

Figure 2.7 presents the Ginzburg-Landau simulation for rotational deformation for each RP phase, converging to that of bulk phase. From the solution above,  $\theta(x) = C \cos(kx - knd/2)$ ,  $\theta_{i\pm 1} = C \cos(kd)$ , where  $knd \rightarrow \pi$  for large enough  $n$ . thus  $\theta_{i\pm 1} = C(1 - 1/2(\pi/n)^2) = \theta_i(1 - 1/2(\pi/n)^2)$ , and the coupling term is simplified as  $(\theta_i - \theta_{i-1})^2 = \theta_i^2 \pi^4 / 4n^4$  and resulting solution to the free

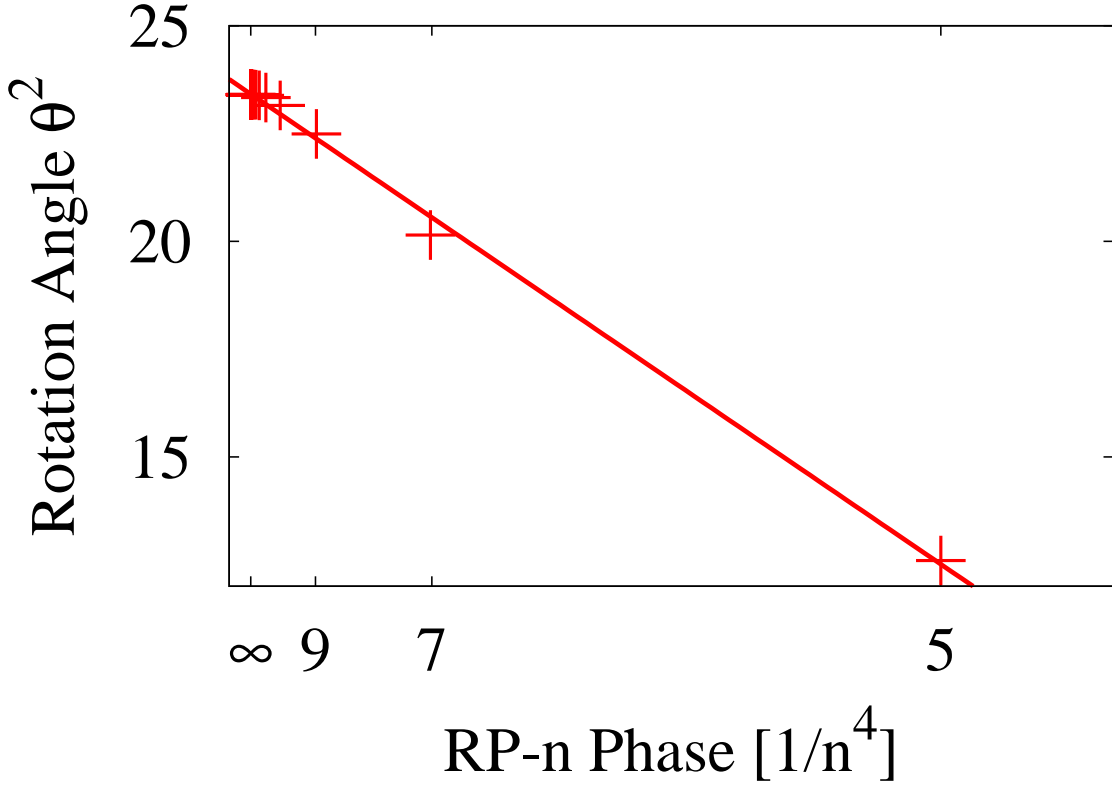


Figure 2.7: Ginzburg-Landau model results for square of rotation angles at center of the bulk region ( $i = n/2$ ) versus inverse-fourth power of phase number  $n$  at  $\epsilon = 0.0\%$ . Solid line is best fit to data.

energy Hamiltonian is

$$\theta_i^2 = \theta_B^2 - \beta(\pi/n)^4/4A. \quad (2.9)$$

Thus the deformation in RP- $n$  phase converges to that of bulk with scaling  $1/n^4$ , which is consistent with the linearity shown in the Figure 2.7.

## 2.6 Experimental signatures

In terms of an experimentally observable signature of this transition, we find that, associated with the rotational ordering, there is a significant expansion of the out-of-plane lattice constant  $c$ , by an amount which should be readily de-



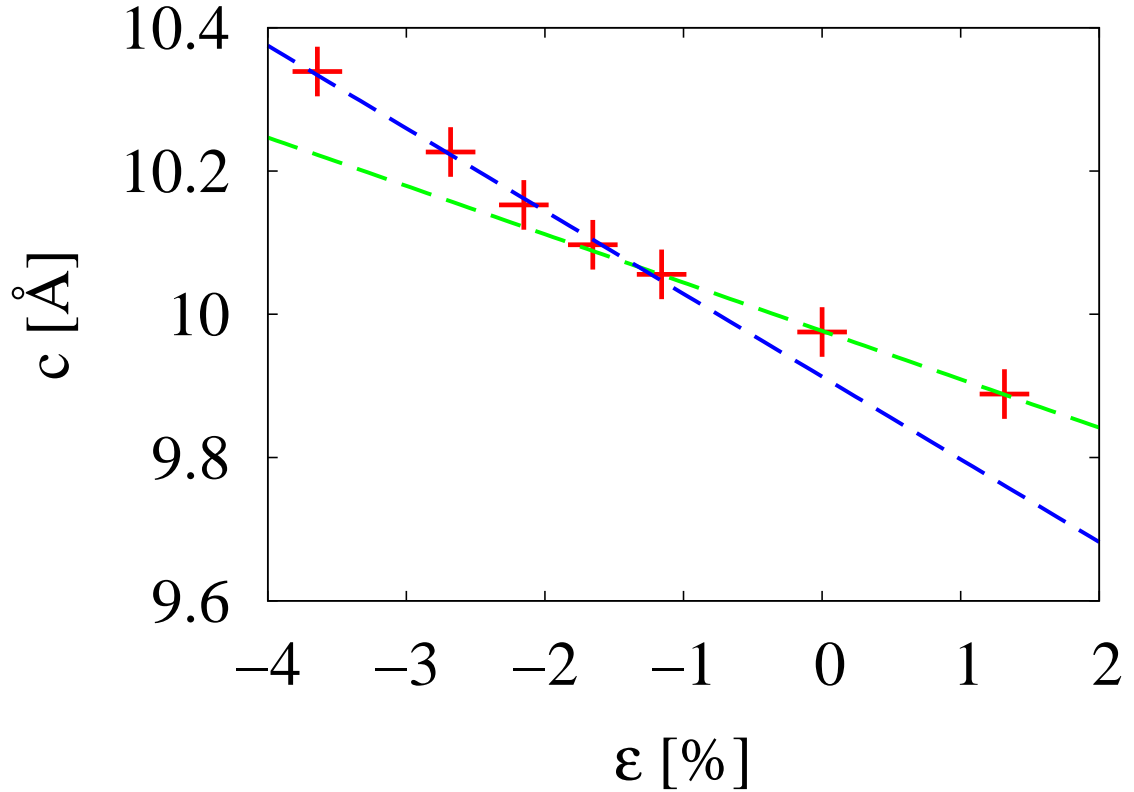


Figure 2.8: Out-of-plane lattice constant versus the biaxial strain  $\epsilon$ : *ab initio* results (+), linear fits to data on either side of the transition (dashed lines).

tectable with x-ray techniques. Figure 2.8 shows the lattice constant  $c$  of the  $n = 2$  phase as a function of  $\epsilon$  through the AFD transition point. The transition is clearly evident where the slope of the curve changes substantially between  $\epsilon = -1\%$  and  $-2\%$  strain. The lattice constant  $c$  for the AFD phase is significantly larger ( $> 0.6\%$  for strains  $\epsilon < -2.6\%$ , about  $1\%$  strain beyond the transition) than the extrapolated value from the non-rotated phase. A perhaps more practical approach is to grow various members of the RP- $n$  series on substrates of *fixed* epitaxial strain  $\epsilon$  and to observe the dependence  $c(n)$  of the out-of-plane lattice constant as a function of  $n$ , looking again for a kink at the transition point. We stress that the numerical values given here apply specifically to zero temperature.

## 2.7 Conclusion

We present a detailed *ab initio* study of the effects of strain on the rotational instability in the Ruddlesden-Popper series in strontium titanate for  $n = 1, \dots, 5$ . Our data suggest the existence of a second-order structural phase transition similar to what is seen in bulk strontium titanate, but with a critical point displaced by  $\sim 1/n^2$  from the bulk value. The key microscopic mechanism for the  $n$ -dependence is the interplay of local AFD coupling between neighboring octahedra layers with a depression of the rotational instability for octahedra neighboring the SrO stacking faults. This depression is associated with the freedom which the neighboring octahedra have to rumple the double SrO layers and form local ionic electric dipole moments. A Ginzburg-Landau free-energy model including nearest-neighbor inter-octahedral interactions, and spatially modulated to reflect the presence of stacking faults, captures the essential features of the *ab initio* results. Despite its simplicity, this model predicts even quantities to which it is not fit, such as rotation angles in the bulk regions of the RP phase. This success suggests that inclusion of inter-octahedral interactions into more general bulk Hamiltonians, particularly those with ferroelectric degrees of freedom, will be a fruitful direction to pursue in future studies of nano-structured and superlattice perovskite materials.

This work was supported by the Cornell Center for Materials Research (CCMR) under the NSF MRSEC program (DMR-0520404). The authors are grateful to Craig Fennie for *many* fruitful discussions.

## CHAPTER 3

# AB INITIO IDENTIFICATION OF TWO-LEVEL STATES IN A MINIMALLY DISORDERED CRYSTALS: PREDICTION OF DENSITY OF TWO-LEVEL STATES

Here we present an *ab initio* investigation of the nature of the two-level states in a material system observed experimentally [110] to show glassy behavior, the substitutionally mixed crystal  $\text{Ba}_{1-x}\text{Ca}_x\text{F}_2$ . Our *ab initio* approach allows us to identify the formation and the distribution of two-level states in this material. Specifically, we find these two-level states to be due to spontaneous symmetry breaking in the local structure of di-substitution defects as induced by random, local chemical strains. We then develop a modified Landau theory which allows us to couple our *ab-initio*-identified two-level centers to long-range strain fields. This embedding approach reproduces the key aspects of our *ab initio* calculations and allows us to make a prediction of the spectral density of states in very good agreement with the experiment, a feat which would otherwise require prohibitively large *ab initio* calculations.

### 3.1 Introduction

The nature of glass transitions has been a subject of great interest for a long time due to their universal characteristics. A wide range of materials, from amorphous solids to disordered crystals, exhibit glassy properties, and the origin of this universality is still debated[4]. Among many approaches to resolve the mystery, two-level states (TLS) theory[83, 3] stands as the simplest but most powerful. The TLS theory posits the existence of a plethora of local minima, *with a continuous distribution* of energy splittings, between which the system

tunnels quantum mechanically. The existence of a distribution of such tunneling centers then explains well the low temperature scaling of glassy properties: thermal conductivity, heat capacity, far infrared absorption[105], and even the quality factor of mechanical oscillators, with the distribution of center properties as the key input. More recently, the concept of a pair of levels in TLS theory has been extended to a multidimensional phase space, the  $3N + 1$  dimension hypersurface of potential energy known as the “energy landscape”[43]. These landscape frameworks have broken new ground in the quantitative analysis of low-temperature properties of glass, including the understanding of such issues as fragilities[64, 65] and relaxation processes [92].

Despite the successes of the two-level states theory described above, the identities of multiple local minima are known for only few systems [94, 73], and the connection between theoretical studies and experimental data, to date, has been made only through *qualitative* observations. *Ab initio* approaches, which have shed *quantitative* light on many subtle questions regarding defects in materials[23, 49, 106], also have been successful in predicting electronic and structural properties of glass states[91, 20, 51, 19]. Previous *ab initio* studies, however, have focused primarily on understanding glass-forming systems in the limited context of glass transitions and glass-forming dynamics because the inherent structural disorder in amorphous solids often requires large simulation cells and necessitates the exploration of large phase spaces of configurations to identify the two-level states. Consequently, *ab initio* identification of the precise nature of the two-level states, which is a key object in understanding the low-temperature properties and the universality of glass-forming systems, is still lacking for nearly all glassy systems.

Recently, a small number of substitutionally disordered crystals have been reported in experiments to exhibit low-energy excitations[110], which are thought to stem from the same origin as in glassy amorphous solids[61, 27]. These disordered crystals have minimal structural disorders and even near perfect lattice structures, making them ideal candidates for *ab initio* exploration of the nature of the two-level centers for two reasons. First, such substitutionally disordered crystals allow the study of glassy behavior without the complexity of amorphous structures. This both allows better focus on the key microscopic phenomena with the primary topological structure fixed, and allows for *ab initio* study without the need for extensive exploration of atomic configuration phase space. Second, unlike other near-crystalline glass-like materials which have been proposed with two-level systems such as rotors or off-center substitutions essentially embedded in a crystalline matrix[94, 27, 104], the reported simple substitutionally disordered crystals[110] ( $\text{Ba}_{1-x}\text{Ca}_x\text{F}_2$  and  $\text{Pb}_{1-x}\text{Ca}_x\text{F}_2$ ) do not require a complex defect-defect interaction to explain the lack of a gap in the two-level center density of states. Specifically, defects with native off-center symmetry and multiple-minima behavior inevitably have tunneling barriers between the minima and thus a finite excitation energy, which must be removed to explain a finite TLS density of states at zero energy by some mechanism, such as the defect-defect interactions studied in recent *ab initio* work[74]. Finally, the absence of native off-center displacements in the systems we study provides strong evidence that the amorphous structure itself need not be the main cause for the low-energy excitations in standard glassy materials.

This work presents an *ab initio* investigation to identify the specific nature of the two-level centers in a system where such nature is not already suspected. Specifically, we consider one of the substitutionally disordered crystals

described above:  $\text{Ba}_{1-x}\text{Ca}_x\text{F}_2$ . The results of this search lead us to identify a candidate structure for the two-level centers and the associated degrees of freedom with sufficient understanding of the underlying physics to make a prediction of the spectral density of centers in very good agreement with that observed experimentally, thereby confirming our identification of the nature of the centers in this material.

### 3.2 Material description

This work employs density-functional theory[77] with the local-density approximation (LDA) and norm-conserving Kleinman-Bylander pseudopotentials[53] to explore the nature of the two-level centers in  $\text{Ba}_{1-x}\text{Ca}_x\text{F}_2$ . We employ partial core corrections[62] to represent the ionic core of barium atoms. A plane-wave basis with a cutoff energy of 25 hartree (1 H=27.21 eV) expands the Kohn-Sham orbitals, and the Gamma point  $k = 0$  is sufficient to sample the Brillouin zone in the supercells which we employ. Increasing the k-point sampling to a  $2 \times 2 \times 2$  grid only changes bulk modulus and lattice constant by 3% and  $< 0.1\%$ , respectively.

We minimize the energy functional with the analytically continued conjugate gradient method[5] employing the DFT++ framework[48]. The simulation cell is a  $2 \times 2 \times 2$  reconstruction of the basic cubic unit cell, and contains 96 atoms in total. We measure all lattice strains relative to the lattice constant of bulk  $\text{BaF}_2$  as computed within our framework, 6.08 Å, ignoring any global lattice changes due to calcium dopants. All calculations minimize the electronic functions to within 10  $\mu\text{H}$  of the Born-Oppenheimer surface, and the ionic coordinates until

the total energy converges within 0.1 mH.

Our study also includes some exploratory works which we perform with an interatomic potential model for practical reasons. The use of this potential model is limited primarily to studying the distribution of local chemical strains, which involve long-range elastic interactions, are hence not particularly sensitive to electronic behavior, and thus can be estimated by interatomic potentials with reasonable confidence. We also employ the model to establish the basic symmetries and analytic structure of a Landau Hamiltonian for our candidate two-level centers (neither of which depend on the detailed nature of the interatomic forces), but then determine the values of all parameters for that Hamiltonian through *ab initio* calculations.

The specific interatomic model we employ in this work takes the total energy of the crystal to be a sum of atomic pair interactions composed of Coulomb terms and a short-range repulsion of the form

$$U = \sum_{ij} (Z_i Z_j \frac{\text{erfc}(r_{ij}/a_{ij})}{r_{ij}} + A_0 e^{-r_{ij}^2/a_{ij}^2}), \quad (3.1)$$

where  $Z_i = -1, +2$  are the ionic charges,  $r_{ij}$  is the distance between atoms  $i$  and  $j$ ,  $A_0 = 6.75$  H (fitted to best represent the lattice constants of the two bulk materials  $\text{BaF}_2$  and  $\text{CaF}_2$ ) measures strengths of the repulsion between ionic cores, and  $a_{ij}$  is a range parameter defined as the mean ionic radius of atoms  $i$  and  $j$  ( $R_F = 1.170\text{\AA}$ ,  $R_{Ca} = 1.190\text{\AA}$ ,  $R_{Ba} = 1.505\text{\AA}$ ). The presence of the “erfc” term (as opposed to simply “1”) in the numerator should be considered as a part of the short-range repulsion between ionic cores. We include this term because we find it improve the numerical stability of the interatomic potential by removing the Coulomb singularity when ionic cores attempt to overlap.

Table 3.1: Lattice constant  $a$  and bulk modulus  $B_m$  of bulk materials, as computed within our interatomic potential model (described in the text), as computed within density functional theory (LDA PS), and as compared to experiment. All-electron density-functional theory results (LDA AE) and experimental results are from references[17, 2].

	BaF <sub>2</sub>		CaF <sub>2</sub>	
	$a(\text{\AA})$	$B_m(\text{GPa})$	$a(\text{\AA})$	$B_m(\text{GPa})$
Interatomic	6.18	49.4	5.46	82.6
LDA PS	6.08	72.8	5.36	100.4
LDA AE	6.13	74.4	5.35	103.5
Experiment	6.20	56.9	5.46	81.1

Table 3.1 presents the bulk properties of BaF<sub>2</sub> and CaF<sub>2</sub> as computed within this interatomic potential model and within our pseudopotential-LDA *ab initio* framework, and also compares these results to the all-electron results (as a verification of our pseudopotential and choice of energy cutoff) and experimental data[2, 17]. Our *ab initio* results show nice agreement with the all-electron results, and also with the experiment, showing that our *ab initio* calculation correctly reproduces elastic properties of the bulk materials. The interatomic results also agree reasonably well with the experimental data (all quantities within 15%) when kept in perspective of the use to which we put the interatomic potential in this work.

### 3.3 Background

Tera-hertz spectroscopic measurement of Ca doped BaF<sub>2</sub> crystals[110] provides two key quantities related to two-level centers within the crystal, absorption frequency and optical density of states. As Figure 3.1 shows, the absorption frequencies, which corresponds to the splitting between closely spaced energy-levels associated with the double-well energy profile between local minima in



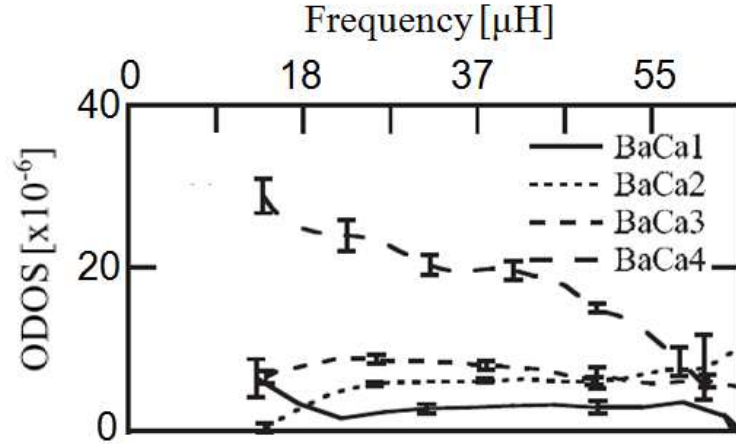


Figure 3.1: Measured optical density of two-level states of the mixed  $(\text{Ba,Ca})\text{F}_2$  crystals versus frequency, adapted from Ref.[110]. Each curve represents a different dopant concentration. For the purpose of presentation in this work, the units of frequency on the horizontal axis have been converted from the  $\text{cm}^{-1}$  of the original reference to  $\mu H$ .

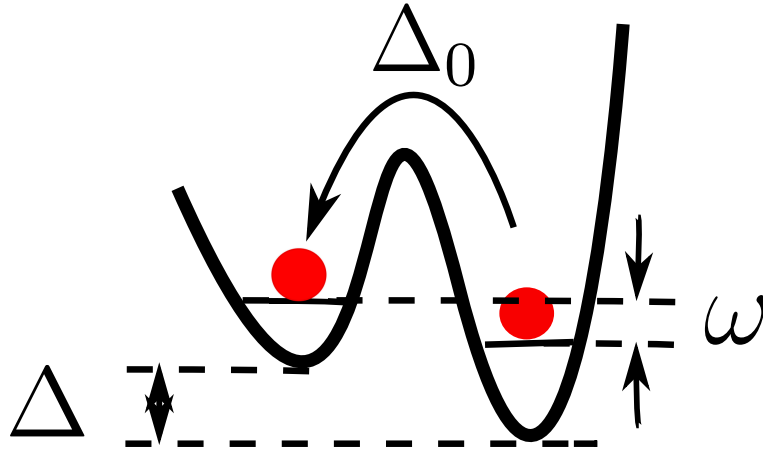


Figure 3.2: Schematic sketch of two-level states.  $\Delta$  is the difference in energy between the minima;  $\Delta_0$  is the magnitude of tunneling probability between the minima;  $\omega$  is the energy splitting between the states.

the crystal ( $\Delta_0$  in Figure 3.2), have been observed in this system to occur from  $10 \mu H$  (and likely down to zero), up to about  $55 \mu H$ . (Here, and throughout, we work in atomic units.) In the standard simplified picture of Figure 3.2, this energy splitting is  $E = \sqrt{\Delta^2 + \Delta_0^2}$ , where  $\Delta$  is the asymmetry in energy between

the minima, and  $\Delta_0$  is the tunneling strength (matrix element) between the two minima. Note that this tunneling strength decreases exponentially with both increasing barrier height and increasing distance between the minima.

The primary quantity determined in the experiments is the optical density of states (ODOS), which yields the total density of two-level centers in the form

$$n_{\text{TLS}} = \int d\omega n_{\text{ODOS}}(\omega)/\mu_b^2(\omega),$$

where  $\omega$  is the absorption frequency, and  $1/\mu_b(\omega)$  is the inverse strength of the electric dipole which couples the center to the external electric field, averaged over all centers with frequency  $\omega$ . In our work below, we determine the dipole strength from the displacement  $r_i$  of each ion  $i$  as the system transitions between neighboring minima through the standard formula  $\mu_b = \sum_i Q_i \Delta r_i$ , where  $Q_i$  is the charge of each ion. To place the magnitude of the observed optical densities in context, we can take a typical characteristic value for  $\mu_b$ . Using the specific two-level center which we found to occur near the middle of the measured absorption spectrum (a di-substitution defect at a local tensile strain  $\epsilon_n - \epsilon_c = 0.4\%$  yielding an energy splitting of  $30 \mu\text{H}$ ) yields the value  $\mu_b \approx 0.9e\text{\AA}$ . This value, combined with the ODOS observed in experimental samples at a dopant concentration of  $8\%$ , yields a density of two-level centers of about  $n_{\text{TLS}} \approx 4 \times 10^{-9}/\text{\AA}^3$ , or  $\approx 2 \times 10^{-7}$  per barium atom.

### 3.4 Initial *ab initio* investigation

Before starting the search for the two-level states, one should keep in mind the difference between an *ab initio* method and a pure theoretical method. Pure theoretical investigations, in general, can either over or under-estimate the density

of TLS's as the proposed mechanisms may or may not be present in the real material. On the other hand, *ab initio* searches identify mechanisms that we believe actually exist, therefore, the total density of TLS's from an *ab initio* identification can only be an *underestimate* by virtue of identifying mechanisms which are present but which may not be the primary contributor. The goal in an *ab initio* search for TLS's, then, is to identify mechanisms with sufficient strength to account for the observed density of two-level centers in the experiment, as we do below.

Following Occam's razor, our search will begin with the simplest possible mechanisms and proceed until we find the one that can account for the observed density. Clearly, given the low occurrence of two-level centers in the material, a brute-force *ab initio* search for such centers among randomly generated dopant configurations would be impractical. Nonetheless, *ab initio* calculations of the doped material provide valuable insights by acting as an effective, high-resolution *in situ* probe of the material behavior in general, and, in particular, the origin of potential energy structures with multiple minima.

We proceed by first constructing  $2 \times 2 \times 2$  cubic supercells of the material with random selection of substitutional defects at a concentration of  $x = 0.25$  (much higher than the experimental concentration, in the hopes of increasing the probability of observing the desired behavior), initially relaxing (with standard steepest descents and conjugate gradient optimization methods) the structures from their ideal  $\text{BaF}_2$  configurations. To detect the presence of multiple minima, we then add random displacements of root-mean-square magnitudes of  $10^{-2}a$ , where  $a = 6.08 \text{ \AA}$  is the cubic lattice constant, and re-relax these structures to the nearest minimum. The result of these studies is that, at this concen-

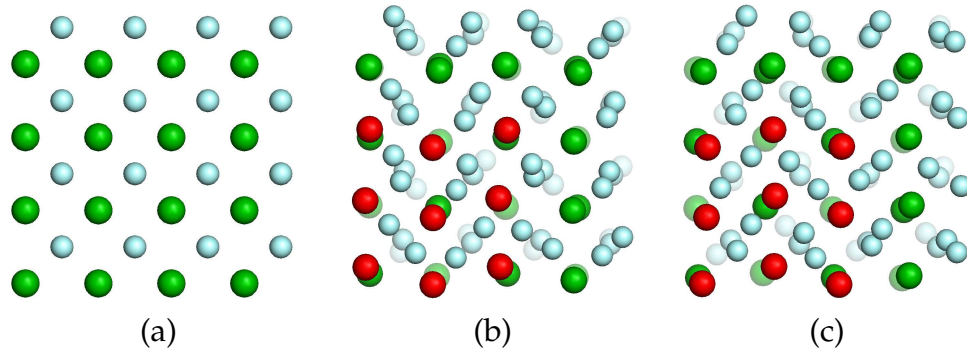


Figure 3.3: *Ab initio* prediction of the atomic locations of local energy minima structures for a ninety-six atom supercell: pure  $\text{BaF}_2$  (a),  $\text{BaF}_2$  with nine Ca substitutions (b and c), barium atoms (green), calcium atoms (red), fluorine atoms (light blue).

tration, multiple minima are quite common, occurring in approximately 10% of our random configurations. We further find that, when multiple minima are found, we can readily identify around 4 distinct minima for each configuration, all similar to those compared in Fig. 3.3. (The substitutional configuration used to generate this figure, consisting of nine defects in a  $3 \times 3$  plane, was chosen for illustrative purposes. Randomly generated configurations show the same features – relatively small distortions of the cation sublattice, and large out-of-line buckling distortions in the lines of anion sites.) This prevalence would correspond to a density of minima of approximately  $n = 2 \times 10^{-3}$  per Ba site (when one accounts for the 32 equivalent Ba sites in our supercell), far larger than would correspond to the observed optical density of states. On the other hand, the energy differences between the minima we have found in this way are typically  $E = 0.1 - 0.4$  eV, three orders of magnitude larger than the energies observed in the optical spectra.

One might hope that, with exhaustive searching, sufficiently small energy differences might be found at a concentration of about  $10^{-8} \text{ \AA}^3$ , and so we next explore the tunneling strength between candidate minima. We calculate

tunneling barriers (transition state energies) between pairs of local minima by performing constrained searches between local minima, defining reaction coordinates along the line segment in phase space connecting the minima and minimizing all coordinates orthogonal to the line segment while holding the reaction coordinate fixed. Unfortunately, we found that the potential barriers were far too high (typically in the range 0.3-0.5 eV) and the separation between minima far too large (typically in the range 3.5-4.8 Å) to lead to sufficient tunneling strengths. From the above observations, we conclude that, while multiple minima are quite common in these structures, only a very special subclass of minima can possibly be responsible for the observed experimental tunneling signatures. To avoid the need for a remarkable coincidence in energy splitting and tunneling strength, the subclass would likely have to have some special symmetry ensuring essentially zero asymmetry in the energies of the minima, an observation also made in a recent theoretical study[74]. Moreover, in our specific case, quite likely, this symmetry would have to be broken by some *fluctuating* external field to result in the observed *distribution* of very small tunneling barriers.

### 3.5 Multiple-minima induced by external strain

Toward identifying the minima responsible for the two-level centers observed in the experiments, we note that the common feature among *all* multiple minima which we identified using the procedure above is that most of the displacement occurs on the anion sites, in the form of what appears to be random buckling, the type of structural instability often associated with strain in a crystal.

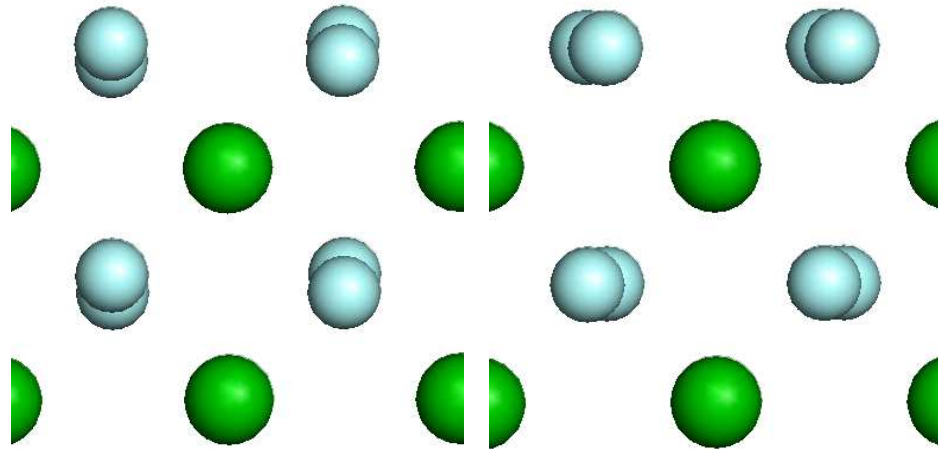


Figure 3.4: Local minima configurations in bulk  $\text{BaF}_2$  under isotropic (tensile) strain of  $\epsilon = 7\%$ : barium (green), fluorine (light blue).

Conjecturing that local strain might provide the needed random fluctuating field, we next induce such minima in pure, bulk  $\text{BaF}_2$  by applying an isotropic external strain. To determine the critical strain, we successively increase the strain, while inducing random distortions in the ionic locations and then re-relaxing the structure to the nearest minimum. We repeat this process until a strain is reached at which the structure no longer relaxes to its high symmetry structure.

Figure 3.4 presents ionic configurations of local minima under tensile isotropic strain near the critical value where we observe the instability to occur,  $\epsilon = 7\%$ . Intriguingly, because the barriers vanish at the critical point, such broken-symmetry configurations indeed can lead to two-level centers with vanishingly small tunneling barriers, for strains sufficiently near the critical point. Moreover, because the multiple minima are induced by spontaneous symmetry breaking, they have very small (zero, in fact) asymmetry in their energies. Indeed, *unlike* systems containing off-centered or rotor defects which inevitably lead to finite tunneling barriers, this critical behavior allows the tunneling bar-

rier to be tuned continuously all the way to zero, thereby opening the possibility of explaining a finite density of TLS's at zero energy. Unfortunately, the critical strain needed to induce these multiple minima (7%) is quite large and extremely unlikely to occur locally in pure regions of the experimental crystals. (Below, we estimate that such strains would occur at less than  $10^{-12}$  per barium site in the crystals employed in the experiments, far less than the observed density of two-level centers.) We conclude, therefore, that the observed two-level centers, if associated with random fluctuations in the local strain field, must directly involve the substitutional defects.

### 3.6 Di-substitutions as two-level centers

Building on the above insights, we consider “seeding” the internal strain distribution by including an explicit substitutional defect to enhance the local strain field, hoping that this then moves the critical strain into an accessible range. Repeating the above procedure with isotropic strains, which do not lower the symmetry of the system and thereby result in zero asymmetry between the resulting minima, we obtain a critical tensile strain for a single substitution of  $\epsilon_c \gtrsim 3\%$ . This strain is again far too large for this defect to be responsible for the observed ODOS because this level of strain would correspond to fewer than  $10^{-8}$  centers per barium site according to our strain distribution studies below.

Encouraged by the large reduction in critical strain by about 4%, we next turn to the “di-substitution” defect, two Ca substitutions separated by a  $\{110\}$  vector on near-neighbor Ba sites. This defect shows a consistent reduction in critical strain from the single substitution, with a remarkably low critical strain,

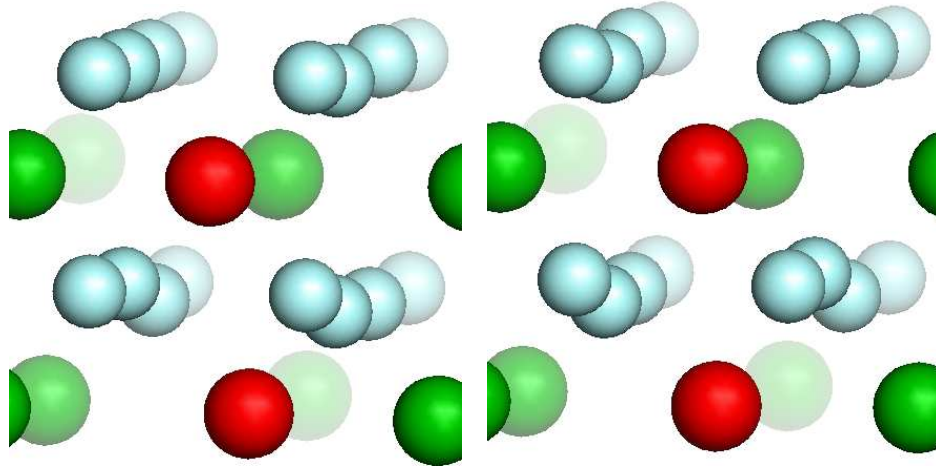


Figure 3.5: Ionic configurations at local minima forming a two-level center: barium (green), calcium (red), fluorine (light blue).

$\epsilon_c \gtrsim 0.2\%$ , well in the range which may well occur as a result of fluctuations in local chemical strain due to substitutional disorder.

As a specific example, Figure 3.5 shows the minimum energy configurations associated with a di-substitution defect under a modest isotropic tensile strain of 0.5%. These minima indeed exhibit the expected rearrangement of anions near dopants in the form of buckling of the lines of anions and are clearly related by a mirror symmetry about the (100) plane containing the substitutions, so that the asymmetry in their minimum energies is zero. Moreover, at this strain, the tunneling barrier between the local minima is on the order of 0.1 mH, sufficiently low to lead to two-level centers in the range observed in the experiments. (According to the excitation energy results from Figure 3.8 below, this particular configuration would have a two-level splitting of  $50 \mu\text{H}$ , within the upper end of the range measured in the experiments.)

To quantify the two-level splittings resulting from such defects and the likelihood of the local strain being in the correct ranges to lead to such splittings



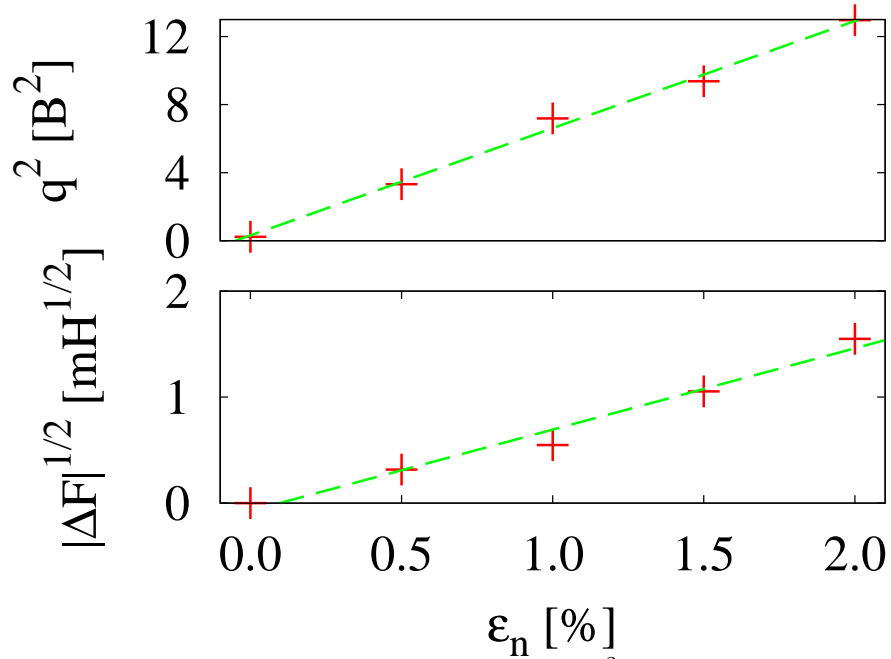


Figure 3.6: Square of transition order parameter,  $q^2$ , versus strain  $\epsilon$  (upper panel); square-root of transition energy,  $\sqrt{\Delta F}$ , versus strain  $\epsilon$  (lower panel): *ab initio* results (crosses), linear fits (dashed lines).

at densities corresponding to the observed optical DOS, we next consider the coupling of strain to the energy profile connecting the two minima. Figure 3.6 shows *ab initio* results for the magnitude  $q$  of the displacement vector connecting the two minima in phase space and for the tunneling barrier height  $\Delta F$ , the combination of which determine the tunneling strength and thus the two-level splitting, as a function of isotropic tensile strain. The data in the figure confirm the existence of a critical tensile strain of approximately  $\epsilon_c = 0.0 - 0.2\%$ . The key here is that the associated barrier height and atomic displacements vanish near  $\epsilon_c$ , so that the quite small splittings in the experimentally observed range can always be obtained for strains sufficiently close to  $\epsilon_c$ . The key question then becomes whether the local strain fluctuations would generate strains in this range for sufficient numbers of di-substitution defects to explain the experimentally observed density.

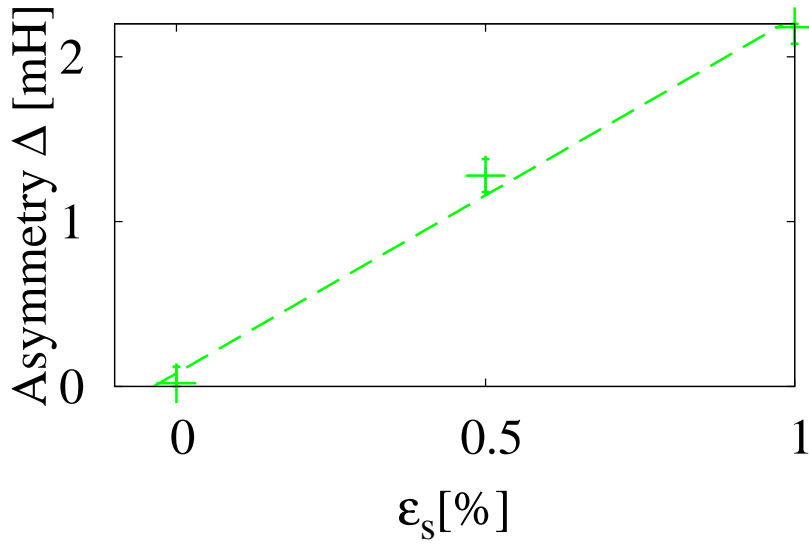


Figure 3.7: Energy asymmetry between local minima of di-substitution defect under an otherwise isotropic tensile strain of 1.0%.

To answer this question, we first note that the linearity in the plotted quantities (square of the displacement of the minima from the high symmetry state and square-root of the barrier height) implies a second-order, strain-driven phase transition and indicates that a simple Landau Hamiltonian suffices to capture the energetics of the defect for isotropic tensile strains up to a few percent.

Whereas isotropic tensile strains lead to zero asymmetry in the minima, the actual local strains resulting from the substitutional disorder are also unlikely to be purely isotropic. As Figure 3.7 shows, such shear strains break the reflection symmetry of the defect, leading to a linear dependence in the asymmetry as a function of shear strain. The data in the figure indicate that the asymmetry grows rapidly with shear strain, so that candidate two-level centers can only occur in regions of the crystal with small local shear strains, an effect we must consider carefully in determining the density of two-level centers. Finally, again, the linear dependence indicates that a low-order Landau Hamiltonian

suffices to model these effects for local strains up to a few percent.

### 3.7 Landau analysis

Exploration of the full range of strains induced by substitutional disorder requires an analytic free energy model as a function of the local strain. Consistent with the *ab initio* data presented above, we now present a low-order Landau Hamiltonian whose structure is constrained by symmetry and whose coupling coefficients we determine from our *ab initio* data. Expanding in powers of order parameter  $q$ , the lowest-order Hamiltonian consistent with the second-order phase transition observed above must include orders up to and including  $n = 4$ . Clearly, the zeroth order term is irrelevant to the present discussion and the system should be invariant under mirror reflection about a plane containing the defects so that the Hamiltonian must respect the symmetry  $(\epsilon_s, q) \leftrightarrow (-\epsilon_s, -q)$ , where  $\epsilon_s$  is the shear strain. From this, it follows that, in the absence of shear strain, the Hamiltonian must include the displacement  $q$  only in even orders,  $(\epsilon_s = 0, q) \leftrightarrow (\epsilon_s = 0, -q)$ . This leaves as the lowest-order Hamiltonian sufficient to capture our results,

$$F(q) = \frac{1}{4}Aq^4 + \frac{1}{2}\gamma(\epsilon_c - \epsilon_N)q^2 + \beta(\epsilon_S)q, \quad (3.2)$$

where the subscripts  $S$  and  $N$  refer the shear and normal strain components respectively, and  $\gamma(\epsilon_N)$  and  $\beta(\epsilon_S)$  are functions which behave linearly under small isotropic strains.

Under isotropic strain with zero shear components, Equation 3.2 reduces to

Table 3.2: Landau expansion coefficients for strain measured in fractions (not percent) and free energy measured in hartree.

$A$ (H/B <sup>4</sup> )	$\gamma_N$ (H/B <sup>2</sup> )	$\beta_S$ (H/B)	$\epsilon_c$ (%)
$4.7 \times 10^{-4}$	0.075	0.079	0.2

the Landau Hamiltonian

$$F(q) = \frac{1}{4}Aq^4 + \frac{1}{2}(\epsilon_c - \epsilon_N)\gamma_Nq^2,$$

where  $\gamma_N$  is the coefficient of the leading term of the function  $\gamma(\epsilon)$ . This reduced Hamiltonian predicts a structural phase transition for  $\epsilon > \epsilon_c$ , with magnitude of displacements  $q_0^2(\epsilon) = \gamma_N(\epsilon - \epsilon_c)/A$  and a potential barrier  $\sqrt{\Delta F(\epsilon)} = \gamma_N(\epsilon - \epsilon_c)/\sqrt{2A}$ . The linearities of  $q^2$  and  $\sqrt{\Delta F}$  with strain agree well with our *ab initio* results shown in Figure 3.6 as mentioned above, and allow us to obtain  $A$ ,  $\gamma_N$  and  $\epsilon_c$ , which appear in Table 3.2.

Under the combination of nonzero shear and isotropic tensile strain, Equation 3.2 includes terms of linear order in the shear and results in the following for the asymmetry (details in the Appendix),

$$\Delta(\epsilon_N, \epsilon_S) = 2\beta_S\epsilon_Sq_0(\epsilon_N), \quad (3.3)$$

where  $q_0(\epsilon_N) = \sqrt{\gamma_N(\epsilon_N - \epsilon_c)/A}$ , and  $\beta_S$  is the coefficient of the leading order in the function  $\beta(\epsilon_S)$ . The linear dependence of the resulting asymmetry  $\Delta$  on  $\epsilon_S$  agrees well with our *ab initio* results shown in Figure 3.7 and allows us to obtain the parameter  $\beta_S$ , which also appears in Table 3.2.

Finally, for the case of anisotropic strain, which also breaks the symmetry of the minima, the detailed analytic forms for  $\gamma(\epsilon_N)$  and  $\beta(\epsilon_S)$  depend on the interplay of symmetry between the defect and the strain and should not depend on the nature of the underlying atomic interactions. Accordingly, in the Appendix

we explore the analytic structure (not the values of the coupling coefficients) of these functional forms within the interatomic potential model described in Section 3.2 above. As described in the appendix, for the fully anisotropic case, we find that the coupling term  $\gamma$  generalizes to a Pythagorean mean displacement from the critical value whereas the coupling term  $\beta$  generalizes to a (linear) arithmetic sum,

$$\gamma(\epsilon_N) = \gamma_N \sqrt{\sum_N (\epsilon_N - \epsilon_c)^2 / n_N} \quad (3.4)$$

$$\beta(\epsilon_S) = \beta_S \sum_S \epsilon_S. \quad (3.5)$$

Accordingly, our further analyses employ these basic functional forms for the Landau Hamiltonian, while employing the parameters  $\gamma_N$ ,  $\epsilon_c$ , and  $\beta_S$  as determined from our *ab initio* calculations and displayed in Table 3.2.

### 3.8 Spectral properties of the di-substitution

With the model Hamiltonian fully constructed and its parameters determined *ab initio*, we now predict the spectral quantities that can be expected to result from the interaction of the di-substitution defect with the local strain fields resulting from substitutional disorder.

In order to determine the energy-level splittings of the two-level states, which correspond to the absorption frequencies in the experiments, we solve a one-dimensional Schrödinger equation in the coordinate  $q$  for a particle with the effective mass of 25.466 u moving subject to the potential energy given in Equation 3.2. (The effective mass is computed as the weighted average mass where the weights are the square of displacements along the reaction coordi-

nate,  $m_{eff} = \sum_i M_i \Delta x_i^2 / \sum_i \Delta x_i^2$ . Using our local minima configurations under a typical strain of 0.5%, we find  $m_{eff} = 25.466$  u, which is much closer to the fluorine atomic mass 18.998 u than the barium atomic mass 137.327 u.) Figure 3.8 shows the resulting energy-level splittings (between the ground and first excited state) as a function of (Pythagorean mean) distance from critical normal strain, for a variety of (sum of) shear strains, and compares these with the range of frequencies measured in the experiments, 10 to 55  $\mu H$  (66-360 GHz). Coincidence between the predicted two-level splittings and the range explored in the experimental measurement occurs for sum of shear strains with absolute value less than 0.03% and, simultaneously, tensile strain within a range of 0.3 to 0.5% of the critical strain. (The critical strain for tensile strain is  $\epsilon_c \approx 0.2\%$ .) The next section considers the concentration at which we should expect di-substitutions to occur with local strains in these ranges in order to determine whether they actually can be responsible for the absorption observed in the experiments.

### 3.9 Statistical Analysis of Strain Distribution

Above we find that only a narrow range of strains induce level-splittings in the experimentally observed range. At the experimentally observed two-level center concentration of  $\sim 10^{-7}$  per barium site, it would be impractical to search for such occurrences in *ab initio* calculations of random distributions of defects. Because at this stage we only require a basic estimate of the likelihood of strains occurring in the correct range, we instead employ a combination of statistical analysis with continuum and interatomic potential modeling. The fact that the latter two approaches give reasonable descriptions of, at least, long-range strain fields, justifies their use to give an approximate description of the distribution

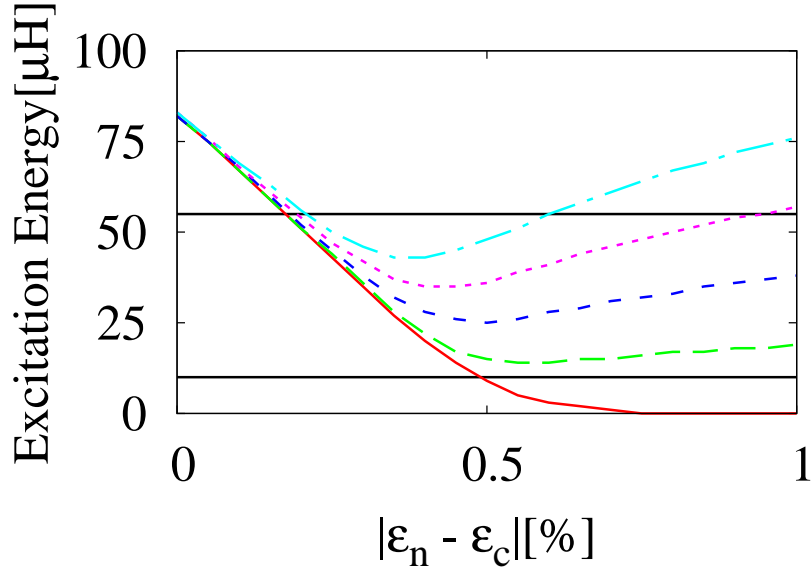


Figure 3.8: Two-level state excitation energies of di-substitutions as a function of tensile strain: shear strains of 0%, 0.01%, 0.02%, 0.03% and 0.04%(lower to upper curves, respectively), lower and upper ranges of excitation spectrum observed in the spectroscopic measurement [110] (horizontal lines).

of local strain fluctuations.

In order to simplify our analysis to determine a first estimate of the concentration of two-level centers with excitation energies in the experimentally observed range, we assume that the formation of a di-substitution is independent of the local strain, so that the density of two-level states is

$$n_{\text{TLS}} = P_{\text{strain}} \times P_{\text{di}}, \quad (3.6)$$

where  $P_{\text{di}}$  is the probability of di-substitution formation at a particular barium site, and  $P_{\text{strain}}$  is the probability of strain fluctuation in the suitable range to account for the observed two-level centers.

To determine the occurrence probability  $P_{\text{di}}$  of the di-substitution itself, we first note that if the placement of substitutions at defect concentration  $c$  were

completely independent, this probability would be  $P_{\text{di}} = Nc^2(1 - c)^{m-1}/2$ , where  $N$  and  $m$  are number of nearest neighbor cation sites to, respectively, either (a) a single cation site or (b) an already-formed di-substitution defect ( $N = 12, m = 18$  in this case), with the factor of two correcting for over-counting the same di-substitution as belonging to two separate cation sites. The substitutions, however, have an attractive interaction, as Figure 3.9 shows. This interaction is negligible compared to thermal energy scales ( $1 \text{ mH} \approx k_B T$ ) at room temperature) except when the substitutions occur on neighboring sites, where there is an attractive interaction of about  $\Delta E = 2 \text{ mH}$ . Accounting for this by a nearest neighbor enhancement factor  $\alpha = e^{\Delta E/k_B T}$ , where  $T$  denotes the effective temperature scale at which the substitutional configuration becomes frozen-in, the probability of formation of a di-substitution (as opposed to single substitutions or higher order clusters) becomes

$$P_{\text{di}} = Nc^2\alpha(1 - c\alpha)^m/2 \text{ per site.} \quad (3.7)$$

Taking the substitutional freeze-in temperature to be about 1700 K, taken from the annealing temperature in the spectroscopy measurement[110], gives  $\alpha \approx e^{0.38}$  and then, for the critical dopant concentration  $c = 0.08$  observed in the experiments, we find  $P_{\text{di}} \simeq 0.0060$ .

Next, to determine the distribution of local chemical strains, we first determine the strain field from an isolated substitution, using the interatomic potential to give what should be a reliable estimate of this essentially continuum elastic property. Then, at the concentration of  $c = 0.08$  from the experiments, we construct over  $10^7$  random substitutional configurations in large supercells of size  $5 \times 5 \times 5$  and employ the principle of super-position from continuum elasticity theory to estimate the resulting local strain at a given site. Finally, we gather statistics of the local strain for  $10^7$  sample configurations.



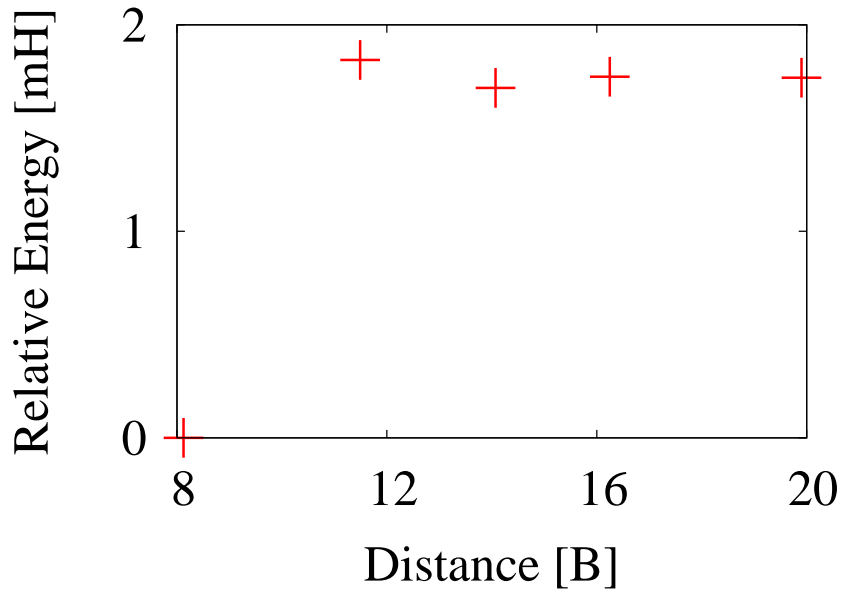


Figure 3.9: Interaction energy of substitutions as a function of distance with the closest arrangement as reference to the energy. Data show that there is relatively little interaction until substitutions site on neighboring sites (distance  $\approx 8$  bohr).

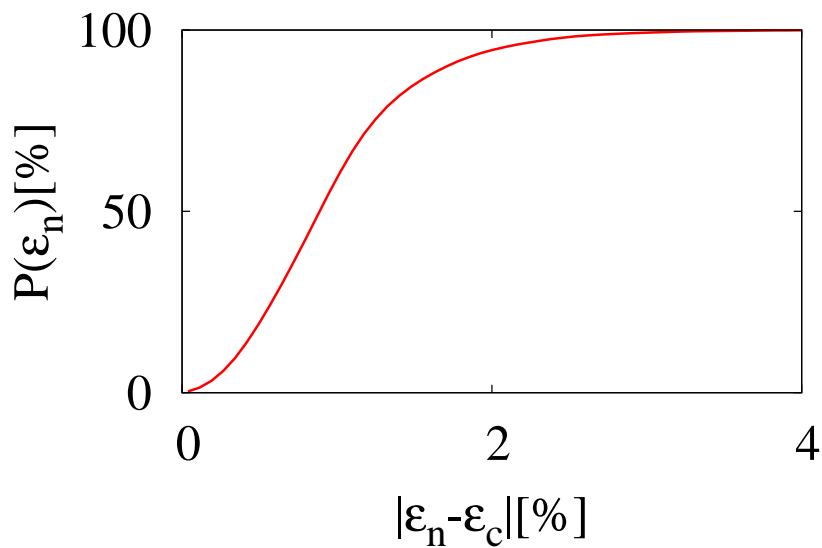


Figure 3.10: Cumulative probability distribution of Pythagorean mean of normal components of strain. Statistical sampling with the interatomic potential model for 1500 atom cell with random dopants of average concentration 0.08.

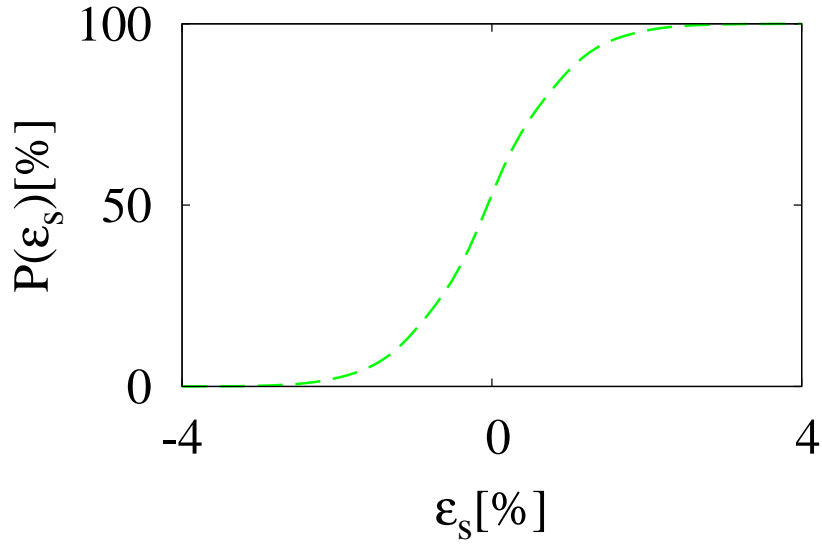


Figure 3.11: Cumulative probability distribution of sum of shear components of strain. Statistical sampling with the interatomic potential model for 1500 atom cell with random dopants of average concentration 0.08.

From this statistical sample, we find the fraction of sites with the appropriate range of shear and normal strain simultaneously,  $|\sum_{i \neq j} \epsilon_{ij}| < 0.04\%$ ,  $(0.3\%)^2 < (1/2) \sum_i (\epsilon_i - \epsilon_c)^2 < (0.5\%)^2$  according to Eqs. (3.4 and 3.5), to be  $P_{\text{strain}} = 0.0053$  with both places statistically significant. To better understand the origin of this result, Figures 3.10 and 3.11 show the cumulative probability distributions of root-mean-squares of normal components and sums of the tensile components of the local strain, respectively. If the normal and shear components of strain were completely uncorrelated, then the probability of finding the suitable range of strain is determined as the product of the independent probabilities for each component. These independent probabilities, in turn, equal the product of the slope of each distribution curve with the width of the range of concern, yielding 0.084 and 0.042, respectively. This independent probability analysis would then give an estimate of 0.0035, in reasonable agreement with our value from direct

correlated sampling.

Now, using our value  $P_{\text{strain}} = 0.0053$  for the likelihood of having strain in the correct ranges, and our probability  $P_{\text{di}} \simeq 0.0060$ , we predict a density of two-level centers of  $n_{\text{TLS}} = 3.2 \times 10^{-5}/\text{site}$  which is within two orders of magnitude of the absorption strength from the spectroscopic measurement  $2 \times 10^{-7}/\text{site}$ , reasonable agreement given the approximate nature of our counting analysis for the prevalence of isolated di-substitution defects. (The results are fairly sensitive to the freeze-in temperature, choosing 700 K instead of the annealing temperature brings the results to within an order of magnitude.)

Very importantly, the fact that we are finding an *overestimate* implies that di-substitutions with the appropriate splittings occur in more than sufficient numbers to account for the optical DOS and that the di-substitutions must be considered strong candidates for a significant portion of the observed absorption. The fact that our result is somewhat too high suggests that perhaps additional effects (strain fields from dislocations or other defects) quench out some of the di-vacancy centers.

Finally, to compare in more detail with the spectroscopic measurement, we split the measured spectrum range into several frequency intervals and evaluate the density of two-level centers for each interval, which is equivalent to taking numerical derivatives of the density of states at a given energy. Under the assumption of an approximately constant dipole strength  $\mu_b$ , this derivative is, up to a constant factor, precisely the optical density of states, which is the experimentally observed quantity. Figure 3.12 presents the resulting computed density of TLS for five  $10\mu\text{H}$  wide intervals, covering from 0 to  $50\mu\text{H}$  ( $4.56\mu\text{H} = 1 \text{ cm}^{-1}$ ). The general features we observe are precisely those found

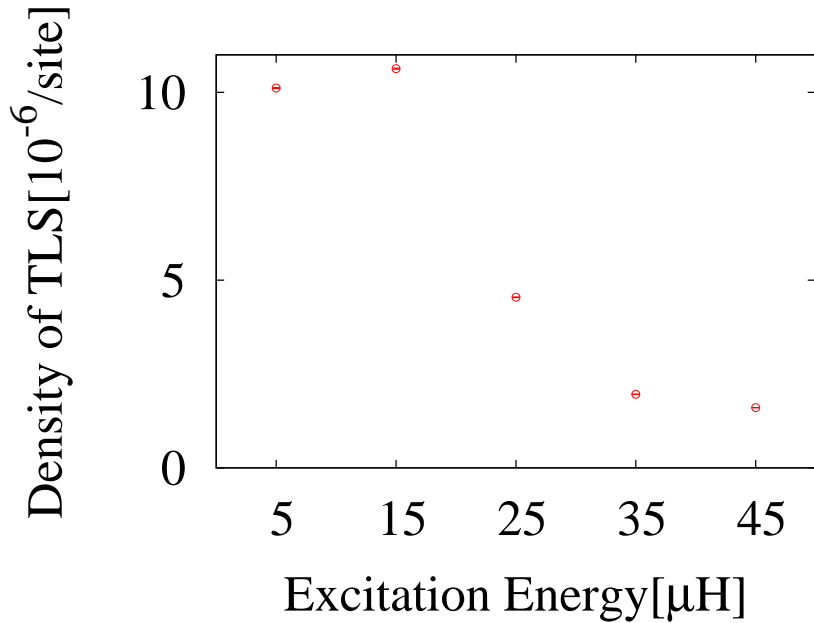


Figure 3.12: Calculated TLS density within various frequency intervals. Intervals are  $10 \mu\text{H}$  wide, with data points located at the center of each interval. Error bars correspond to  $\pm 1 \sigma$  ranges based on Poisson statistics.

in the experiments at 8% nominal concentration (compare to long dashed curve in Figure 3.1, which is adapted from J. P. Wrubel *et al.*[110]): a fairly constant concentration at low frequencies, with steeper drop off toward zero concentration at higher frequencies. We also find rough agreement (which is impressive given the approximate nature of our statistical analysis and present assumption of constant  $\mu_b$ ) for the frequency range corresponding to the drop off. We find the drop off to begin between 15–25  $\mu\text{H}$  ( $=3.3\text{--}5.5 \text{ cm}^{-1}$ ), whereas the steeper drop off in the experiments occurs between 9–11  $\text{cm}^{-1}$ . These results are quite promising as no theory as yet has made a prediction for the existence or location of this drop off. More careful investigation of this issue clearly is warranted.

### 3.10 Conclusion

We present a quantitative *ab initio* study of two-level states in a class of glass-like substitutional mixed crystals. The two-level states appear to arise from a structural instability followed by rearrangements of fluorine atoms, driven by fluctuating local chemical strains due to random displacements of the substitutions. Our data indicate that the structural instability is well described as a second-order phase transition governed by the tensile component of strain, with the shear component adding an asymmetry to the potential energy surface. A Landau free-energy Hamiltonian captures well the interaction of strain with the reaction coordinate connecting the minima associated with the two-level centers. With parameters determined from *ab initio* calculations, this microscopic Hamiltonian successfully predicts the two key observables of the two-level centers, the excitation spectrum and the optical density of states, both yielding results in good agreement with THz spectroscopy data, *including* a finite density of TLS's in the zero-frequency limit. This success suggests not only that fluctuating local crystal strains should be considered as one of the many mechanisms explaining TLS behavior, but also that the combination of *ab initio* calculation with similar analyses opens a promising route study of glassy systems in the future.

Future work should include several more detailed analyses to improve the quantitative predictions of this work. For example, more detailed study of the fluctuations in the local strain fields should include *ab initio* results for the near-field strain fields from substitutions, as linear elastic theory does not give a particularly accurate description of these. To avoid prohibitively expensive calculations, such results could be combined with linear elasticity theory for the long-

range strain fields. Second, a more careful analysis of the statistical corrections due to correlations and possible clustering among the substitutions are also warranted. Third, more detailed analyses incorporating the strain-dependence of the coupling dipole  $\mu_b$  may also improve the quantitative agreement with the experimental observations. Finally, while we have demonstrated that the di-substitution defect is sufficient to account for most, if not all, of the observed experimental signal, further investigations of larger clusters (tri- or quad- substitutions) are also warranted, as these may help to extend our range of frequencies before our predicted drop off at 3.3–5.5  $\text{cm}^{-1}$  into better agreement with the experimental observation of this drop off between 9–11  $\text{cm}^{-1}$  if the above improvements do not lead to better overall agreement.

The authors are grateful to J. P. Sethna and A. J. Sievers for many fruitful discussions.

## CHAPTER 4

### EFFICIENT TREATMENTS FOR SOLVENT ENVIRONMENTS IN EXCITED STATE CALCULATIONS: GW FOR SOLVATED SYSTEMS

Molecular excitations in dielectric environments have drawn a great deal of interest because manipulation of the molecular environment provides the possibility to engineer photo-excitation processes. Although the polarizable continuum medium (PCM) model, in combination with time-dependent DFT (TDDFT), has been successful in obtaining solvent shifts in exciton energies (*solvatochromic* shifts) for solvated molecules, the standard TDDFT approach is known to be very poor in predicting excitation energies for extended systems such as surfaces.

As an alternative to the TDDFT approach, here we explore the development of efficient solvent treatments for use within the framework of many-body perturbation theory (MBPT) approaches, methods known to give much accurate predictions of excitation energies than TDDFT, and which are capable of addressing quasiparticle energies — something which TDDFT does not predict. These methods include the GW method for quasiparticle energies and the Bethe-Salpeter equation (BSE) for optical excitations.

This chapter deals with the formal development of two approaches to the solvent treatment: (1) joint density-functional theory (JDFT) employing a continuum model of the dielectric response of solvent, and (2) the quantum-chemistry inspired molecular embedding method, which is closely related to the cluster expansion approach. Our discussion begins with detailed considerations of the modifications which must be made to the GW method to incorporate such descriptions of the solvent, and then goes on to explore the convergence of

the cluster expansion method when applied to molecular embedding. The next chapter will show the results of applying these methods to solvated molecules.

## 4.1 Introduction

Incorporation of the environmental effects in excited state calculations are essential for many systems. Numerous biological and electrochemical systems naturally exist dissolved in aqueous solutions. Empirically, it is observed that the excitation spectrum shifts in response to the presence of the environment, thereby opening a pathway to tune excited state properties to specific applications (such as capturing larger portions of the ground-level solar spectrum in solar cells). An example of a successful application is the dye sensitized solar cell immersed in liquid solvent, known as the Grätzel cell[75, 36]. Shift in the excitation spectrum from the gaseous state (i.e., isolated molecules or vacuum) to the crystalline state occurs for most organic molecules such as naphthalene and benzene, common testing systems in many quantum-chemistry calculations.

There have been many attempts to incorporate environmental responses into excited state calculations[21, 72, 29, 42, 39, 33], and these approaches can be grouped into the two main categories: including explicitly the molecular environment[42, 39, 33], and employing a continuum model describing polarization effects[21, 72, 29]. The first approach is commonly applied when atomic coordinates of the entire system are either frozen or easily computable, or with the aid of molecular dynamics for phase-space sampling of structural rearrangements (the QM/MM method). When employing the GW and Bethe-Salpeter equation to compute exciton energies, this is straightforward but quite computationally intensive. Indeed, this approach has been successful in obtaining the exciton



energy shift of H<sub>2</sub>O molecules, in going from the gaseous to crystalline phase, and even in going from the gaseous to liquid phase by use of the QM/MM method[42]. However, the computational cost of this approach depends heavily on the simplicity of the molecular structure: specifically, for general solute-solvent systems involving global rearrangement of molecules, the phase space sampling significantly raises computational costs, requiring repetition of a large number of calculations which are already quite expensive.

The continuum description, on the other hand, employs a continuous dielectric function in Poisson's equation to represent the electrostatic response of solvent. This class of approaches, generically known as the polarizable continuum medium (PCM) methods, clearly requires less computational power as only a single excited-state calculation is required. PCM is often incorporated into time-dependent density functional theory (TDDFT) calculations, which compute the exciton frequency by solving the Dyson's equation for collective charge fluctuations. This approach has been successful in calculating solvatochromic shifts for various small molecules solvated in aqueous solutions[21, 72]. However, TDDFT calculations are well known to produce wrong predictions for extended systems as a result of the *local* or *semi-local* density functional approximations typically made to the exchange-correlation kernel in the theory[15]. Moreover, the dielectric function in the PCM method fails to incorporate details of the local microscopic structure, which is essential in describing short-wavelength features of the solvent effect.

As a way to evaluate the reliability of the resulting method for calculating quasiparticle states and, ultimately, to find ways to improve upon it, we also here consider a more direct approach, which is to include the RPA response

function of the solvent system directly into the excited state calculations. To analyze the RPA response of the solvent, we follow an approach inspired by the cluster-expansion methods of quantum-chemistry. In this context, the cluster expansion gives a series expansion of the solvent response whose leading order term is the sum of the responses of individual solvent molecules. With the higher-order terms omitted, the evaluation of the series requires clusters of up to only a few molecules to be considered, which is computationally much less demanding than explicitly computing the response for the entire solvent. It turns out that, in the case of small clusters of H<sub>2</sub>O molecules, including just the first two terms or even just the first term in the response series is sufficient to give quasiparticle energies quite close to those calculated with the full, explicit response function.

## 4.2 Continuum environment approaches

The underlying picture of the environment in the polarizable continuum method is straightforward. In this picture, the distinction between solute and solvent systems is clear, and the solvent is represented as a smooth continuum of charges. The interaction between solute and solvent is characterized by continuum dielectric screening of the Coulomb interaction taking into account the rearrangements of nuclei and (mostly, for the frequencies relevant to electronic excitations) electrons of the environment in response to the potential fluctuations arising from motion of charges in the solute. To mimic the physical boundary between solute and solvent, the continuum media is assumed to have cavities around solute molecules in which the dielectric screening is zero, *i.e.*  $\epsilon(r, \omega) = 1$ , with the the rest of space treated with the bulk solvent response  $\epsilon(r, \omega) = \epsilon_b(\omega)$ ,

where  $\epsilon_b(\omega)$  is the macroscopic dielectric constant of the bulk solvent at the relevant frequencies.

This simple description has been quite successful in reproducing solvation effects on various material properties, including zero-frequency equilibrium properties such as free energies[22, 103], as well as and exciton energy shifts[21, 29, 72]. However, the shape and size of the dielectric cavities employed have to be predetermined, and often have to be fitted to get reliable results.

#### 4.2.1 Overview of joint density-functional theory (JDFT)

As an alternative to the aforementioned fitting and the general *ad hoc* nature of these approaches, Petrosyan and coworkers[82] introduced the joint-density functional theory. This theory, which stems from a set of theorems which require no approximations *in principle*, combines the *ab initio* description of the solute electrons with the continuum solvent model by defining the new free energy functional,

$$A[n(r)] = A_0[n(r)] + \int d^3r \left( \phi(r)(n(r) + N_{ion}(r)) - \frac{\epsilon[n(r)]}{8\pi} |\nabla\phi(r)|^2 \right), \quad (4.1)$$

where  $n(r)$  and  $N_{ion}(r)$  are electron and nuclei charge densities,  $A_0$  is the single-particle kinetic plus exchange-correlation components of the original Kohn-Sham free energy, and  $\phi(r)$  is the mean electrostatic potential field. The ground state is obtained by minimizing the above free-energy functional with respect to both the electron density and the potential field, which at the same time should satisfy the Poisson equation below:

$$\nabla \cdot (\epsilon(r)\nabla\phi(r)) = -4\pi (n(r) + N_{ion}(r)). \quad (4.2)$$

For practical calculations, Petrosyan and coworkers[82] approximated the dielectric constant functional  $\epsilon[n(r)]$  as a local function of the electron density  $n(r)$  with the expression

$$\epsilon(r) = 1 + \frac{\epsilon_b - 1}{2} \operatorname{erfc} \left( \frac{\ln(n(r)/n_c)}{\sqrt{2}\sigma} \right), \quad (4.3)$$

where  $n_c$  is the critical value of electron density determining the boundary between vacuum and solvent, and  $\sigma$  controls the width of the transition from bulk to vacuum. Writing the dielectric parameter field as a function of the *ab initio* electron density allows the solvent media to be consistent with the electronic structure of the system. Moreover, the continuous boundary between solvent and cavity provides more reliable solvent descriptions than the original PCM methods with discontinuous cavity boundaries. Finally, it is observed that results are relatively insensitive to the transition width  $\sigma$ , so that, in practice, there is only one fit parameter  $n_c$ , as opposed to a much larger set of fit parameters in the standard PCM, which requires van der Waals radii for each functional group of a molecule[16, 103].

So far, we have discussed procedures for equilibrium calculations, where systems are assumed to be in a static equilibrium. For non-static, dynamic situations, such as the study of excitons in TDDFT or virtual excitations in the GW quasiparticle calculations, this approach must be modified. In this work, we employ the time-dependent extension of joint density-functional theory proposed by Lischner *et al.* [60], where the dynamic response of the solvent is characterized by a frequency-dependent dielectric functional  $\epsilon[n(r), \omega]$ . In this approach, the solute electron density and nuclei are assumed to be frozen such that cavities remain constant during excitations. The bulk dielectric parameter  $\epsilon_b$  in Eq. (4.3) then becomes the only frequency-dependent term. The frequency-dependent bulk dielectric constant is then estimated from the low-lying excitations of the

solvent molecules as[60]

$$\begin{aligned}\epsilon_b(\omega) &= 1 + \frac{N_{sol}\gamma(\omega)}{1 - N_{sol}\gamma(\omega)/3} \\ \gamma(\omega) &= \sum_i f_i/(\omega_i^2 - \omega^2),\end{aligned}\tag{4.4}$$

where the first expression is the Clausius-Mossotti relation between the macroscopic dielectric parameter  $\epsilon_b(\omega)$  and molecular polarizability  $\gamma(\omega)$ , with  $N_{sol}$  being the density of solvent molecules. The next line defines the frequency-dependent polarizability from the molecular excitations  $i$ , each with oscillator strength  $f_i$  and excitation frequency  $\omega_i$ .

For the equilibrium calculations below of molecules solvated in liquid water, we use the known macroscopic dielectric parameter of water  $\epsilon_b = 80$ , with  $n_c = 7 \times 10^{-4}$  and  $\sigma = 0.6$  as given in the previous work by Petrosyan *et al.*[82]. For the embedded GW calculations, we used low-lying excitation modes of the H<sub>2</sub>O molecule calculated by Lischner *et al.*[60], which gives us  $\epsilon_b$  ranging from 1.6 to 1.8 for frequencies, or equivalently excitation energies, ranging from 0 to 2 eV, agreeing well with the experimental data. Finally, to perform the requisite frequency integrals of the GW method, we employ the contour deformation technique[57, 35], with an analytic continuation of Equation 4.4 to evaluate the bulk dielectric parameter and electronic response functions at complex frequency.

### 4.3 Molecular embedding methods

As an alternative to the above continuum model for solvents, one may include the solvent molecules explicitly at a reduced level of theory to make the calculations tractable. For ground-state calculations, one recent approach is the

orbital-free embedding technique[109]. Assuming that the electron density of the solvent is already known and that there is no need for it to be updated (as in the case of closed shell molecules with relatively low electronic polarizabilities), the solvent system can be treated as a frozen environment providing a fixed background electron density, and full density-functional theory calculations are only needed for the solute system. Following the same logic as the pseudopotential approach in solid-state physics, where the core electrons are regarded as fixed and static, the solvent effect is then represented and included as an external potential in the DFT calculation for the solute.

As in the continuum model, this approach assumes a sharp distinction between the solute and solvent. The total electronic density is then expressed as  $n_{tot} = n_{sys} + n_{env}$ , where  $n_{sys}$  is the electron density of the solute system, determined from its Kohn-Sham orbitals, and  $n_{env}$  is the (static) density of the solvent environment. According to the Hohenberg-Kohn-Sham theorems, there exists an energy functional whose variational derivative with respect to the electron density gives the effective potential in the Kohn-Sham equation. Applying similar logic, the solute-solvent coupling can be characterized by an effective potential in the Kohn-Sham equation, obtained by taking a variational derivative of the non-additive part of the energy functional for the entire system. The resulting effective potential, denoted as the coupling potential  $V_{cpl}$  in this thesis, is thus

$$V_{cpl} = \frac{\delta}{\delta n_{sys}} (E[n_{tot}] - E[n_{sys}] - E[n_{env}]). \quad (4.5)$$

With this coupling potential, the Kohn-Sham equations for the solute electrons

become

$$\left[ -\frac{1}{2}\nabla^2 + V_{eff}[n_{sys}] + V_{coupling}[n_{tot}, n_{sys}] \right] \psi_i(r) = \epsilon_i \psi_i(r)$$

$$\sum_i |\psi_i(r)|^2 = n_{sys}(r), \quad (4.6)$$

where  $V_{eff}$  is the single-particle potential for the solute system only, and  $\psi_i(r)$ ,  $\epsilon_i$  are the Kohn-Sham orbitals and eigenvalues for  $i$ -th Kohn-Sham state.

Within standard density-functional theory, the energy functional  $E[n]$  is

$$E[n] = \int dr (n(r)V_{ion}(r) + f_{xc}[n(r)] + f_{TF}[n(r)]) + \frac{1}{2} \int dr dr' \frac{n(r)n(r')}{|r-r'|}, \quad (4.7)$$

where  $V_{ion}$  is the ionic potential coming from the nuclei and core electrons in the form of a pseudopotential,  $f_{xc}$  is the exchange-correlation functional, which is often approximated as a local function of electron density within the local density approximation (LDA). For the kinetic energy part, for which an exact functional form does not exist, an approximate functional,  $f_{TF}$  is used instead, the simplest available functional form from the Thomas-Fermi (TF) theory,

$$f_{TF}[n(r)] = \frac{3}{10}(3\pi^2)^{2/3}n^{5/3}(r). \quad (4.8)$$

With the given energy functional above, the coupling potential becomes

$$V_{cpl}(r) = V_{ion}^{env}(r) + \int dr' \frac{n_{env}(r')}{|r-r'|}$$

$$+ \left( \frac{\partial f_{xc}}{\partial n} + \frac{\partial f_{TF}}{\partial n} \right) [n_{tot}(r)] - \left( \frac{\partial f_{xc}}{\partial n} + \frac{\partial f_{TF}}{\partial n} \right) [n_{sys}(r)], \quad (4.9)$$

where  $V_{ion}^{env}$  is the ionic potential from the environment. Consequently, the coupling potential is dependent upon the solute electron density and thus must be consistent with the Kohn-Sham equation above. In order to satisfy the self-consistency between Equations 4.6 and 4.9, we iteratively solve these equations for  $n_{sys}$  while keeping  $n_{env}$  frozen until the subsystem energy converges within 0.1 mH, which most often requires approximately only three to four iterations.

## 4.4 Quasiparticle calculations within continuum embedding

Inspired by the aforementioned PCM+TDDFT calculations from Section 4.2, here we try a similar embedding approach for quasiparticle calculations within the many-body perturbation theory (MBPT) GW approach. We base our embedding approach, as do the aforementioned TDDFT calculations, on the assumption that the calculated quasiparticle states remain localized around the solute so that the only many-body processes coupling the solute to the environment come through the Coulomb interaction. (e.g. we are assuming that the resulting holes or electrons do not propagate or spread significantly among the solvent molecules.)

The key quantity in the GW approach is the self-energy kernel  $\Sigma$ , which acts as a self-consistent potential in an effective Schrödinger's equation for the quasiparticle states. Within the GW method, this self-energy kernel is expressed in terms of the Green's function  $G_{tot}$  (which, at this stage, includes electronic states for solute and solvent), and the screened Coulomb interaction  $W$  (as opposed to the bare Coulomb interaction  $V_c$ ) in the form

$$W = (V_c^{-1} - \chi_{tot})^{-1}, G_{tot}(\omega) = \sum_i \frac{\Sigma_{tot} = iG_{tot}W}{\omega - \epsilon_i} \frac{|\psi_i^{tot}\rangle\langle\psi_i^{tot}|}{\omega - \epsilon_i}, \quad (4.10)$$

where  $|\psi_i^{tot}\rangle$ ,  $\epsilon_i$  are the quasiparticle states and eigenvalues, respectively, which are generally approximated in practice by the corresponding Kohn-Sham eigenfunctions and eigenvalues.

Next, we consider the simplifications which result from the weak electronic coupling between the solute and solvent. This assumption allows us to take the electron quasiparticle states for solvent and solute to have little overlap. The



Green's function for the entire system then decomposes into regions of local correlations within each subsystem (solvent and solute), and they may then be calculated separately. The portion of the self-energy operator localized to, and thus relevant to the quasi-particles and Green's function in, the solute region is then

$$\Sigma_{sys} = iG_{sys}W, \quad (4.11)$$

where we denote quantities relevant to the region of the solute with the subscript "sys" to indicate that they refer to the explicit system under study. Next, assuming a sharp distinction between the solute and solvent, the charge response of entire system can be expressed as a sum of each subsystem's response function, in the same way as can be the electron Green's function. This allows us to rewrite the screened Coulomb interaction in terms of separate response functions of the solute  $\chi_{sys}$  and solvent  $\chi_{env}$ ,

$$W = (V_c^{-1} - \chi_{sys} - \chi_{env})^{-1}, \quad (4.12)$$

with the subscript "env" denoting the solute as the environment we intend to include implicitly into the calculations. Eqs. (4.11, 4.12) now represent the reduced GW equations to be solved only for the solute, with the *only difference* in the calculation for an isolated and solvated molecule being the presence of the environment dielectric response in the form of the microscopic polarizability  $\chi_{env}$ .

To make the connection to continuum approaches such as PCM, we note that, for PCM methods, the effective Coulomb interaction that plays precisely the same role as  $W$  in Eqs. (4.11, 4.12) is the electrostatic Green's function associated with the following modified Poisson-Boltzmann equation for a given

charge fluctuation  $\delta\rho(r, \omega)$ ,

$$\nabla \cdot (\epsilon(r, \omega) \nabla \delta\phi(r, \omega)) = -4\pi\delta\rho(r, \omega), \quad (4.13)$$

where  $\omega$  is the oscillation frequency,  $\epsilon(r, \omega)$  is the predetermined frequency-dependent dielectric parameter as described in Equation 4.4. Defining this effective Coulomb interaction as  $\tilde{V}_c$ , we then have  $\delta\phi(\omega) \equiv \tilde{V}_c(\omega)\delta\rho(\omega)$ .

The advantage of following the above formal route to Eq. (4.12) is that the identification of  $W$  with  $\tilde{V}_c$  then immediately gives the appropriate generalization of the continuum approach in the GW context. More fundamentally, this allows us to identify, and thereby eventually improve upon, the nature of the implicit approximations which continuum methods make for the microscopic quantity  $\chi_{env}$ . Specifically, transforming the above Poisson's equation to Fourier space, identifying  $\tilde{V}_c \equiv W$ , and employing Eq. (4.12), we find that continuum models correspond to the following choice for the microscopic polarizability

$$\chi_{env}(G, G', \omega) = -(\tilde{\epsilon}(G - G', \omega) - \delta_{GG'}) \frac{G \cdot G'}{4\pi}, \quad (4.14)$$

where  $\tilde{\epsilon}(G, \omega)$  are the Fourier components of the solvent dielectric parameter  $\epsilon(r, \omega)$  in the Poisson's equation above. We do not recommend performing calculations in this matrix form as it is too dense and large to lead to a practical computation. Rather, we consider this form below as a way to identify the failings of, and to improve upon, the continuum approach.

Finally, we comment on a very important practical matter for those, like us, who carry out calculations in plane wave bases that require periodic boundary conditions. Such calculations cause erroneous Coulomb interactions between the solute and its periodic images. In order to avoid such errors, we employ a spherical truncation of the bare Coulomb interaction, as indepen-

dently introduced by Rohlfing *et al.*[88] for the context of vacuum calculations  $V_c(r) \rightarrow V_c(r)\Theta(|r| < R_c)$  or, equivalently, in Fourier space  $V_c(G) \rightarrow G^2(1 - \cos(|G|R_c))/4\pi$ . In the present context, the response function of the modified Poisson Boltzmann equation, Eq. (4.13), must be carefully generalized to reflect the same sort of localization of direct Coulomb effects while leaving the local polarization response intact,

$$G \cdot (\epsilon(G - G') + \delta_{GG'}[\frac{1}{1 - \cos(|G|r_c)} - 1])G'\phi(G') = 4\pi\rho(G), \quad (4.15)$$

where we essentially replace (the inverse of) the long-range Coulomb term  $\delta_{GG'}G \cdot G'/(4\pi)$  from Eq. (4.14) with its truncated version.

## 4.5 Cluster-expanded electronic response

In the above section, we introduced a continuum approach to efficiently include solvent response in the GW method. Such approaches assume the long-wavelength features of the solvent to be the most relevant and develop models to describe it. This section introduces an alternate embedding scheme, which takes the bottom-up approach, starting from local molecular subsystems to construct a response model characterizing the entire solvent.

We begin with the hypothesis of the cluster expansion method, that any property of a given system, the solvent in this case, can be expressed as the sum of contributions from all possible subsystems, appropriately organized into a convergent series. The cluster expansion method has been widely used in the computational chemistry as a way to reduce the intractable problem of extended systems to the tractable problem of finite subsystems[12, 69, 37]. The key, practical factor here is the rate of convergence of the series, which depends solely

upon the interaction strengths between the subsystems. Because closed-shell solvents (such as those we wish to consider) have relatively weak intermolecular electronic interactions, they are natural candidates for this approach.

As mentioned above, the charge response of liquid solvents is represented by the electron-density response function of a collection of solvent molecules, which can be expanded as the following series:

$$\chi_{tot}(r, r') = \sum_{R_i} \chi_{mol}(r - R_i, r' - R_i) + \sum_{R_i \neq R_j} \Delta\chi_{R_i-R_j}(r - R_i, r' - R_j) + \dots, \quad (4.16)$$

where  $\chi_{mol}(r - R_i, r' - R_i)$  is the electron-density response function of an isolated molecule located at  $R_i$ , and  $\Delta\chi_{R_i-R_j}(r - R_i, r' - R_j)$  is the correction to the electron-density response function for a pair (“dimer”) of molecules,  $\chi_{di}(r - R_i, r' - R_j)$ , each of which is located at  $R_i$  and  $R_j$ , computed as

$$\Delta\chi_{R_i-R_j}(r - R_i, r' - R_j) = \chi_{di}(r - R_i, r' - R_j) - \chi_{mol}(r - R_i, r' - R_i) - \chi_{mol}(r - R_j, r' - R_j). \quad (4.17)$$

The physical interpretation of the expansion series in Equation 4.16 is that the first term takes into account the contributions from individual molecules, the second term includes up to di-molecular subunits, and higher-order terms include contributions of even-larger subsets of molecules. It will be shown later in this chapter that the first two terms in the Equation 4.16 are sufficiently dominant to obtain quite accurate results and that even the first term in the series by itself is sufficient to give useful, reliable results.

In practice, we employ plane-wave basis sets, which make it easier to evaluate the summation over subunits in the expansion series. In Fourier space, the first term in the expansion series  $\chi_{tot}^{(1)}$  becomes

$$\chi_{tot}^{(1)}(G, G') = \int dr dr' e^{-iG \cdot r} \sum_R \chi_{mol}(r - R, r' - R) e^{iG' \cdot r'}.$$

In a molecular crystal (or fluid), the molecules will occur not only in different locations, but also in different orientations, and potentially as different species. Labeling these possibilities with the index  $\alpha$ , the above expression simplifies as

$$\begin{aligned}\chi_{tot}^{(1)}(G, G') &= \sum_{\alpha} \sum_{R \in \alpha} e^{-i(G-G') \cdot R} \int dr dr' e^{-iG \cdot r} \chi_{mol}^{\alpha}(r, r') e^{iG' \cdot r'} \\ &= \sum_{\alpha} \left( \sum_{R \in \alpha} e^{-i(G-G') \cdot R} \right) \chi_{mol}^{\alpha}(G, G'),\end{aligned}\quad (4.18)$$

where  $\chi_{mol}^{\alpha}(r, r')$  is the electron-density response function for a molecule of type  $\alpha$ . The sum of subunit response functions in the original expression is reduced to the response function for a single molecule with a structure factor, which clearly can be calculated with less computational costs than the explicit computation of the entire solvent. Moreover, this model response guarantees more reliable short-wavelength features than the continuum approach, for it is constructed from explicit microscopic response functions of the solvent molecules.

Finally, we obtain the single-molecule response function  $\chi_{mol}$  from time-independent perturbation theory (e.g., the RPA approximation) according to the analytic expression[46],

$$\chi_{mol}(G, G') = \frac{4}{\Omega} \sum_{c,v} \frac{\langle v | e^{-iG \cdot r} | c \rangle \langle c | e^{iG' \cdot r} | v \rangle}{\epsilon_v - \epsilon_c}, \quad (4.19)$$

where  $\Omega$  is the volume of the simulation cell,  $|c \rangle, |v \rangle$  represent molecular orbitals for empty (“conduction”) and filled (“valence”) Kohn-Sham states, respectively,  $\epsilon_c, \epsilon_v$  are the corresponding eigenvalues, and the factor of four accounts for spin and time-reversal symmetry.

## 4.6 Test on the cluster expansion method for the electronic response function

The previous section showed how to evaluate efficiently an approximate model microscopic response function for a system of molecules. As a way to verify the accuracy of the resulting response model, we compare the approximate response model against the explicit response by comparing quasiparticle energies.

Our test system consists of a cluster composed of five  $\text{H}_2\text{O}$  molecules sitting at the molecular sites of an ice crystal (in the Ic phase). Because the hydrogen bond is the strongest amongst intermolecular electronic interactions without actual chemical bonding, such a system represents a challenging test case for our microscopic response model. In order to determine the effect of including the pair correction terms, as well as the reliability of including only the first term in Eq. 4.16, we calculate the ionization potentials and HOMO-LUMO gap of a cluster of five  $\text{H}_2\text{O}$  molecules, arranged with their oxygen atoms at the corners and the center of a tetrahedron and with hydrogen atoms obeying the ice rules for hydrogen bonding, as shown in Figure 4.1.

For this demonstration we compare density-functional theory (DFT) results with the GW-COHSEX results taking the environment response calculated from (a) the cluster expansion truncated at the level of single molecules, (b) the cluster expansion truncated at the level of single and pairs of molecules, (c) the full cluster without approximation. The COHSEX approximation assumes that the electronic response is purely frequency-independent. This approximation is a standard treatment used in the literatures for evaluating the convergence properties of excited state calculations[101, 11] because, even though the COHSEX

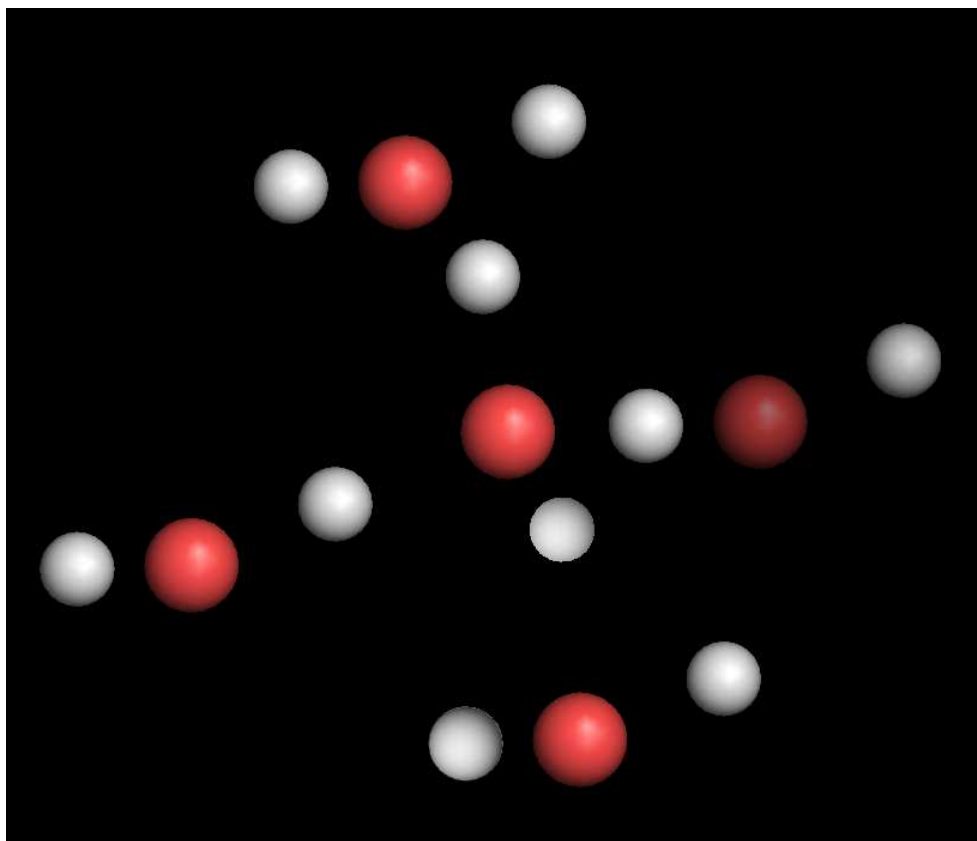


Figure 4.1: The atomic configuration of five  $\text{H}_2\text{O}$  molecule cluster, with oxygen atoms at vertices and center of a tetrahedron, and hydrogen atoms obeying the ice rules for hydrogen bonding, as a test system to verify the accuracy of response model: oxygen atoms (red), hydrogen atoms (white).

approximation is known to somewhat underestimate correlation effects, it contains sufficient amounts of the key many-body effects (exchange-correlation and local fields) to give good understanding of the convergence of different expansion methods.

Table 4.1 presents both the ionization potential (i.e., the quasiparticle energy of the highest occupied molecular orbital (HOMO)) and the HOMO-LUMO gap (i.e., the difference between the HOMO and the lowest unoccupied molecular orbital (LUMO) levels) as computed within the above models for the response function  $\chi$ . Due to well-known flaws in the local density approximation (LDA)

Table 4.1: Ionization potential (HOMO level) and HOMO-LUMO gap as computed within DFT (DFT) and within the static COHSEX using the microscopic polarizability computed as a sum of single molecule contributions (Single), as a sum of single molecule contributions plus pair corrections (Single+Pair), and computed directly for the entire cluster (Exact).

Molecular response	Ionization potential(H)	HOMO-LUMO gap(H)
DFT	-0.156	0.077
Single	-0.290	0.294
Single+Pair	-0.273	0.266
Exact $\chi$	-0.277	0.277

of the exchange-correlation effect for electrons, both the ionization potential and the HOMO-LUMO gap are underestimated in the density functional calculations as compared to the GW method. The GW-COHSEX calculations, indeed, clearly recover significant portions of the missing exchange-correlation effects, doubling the ionization potentials. We find that the response model constructed from single molecular contributions only already recovers up to 90% of the final GW result. Including the pair correction terms brings in another 5% of the effect, capturing 95% of the final GW result. Given the additional computational costs of including the pairs and the fact that the single molecule terms already capture 90% of the GW result, we in the next chapter will focus on calculations employing only single molecule terms in the cluster expansion.

## 4.7 Summary

This chapter explores the formal underpinnings for two different schemes accounting for environmental dielectric screening effects, the continuum dielectric model and the molecular embedding, and explores how to incorporate these approaches into modern quasiparticle calculations within many-body perturba-



tion theory.

The continuum embedding method, which employs a continuous dielectric function in Poisson's equation to represent electrostatic response of solvent, already has been used widely to calculate equilibrium states and optical excitations (TDDFT). Here we show how to incorporate this approach into the GW method, a Green's function based approach which allows us to capture both optical and electron excitations and is applicable to various systems for which TDDFT is known to fail.

As a way to evaluate the reliability of the continuum embedding approach for calculating quasiparticle states, and to potentially improve upon it, we then considered a more direct, molecular embedding approach. This new approach employs the effective potential (for equilibrium states) and the RPA response function (for excited states) of the solvent molecules directly into the calculations. Inspired by the cluster expansion approach of quantum chemistry, we show how to expand the RPA response function of the solvent in a series whose leading term is, simply, a sum of the microscopic dielectric response of individual solvent molecules. This approach demands far less computational power than the explicit evaluation of the entire solvent response. We further show that, in a test involving a small clusters of  $\text{H}_2\text{O}$  molecules, the first one or two terms of the series are sufficiently dominant to yield the quasiparticle energies close to those calculated with the full explicit response function, with the first term yielding 90% of the GW correction and the second term another 5%. The next chapter will apply these embedding approaches to calculate solvation effects on the quasiparticles states of small organic molecules dissolved in water.

## CHAPTER 5

### APPLICATION TO SOLVATED ORGANIC MOLECULES

In this chapter, we present detailed calculations of the quasiparticle states of solvated molecules with the effective solvent models introduced in the previous chapter. Specifically, we investigate the accuracy of two different embedding methods for predicting experimental quantities within the GW method. We begin with the polarizable continuum model (PCM), as implemented in the joint density-functional theory (JDFT) form, as a computationally efficient treatment for liquid environments. We also consider the molecular embedding method, which includes the single-molecule terms from the cluster expansion that the previous chapter showed to capture 90% of the final result computed with the explicit response function. This method has the clear advantage of being derived from the microscopic response of the liquid and thus containing its full molecular details. We then explore the connections between these two methods, finding that the solvent contribution in the GW calculations is surprisingly close for the two methods despite the fact that they stem from very different approaches to the solvent response.

The latter observation supports the reliability of the PCM solvent description at least for the polarization response of the solvent, which is the most important contribution of the environment in the GW method. It also opens the door to the possibility of combining the two solvent models in some way as to maintain the computational efficiency of the continuum approach and the higher accuracy of the molecule embedding approach. Specifically, using the formal connections we made in the previous chapter between the PCM and molecular based approaches, we find that the solvent response function implicit in the two

methods show remarkable agreement at long wavelengths, thus providing the first explanation for the relative accuracy of the original PCM approach. Finally, these connections point us to an approach for correcting the short-wavelength interactions to improve upon the accuracy of the PCM *by over a factor of three* with relatively little additional computational cost.

As test and demonstration systems, we consider a series of small organic molecules dissolved in liquid water. In this context, we find that our modified GW method captures substantial amounts of the solvent shift in the ionization potential and reproduces the general trend in the magnitude of the solvent shifts. For the molecular embedding method, we consider an ice crystal to allow connections to be made to the aqueous PCM results. This connection is possible because one may consider each molecule in liquid water as a solute and because the hydrogen bond network in liquid water forces local arrangements not too dissimilar from those in ice. For this system, we focus on ionization potential shifts from the gaseous to the “solvated” crystalline phase.

## 5.1 Overview of embedded GW method

We calculate the quasiparticle energy for each solvated system in a three step procedure. First, (1) we obtain the equilibrium state of the combined solute-solvent system with density functional-theory, representing the solvent through either joint-density functional theory or the orbital-free embedding method of Section 4.2 and Section 4.3, depending on whether we are pursuing a continuum or explicit molecular description of the environment, respectively. This equilibrium state is obtained by self-consistent iteration of the following two-step sub-procedure,

- the free energy functional, restricted to the solute and containing the effective Hamiltonian representing the solvent, is minimized to compute the solute electron density;
- the effective solvent Hamiltonian is updated with the computed solute electron density.

We find that this procedure typically requires about ten iterations to reach a convergence of the total energy within  $10\mu\text{H} = 0.27\text{meV}$  for the solvated molecules considered here. Next, (2) we use the self-consistent solute Hamiltonian from step 1 to evaluate a complete set of Kohn-Sham orbitals and eigenvalues for the solute. Finally, (3) from these orbitals and eigenvalues, we construct  $\chi$  and the associated screened Coulomb interaction kernel  $W$ , and compute the self-energy correction for each quasiparticle state within the GW framework.

Simply replacing the quasiparticle wave functions and energies appearing in the Green's function  $G$  with the Kohn-Sham eigenstates and eigenvalues from DFT calculations has been well-established as an accurate approximation in many GW calculations for semiconducting materials. However, recent studies[25, 107] suggest that performing iterative updates for the quasiparticle states, a method termed self-consistent GW, leads to significant improvements for systems such as molecules which have localized states. At present, our primary concern is to demonstrate the inclusion of solvent effects within the GW method, and not to explore the issue of the importance of self-consistent GW. Accordingly, we take a middle-ground approach and iteratively update the orbital energies but leave the quasiparticle states as approximated by the corresponding Kohn-Sham orbitals. (Fully self-consistent GW with orbital updates is extremely computationally intensive.)

A second technical issue of concern in GW calculations is that the electron Green's function  $G$  involves an infinite sum over a complete set of quasiparticle orbitals. This sum involves a linear energy denominator and, consequently, converges rather slowly. Nonetheless, the GW self-energy kernel is heavily dominated by the first few hundred states of lowest energy. Consequently, the higher states with relatively large energy are often truncated and removed from the sum[95, 32], or replaced with approximate forms such as plane waves[13]. In our case, as again our focus is on the inclusion of solvent effects within GW and not issues with the GW method itself, we ignore the higher states and limit the summations to the two hundred lowest states in energy.

## 5.2 Calculations

### 5.2.1 Computational Details

Our density functional-theory calculations represent the ionic cores with Rappe-optimized norm-conserving pseudopotentials[53, 86] and exchange correlation effects within the local density-approximation (LDA) as parameterized by Perdew and Zunger[81]. A plane-wave basis with a cutoff energy of 20 H expands the Kohn-Sham orbitals, and, because we deal with isolated molecules, only 1 k-point (at  $\Gamma$ ) is needed to sample the Brillouin zone of the simulation cell. Our supercells are cubic boxes of sizes 30 bohr for isolated molecules or 24 bohr for the ice crystal calculations, which contain  $4 \times 4 \times 4$  primitive FCC cells of the ice structure. The resulting energy functional is minimized with the analytically continued conjugate gradient method[5] using the JDFTX software

package[100]. For the GW calculations, we represent the microscopic electron response matrix  $\chi$  with a plane-wave basis of cutoff 10 H, corresponding to  $\sim 21,000$  and  $\sim 41,000$  basis vectors in the 24 bohr and 30 bohr boxes, respectively.

Since we always deal with neutral molecules within the DFT calculations, the interactions of molecules with their periodic images are strongly screened and no correction is needed. The quasiparticle states in the GW calculations, on the other hand, have nonzero charge, and this interactions must be corrected. As described in Chapter 4, we employ a spherical truncation of the Coulomb potential[88],  $V_c(r - r') = \frac{1}{|r - r'|} \Theta(|r - r'| < R_c)$ , where  $R_c$  is the cutoff radius, chosen so that the molecule in question fully interacts with itself but feels no influence from its periodic images. Section 4.4 of Chapter 4 further describes how this must be generalized when the molecule sits within a dielectric screening environment. An appropriate cutoff radius satisfying the above conditions is obtained near the half size of the dimension of the simulation cell. In particular, we employ  $R_c = 15$  bohr when working with the 30 bohr cubic cell, and  $R_c = 12$  bohr for the molecular embedding solvent in a 24 bohr cubic cell.

## 5.2.2 Summary of studies

To explore the accuracy of our continuum solvent descriptions, we employ as test systems the series of small molecules  $\text{NH}_3$ ,  $\text{H}_2\text{O}$ ,  $(\text{CH}_3)_2\text{CO}$ ,  $\text{H}_2\text{CO}$ , all of which are known to dissolved easily in liquid water. As described in the introduction to this chapter, for exploration of the molecular embedding method, we replace the liquid environment with a crystalline form of ice, ice Ic. We make

this choice for practical reasons, namely relieving us from the complications of sampling molecular configurations in liquid water while still exploring a structure with the same hydrogen bonding tendencies as liquid water.

Below, we present the following computational studies for the above systems. First, Section 5.3 assesses the environmental effect on the equilibrium state of the solute by computing the Kohn-Sham eigenvalues of the top valence orbitals with and without the solvent models. Moving next to the many-body perturbation theory (MBPT) predictions, in Section 5.4 we establish baseline vacuum results for the quasiparticle states of the above series of molecules. Section 5.5 and Section 5.6 then present environmental screening as computed within our continuum embedded and molecularly embedded GW approach, respectively. Finally, Section 5.7 explores the details of the microscopic polarization response function  $\chi$ , resolves which of its Fourier components determine the excitation spectrum of the solute, and compares how those components behave in both the continuum and molecular embedding cases. This section then ends with a proposal and demonstration of how to improve upon the continuum approach to mimic the correct microscopic response for the relevant Fourier components. This allows us to present a new, significantly more accurate (by over a factor of three!) and, yet still, computationally efficient approach to embedded quasiparticle calculations.

### **5.3 Environmental effects on the equilibrium state**

The equilibrium calculation in the density-functional theory framework yields directly the Kohn-Sham orbitals and eigenvalues for the electrons in the filled

(valence) states of the system, and also the electron density and the single-particle Hamiltonian. This Hamiltonian, in turn allows computation of the empty (conduction) states, which are needed in the construction  $W$  through  $\chi$  and in the construction of Green's function  $G$  determining the self-energy operator  $\Sigma = iGW$ . Consequently, the equilibrium DFT calculation and its resulting states and eigenvalues represent key inputs into the final many-body GW calculations.

At the level of such the equilibrium density-functional theory calculations, as described in Section 4.2 and 4.3 of Chapter 4, environmental effects are included into the single-particle Hamiltonian either by computing all electrostatic interactions (electron-ion, electron-electron, and ion-ion) in an effective continuum dielectric or by computing the effective potential accounting for the electrons and nuclei of the environment molecules. Accordingly, we begin our analysis by exploring the effects of each of these approaches on the single particle Hamiltonian.

We first consider the continuum method, in which the solvent effect is characterized by the screening of the electrostatic potential. Figure 5.1 displays the environment-induced potential (difference between the screened and bare Coulomb potentials) for the case of an  $\text{H}_2\text{O}$  molecule solvated in a dielectric description of liquid water. The figure shows, as is to be expected, a clear build up of negative and positive charges (as reflected in negative and positive electrostatic potential contributions, respectively) near the protons and oxygen ions, respectively. The strong localization of induced charges in the solvent to the vicinity of the molecule reflects the fact that liquid water, with its large static dielectric constant  $\epsilon_b \approx 80$ , strongly screens any external Coulomb potentials.



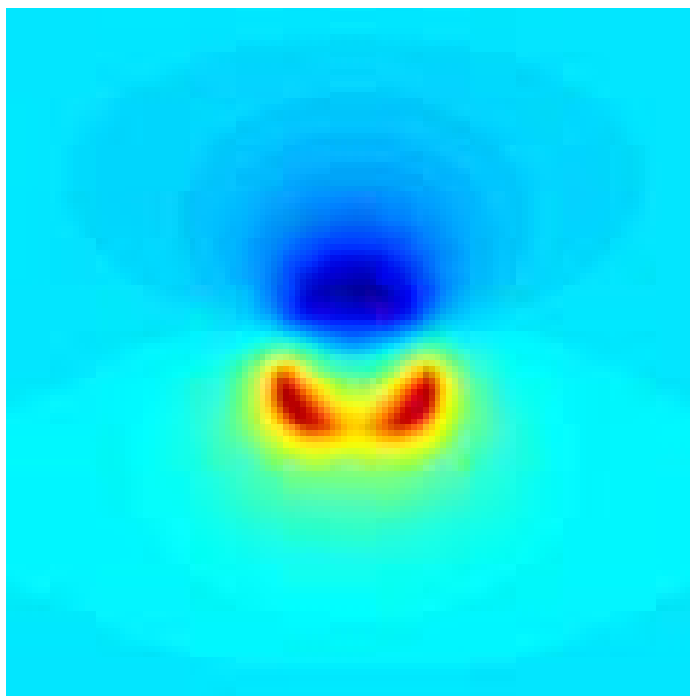


Figure 5.1: Electrostatic potential induced by environment for  $\text{H}_2\text{O}$  molecule solvated in liquid water as described by a polarizable continuum: from negative or repulsive to electrons (red) to positive or attractive to electrons (blue). Screening potential near the protons is repulsive to electrons because the screening potential has the opposite sense from the potential of the molecule itself.

Next, we consider the same induced potential as determined within the molecular embedding view of the environment. Figure 5.2 shows the iteratively converged environment potential determined from the orbital-free embedding method according to Equation 4.5 for crystalline ice Ic as the model environment. Here, the solvent molecules are placed in an ordered structure and contribute to the repulsive potential peaks (which are truncated for better visualization and thus shown here as yellow circles), due mainly to the exclusion principle between solute and solvent electrons, as described by the Thomas-Fermi

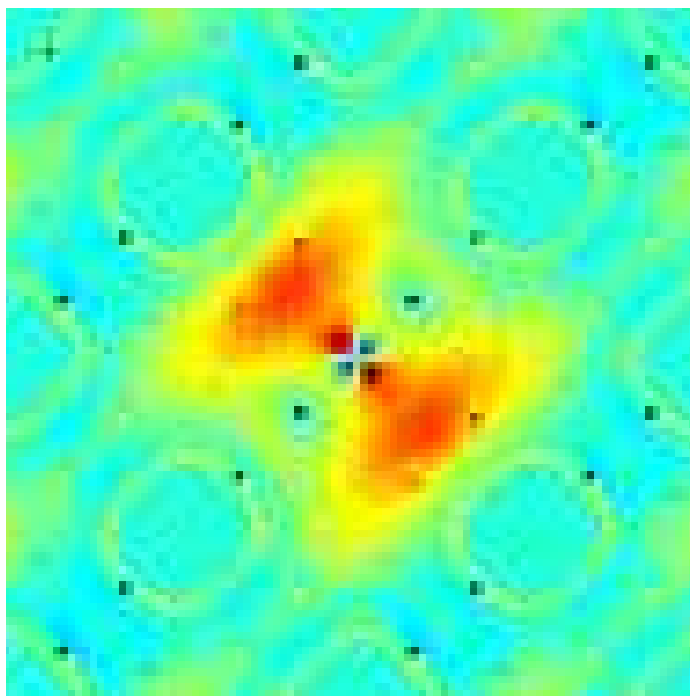


Figure 5.2: Coupling potential between  $\text{H}_2\text{O}$  molecule and remaining molecules of ice Ic crystal computed within the orbital-free embedding method: attractive (blue) and repulsive (red) to electrons. Yellow circles are traces of Thomas-Fermi repulsive potential peaks truncated for better visualization.

kinetic energy functional (Equation 4.8). In this case, the solvent potential draws electrons to the hydrogen bonding sites, making them appear as light blue peaks in the figure. Beyond the large repulsive potentials on the oxygen sites and the polarization phenomena near the explicit molecule, a subtle, but important, difference between the continuum and molecular-environment potentials is a large positive constant shift in the potential from the molecular embedding method relative to that of the continuum approach. This shift, due to the pattern of Coulomb potentials from the solvent molecules, a “local molecular field effect”, leads to a significant solvent shift in the orbital energies which also appears in

Table 5.1: Density functional-theory results for the ionization potential of H<sub>2</sub>O molecule in vacuum and in a full water environment as calculated explicitly (Ice Ic at  $\Gamma$  point), and with molecular (Molecular) and continuum (Continuum) embedding. Results given for both the energy of the HOMO level (Ionization potential) and the shift in this level upon solvation within the various descriptions.

Environment	HOMO eigenvalue (H)/ (Ionization potential)	Shift from Vacuum
Vacuum	0.268	–
Continuum	0.254	0.014
Molecular	0.188	0.080
Ice Ic	0.174	0.090

the energy levels from the full, explicit crystal calculation.

With the effective Hamiltonians determined, we now consider the resulting solvation effects on the energy of the solute orbitals. The energy of the highest occupied molecular orbital (HOMO) gives the ionization potential (IP), which is measurable from photoelectric emission experiments. Table 5.1 presents the HOMO levels of an H<sub>2</sub>O molecule as determined from density-functional theory calculations for vacuum and both of our solvent models. The table also compares these levels to a full calculation of the molecular crystal for a direct comparison with the exact result expected within the density-functional theory<sup>1</sup>. Within these equilibrium state calculations, the continuum method significantly underestimates the solvation shift of embedding the molecule in the bulk structure (capturing only  $\sim 15\%$  of the shift), whereas the molecular embedding approach captures most of it ( $\sim 85\%$ ). We believe that the shift at this level is due mostly to the constant shift throughout the supercell associated with the Coulomb potential of the environment with the molecular arrangement, a

<sup>1</sup>The experimental IP value for H<sub>2</sub>O in vacuum is 0.46 H=12.6(1) eV[78]. The underestimation by over a factor of two relative to experiment corresponds to the well-known “band-gap” problem of density-functional theory. GW calculations were developed precisely to address this issue. Section 5.4 below will make comparison between experiment and the GW calculations.

Table 5.2: Comparison of vacuum DFT and GW results for ionization potentials (eV) of various molecules with experimental data.

Molecule	DFT	Our GW	Other many-body works	Experiment[78]
H <sub>2</sub> O	7.29	11.97	12.5 (GW)[39]	12.5-12.7
(CH <sub>3</sub> ) <sub>2</sub> CO	5.69	9.03		9.69
NH <sub>3</sub>	6.28	9.96	10.7 (GW)[50]	10.18
H <sub>2</sub> CO	6.14	10.15	10.83 (CCSD)[68]	10.88

“local molecular field effect”, which is absent in the continuum approach.

## 5.4 GW in vacuum

With the Kohn-Sham orbitals and eigenvalues in hand, the next step in the quasiparticle calculations (including the ionization potential) is to construct the self-interaction kernel within the GW approximation,  $\Sigma = GW$ , and compute the energies of the quasiparticle states by adding the self-energy correction to the Kohn-Sham eigenvalues. Although there are a few publicly available software packages for GW calculations, for example, BerkeleyGW[24] and Abinit[14], none of them provide the capability to include solvation effects in quasiparticle calculations. Accordingly, we had to develop our own codes to incorporate the solvent treatments into the GW calculations.

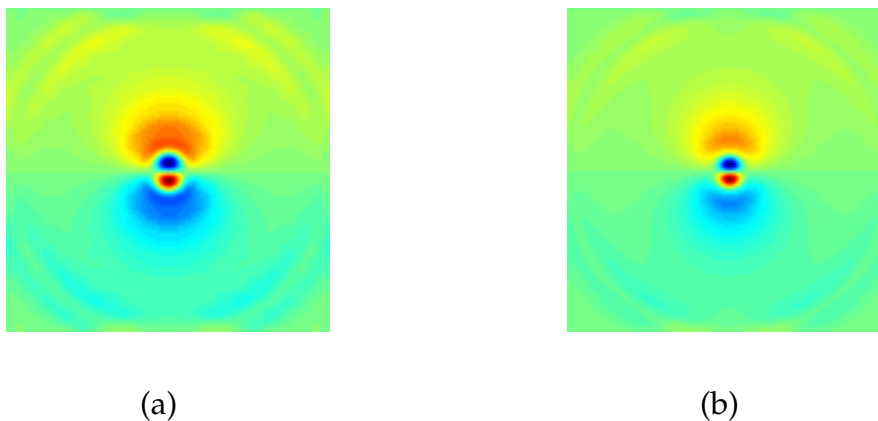
In order to benchmark the accuracy of the our GW codes against other standard packages and to allow calculation of solvation shifts in quasiparticle energies, we first compute the GW quasiparticle states of the non-solvated versions of our target systems, in this case the series of small polar molecules NH<sub>3</sub>, H<sub>2</sub>O, (CH<sub>3</sub>)<sub>2</sub>CO, H<sub>2</sub>CO, which we choose for the availability of both experimental data[78] and other GW calculations[39, 50, 68].

Table 5.2 compares the HOMO quasiparticle energies (ionization potentials) in vacuum of each of the above molecules as calculated within density-functional theory, our own GW software, available many-body results from the literature (primarily GW, but some quantum-chemistry coupled-cluster results as well) with the ionization potential from experiments. Our quasiparticle energies agree well with both the experimental values and other many-body works for all of the four molecules. The average error with respect to the experimental values is 0.5 eV, corresponding to 13% of the average GW correction (3.92 eV) with respect to the Kohn-Sham orbital energy. We consider this to be in an acceptable range regarding that only 200 Kohn-Sham states are included in the GW calculation, and that the typical error for ionization potentials for standard GW calculations (without advanced techniques such as self-consistency, off-diagonal corrections, or approximate analytic summations over an infinity of empty states) is a few tenths of an electron volt. (We also note that our inclusion of only 200 empty states for these exploratory calculations is also not sufficient for full convergence.) Because our primary focus in this work is to explore the inclusion of solvent effects in the GW calculations, at this stage we do not consider further improvements to our GW calculations.

## 5.5 GW within polarizable continuum models

We next explore solvent effects on quasiparticle states by integrating continuum embedding within our GW calculations. On the basis of the Kohn-Sham states computed in Section 5.3 and the response function of Eq. (4.14) from Section 4.4, we construct the fully screened Coulomb kernel  $W$  as we do for the vacuum case, but now with the inclusion of  $\chi_{env}$ , in addition to  $\chi_{sys}$  as computed in

Figure 5.3: Screened potential fluctuations associated HOMO-LUMO transition for  $\text{H}_2\text{O}$  molecule viewed in plane perpendicular to molecular plane: gaseous state (a), solvated state (b). Outer circular feature at the edges of the supercell is due to spherical truncation of Coulomb interaction to avoid image effects. Plane of figure passes through center of the oxygen atom and is perpendicular both to the plane containing the atoms of the molecule and to the perpendicular bisector between the hydrogen atoms of the molecule.



Eq. (4.19).

To explore the solvent effect on the GW results, Figure 5.3 compares the screened interaction  $W$  for a  $\text{H}_2\text{O}$  molecule in both its gaseous state and solvated state computed within the continuum approach. For visualization purposes, we plot the action of  $W$  on the charge fluctuation  $\delta\rho$  associated with a typical optical excitation, specifically the HOMO-LUMO transition, in the static limit  $\omega \rightarrow 0$ . This particular charge fluctuation results in a dipole perpendicular to the plane containing the atoms of the molecule, which is oriented in the vertical direction in the figures. Comparing Figure 5.3(a) with Figure 5.3(b) shows that the potential field in the liquid phase, compared to the gaseous phase, is noticeably more localized near the molecule and is less intense as the response field of the environment tends to cancel the local polarization.

Table 5.3: Ionization potential for molecules solvated in liquid water as determined within the continuum solvation approach at the density-functional theory (DFT) and GW levels and compared to estimates from experimental data (Pearson)[78].

Molecule	DFT	Our results(GW)	Pearson's estimate
H <sub>2</sub> O	6.9	9.9	8.0
(CH <sub>3</sub> ) <sub>2</sub> CO	5.8	7.5	7.1
NH <sub>3</sub>	6.1	8.0	6.1
H <sub>2</sub> CO	5.9	8.2	None

Next, we turn to the effects of this screening on quasiparticle energies. Unfortunately, direct measurement of the ionization energy is not available for solute molecules dissolved in solvent, because the incoming radiation is absorbed by and ionizes the solvent before reaching the solute molecules. For making comparisons, we here instead employ estimates given by Pearson[78] in which the shift for the ionization potential is calculated from the free energy of hydration of neutral molecules and protonated ions, and the protonation energy of the same molecules in both their gaseous and aqueous phases. This procedure is not a direct measurement and makes a number of assumptions about the effects of protonation on ionization potentials and therefore is subject to some error. Nonetheless, these are the best data we have available, and we believe that the data from Pearson give at least qualitatively reasonable values for the solvent effects we study here.

Table 5.3 presents the computed solvated HOMO energies for each molecule in our test suite and compares them with Pearson's estimate (with the exception of H<sub>2</sub>CO which is known to combine with H<sub>2</sub>O molecules and form oligomers in water). While density-functional theory significantly underestimates the ionization potential (as expected from the previous results for the gaseous phases of these molecules), the GW method significantly overestimates the ionization

potential with respect to Pearson's free energy estimates. In an absolute sense, the GW results for the ionization potentials do not seem a significant improvement, especially for the case of  $\text{NH}_3$ . However, there is significant potential here for partial cancellation of errors as we look to solvatochromic shifts (change in exciton frequency upon solvation), which are of more direct experimental interest.

Table 5.4 presents these shifts in ionization potential for each molecule upon solvation from the gaseous state. These data underscore the failure of density-functional theory in capturing such solvent shifts: the shift is severely underestimated by at least an order of magnitude, and even exhibits the incorrect sign for the case of  $(\text{CH}_3)_2\text{CO}$ . This indicates that the apparent agreement of the solvated ionization potentials computed within density-functional theory is a coincidental cancellation of errors: the DFT ionization potentials are too small due to the well-known gap problem, an effect which happens to match the magnitude and sign of the solvation shifts that the embedded DFT calculations give as essentially zero. The shifts in the GW method, on the other hand, are a significant improvement, capturing about half of the effect (if Pearson's estimated values are to be taken *quantitatively*). Moreover, the relative order in the solvent shifts is consistent for all molecules for which there are estimates from Pearson,  $(\text{CH}_3)_2\text{CO}$ ,  $\text{NH}_3$ , and  $\text{H}_2\text{O}$ , in order from the smallest to the largest shift. Because the ionization potential shift comes from solvent polarization affecting the electron correlation of the solute, such consistency suggests that the GW+PCM method is able to capture significant portions of the charge response of the solvent and its dependency on the solute.

The apparent underestimation of the solvent shift relative to the Pearson's



Table 5.4: Ionization potential shifts from the gaseous state for molecules solvated in liquid water, as determined within the continuum solvation approach at the density-functional theory (DFT) and GW levels and compared to estimates from experimental data (Pearson)[78].

Molecule	DFT	Our results(GW)	Pearson's estimate
H <sub>2</sub> O	0.4	2.1	4.6
(CH <sub>3</sub> ) <sub>2</sub> CO	-0.1	1.5	2.6
NH <sub>3</sub>	0.2	2.0	4.1
H <sub>2</sub> CO	0.3	2.0	None

estimates for the ionization potential may stem either from a number of areas of concern in our approach or from difficulties in Pearson's approach. The later approach determines the ionization potential shift by comparing the solvation energy of neutral and ionized molecules from their gaseous phases (where the ionization potential is known). The free energy of the ionized molecules in solution are then *estimated* to be the same as the known results for the protonated molecules, *i.e.*  $G(B^+(aq)) \approx G(BH^+(aq))$ , but the free energy of the protonation process itself and its effects on the estimated ionization potentials are not known.

In terms of potential errors from our method, there are two areas of concern. First, when the electronic states of the solute and solvent systems couple strongly, our initial representation of the Green's function localized on a single explicit molecule as in Eq. (4.11) breaks down. Second, the description of the Coulomb coupling to the environment, as characterized by  $W$  in Figures 5.3, may lack sufficient microscopic detail to give an accurate picture of the dielectric screening.

Mitigation of the above two areas of concern suggests two strategies for improvement. The first area of concern, coupling of electronic states to the en-

vironment, would clearly apply to the case of the solvation of  $\text{H}_2\text{O}$  molecules, which form a hydrogen-bonding network with the surrounding  $\text{H}_2\text{O}$  molecules in liquid water. One direct approach to mitigating this source of error would be to increase the number of molecules included in the explicit parts of the calculation and consider a cluster containing a few solvent molecules, as is sometimes done in combined molecular-dynamics GW studies[42]. Pursuing such an approach is beyond the scope of this thesis. The second area of concern, insufficient description of the Coulomb coupling to the environment, can be mitigated by including additional molecular detail in the environment response function, as we do in the next section.

## 5.6 Molecular embedding for the excited states

Next, we turn to the combination of the GW method with a molecular model for the environment response function  $\chi_{env}$ , computing it within the cluster expansion at the single-molecule level, which Section 4.5 showed to capture 90% of the solvation effect. For our test system, we consider a crystalline form of ice (the Ic phase) which satisfies the hydrogen bonding constraints and thus produces a structure reminiscent of what is found in liquid water. This choice is made as a matter of convenience for this initial exploration of the method. The advantage is that no phase space-sampling or averaging is needed to determine the structure, as it would be in the case of the liquid. One disadvantage, noted at the very end of the previous section (Section 5.5), is that comparison of the final solvation shift to the experimental data may still suffer due to coupling of the electrons from one molecule to the next.

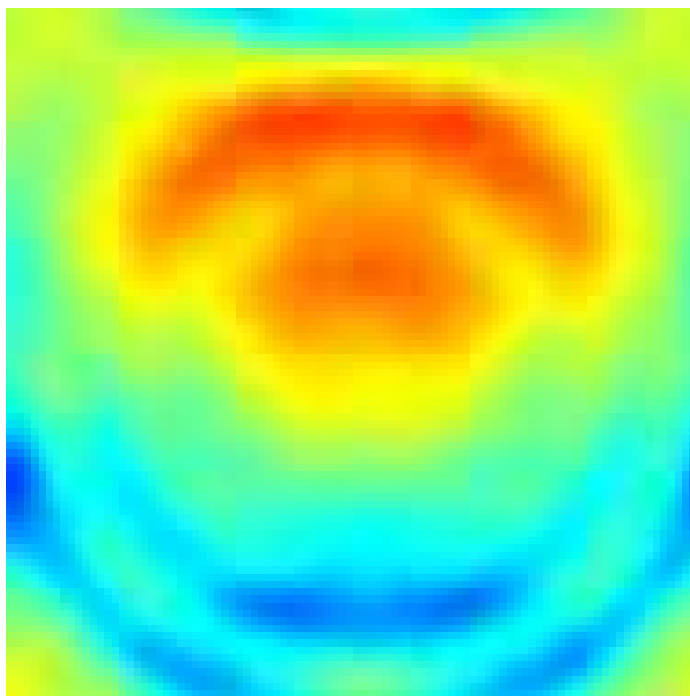


Figure 5.4: Screened Coulomb potential associated with HOMO-LUMO charge fluctuation for solvated H<sub>2</sub>O molecule as calculated from molecular  $\chi_{env}$ . Geometry of plane the same as in Figure 5.3. Inner features correspond to shell structure of the ice crystal, outer rings correspond to truncation of Coulomb interaction as in Figure 5.3.

Figure 5.4 displays the potential fluctuation in the ice crystal,  $\delta\phi = W \delta\rho$ , where  $W$  is the full, screened Coulomb interaction and the charge fluctuation  $\delta\rho$  is from the HOMO-LUMO transition, the lowest vertical transition mode of the solute molecule in the center of the figure. Compared to the gas-phase (Figure 5.3), the potential near the solute is significantly weakened by the screening of the molecular environment. In contrast to the continuum screening model (Figure 5.3 (b)), the more realistic molecular model shows a greater spread of the potential into the surrounding regions because the screening, rather than being uniform, is now concentrated near the atomic locations and requires coherence

Table 5.5: Ionization potential (HOMO energy level) of H<sub>2</sub>O molecule in vacuum, and embedded either in a continuum dielectric or model molecular crystal (ice Ic), as computed with DFT and the GW approach. Final column gives the resulting solvation shift for the total GW result, and final row repeats the data from Pearson’s estimate.

	DFT (eV)	GW (eV)	Total shift (eV)
Vacuum	7.3	12.0	
Continuum	6.9	9.9	2.1
Molecular	5.1	8.2	3.8
Free energy estimate[78]		8.0	4.6

Table 5.6: Solvation shifts for individual contributions (DFT and the GW self-energy correction added to the DFT result) and total ionization potential (HOMO level) for H<sub>2</sub>O molecule embedded either in a continuum dielectric or model molecular crystal (ice Ic), as computed with DFT and the GW approach. Final row repeats the data from Pearson’s estimate.

	DFT (eV)	GW self-energy (eV)	Total shift (eV)
Continuum	0.4	1.7	2.1
Molecular	2.2	1.6	3.8
Free energy estimate[78]			4.6

across several shells of neighboring molecules to reach the full screening effect.

With the behavior of the screening potential  $W$  understood, we now turn to the quasiparticle energies. Table 5.5 shows the final results for the ionization potential for the molecule in the center of our crystalline cell as computed within density-functional theory and the GW approximation for vacuum and both the continuum and molecular embedding approaches, comparing the results with Pearson’s estimates. The molecular embedded GW approach indeed does a much better job capturing the shift from vacuum, capturing  $3.8 \text{ eV} / 4.6 \text{ eV} = 83\%$  of the effect (as opposed to  $2.1 \text{ eV} / 4.6 \text{ eV} = 46\%$  of the effect captured in the continuum case).

Table 5.6 gives the solvation shift associated with each of the individual con-

tributions (DFT or the GW self-energy correction) to the final shift for both our continuum and molecular embedding approaches. This decomposition indicates, interestingly, that, although the GW shift is important for producing the final result, most of the improvement from the molecular embedding approach comes at the DFT level of the calculation, with the GW self-energy correction being quite similar in both the continuum and the molecular embedding cases.

In terms of the DFT correction, the major difference between the two solvent models, as observed in Section 5.3 with the explicit crystal calculation, is a basic shift in the potential at the location of the solute molecule due to the local electric fields from the molecules making up the environment. We conclude that this “local molecular field effect” is the principal solvent correction which the molecular embedding brings to the calculation of solvation shifts. We propose, therefore, that an efficient and accurate method for computing solvation shifts would be a hybrid method of carrying out the relatively inexpensive DFT calculations within the more complex molecular environment and then computing the much more computationally intense GW corrections within the simpler, more efficient continuum approach.

## 5.7 Analysis of the solvent response function

The previous section showed that, despite their starkly different origins, our two treatments of the solvent dielectric response yield substantially similar contributions in the GW quasiparticle energy. This section explores the deeper reasons for this apparent coincidence and uncovers a path to improve the continuum dielectric approach by generalizing to non-local dielectric functions. To

connect the two approaches, we consider the corresponding forms for the microscopic polarization response function  $\chi_{env}(G, G')$ , either from superposition of molecular contributions, Eq. (4.18), or in the form implicit in the continuum approach, Eq. (4.14).

We begin by determining which components of the response function  $\chi_{env}(G, G')$  are the most important to the final result. As a measure of this, we consider the screened Coulomb interaction of the HOMO (the top “valence” orbital in condensed-matter parlance) with itself, a major contributing factor to the GW correction. Specifically, this quantity is  $\langle \rho_{vv} | W(\omega) | \rho_{vv} \rangle$ , where  $\rho_{vv} = \psi_v^\dagger \psi_v$  is the electron density associated with the top valence orbital. At the lowest order, the effect of this environment response function is then,

$$\begin{aligned} \langle \rho_{vv} | V_c \chi_{env} V_c | \rho_{vv} \rangle &= \sum_{G, \Delta G} [V_c \rho_{vv}]_G^\dagger \chi_{env}(G, G + \Delta G) [V_c \rho_{vv}]_{G+\Delta G} \\ &= \sum_{G, \Delta G} \chi_{env}(G, G + \Delta G) \tilde{\phi}(G, \Delta G), \end{aligned}$$

where  $\tilde{\phi}(G, \Delta G) \equiv [V_c \rho]_G^\dagger [V_c \rho]_{G+\Delta G}$  can now be thought of as a weight factor determining the importance of the component  $\chi(G, \Delta G)$  in the self-energy correction. For a given momentum transfer  $\Delta G$ , we may then define a weighted average susceptibility  $\langle \chi_{env} \rangle (\Delta G)$  as

$$\langle \chi_{env} \rangle (\Delta G) = \frac{\sum_G \chi(G, G + \Delta G) \tilde{\phi}(G, \Delta G)}{\sum_G \tilde{\phi}(G, \Delta G)}. \quad (5.1)$$

Finally, we can define the sum of potential fluctuation weights for a given momentum transfer as

$$\langle \tilde{\phi} \rangle (\Delta G) = \sum_G \tilde{\phi}(G, \Delta G).$$

We then may compute the screened Coulomb self-energy of the valence orbital (to the lowest order in the environment response) as simply the sum

$$\langle \rho_{vv} | V_c \chi_{env} V_c | \rho_{vv} \rangle = \sum_{\Delta G} \langle \chi_{env} \rangle (\Delta G) \langle \tilde{\phi} \rangle (\Delta G).$$

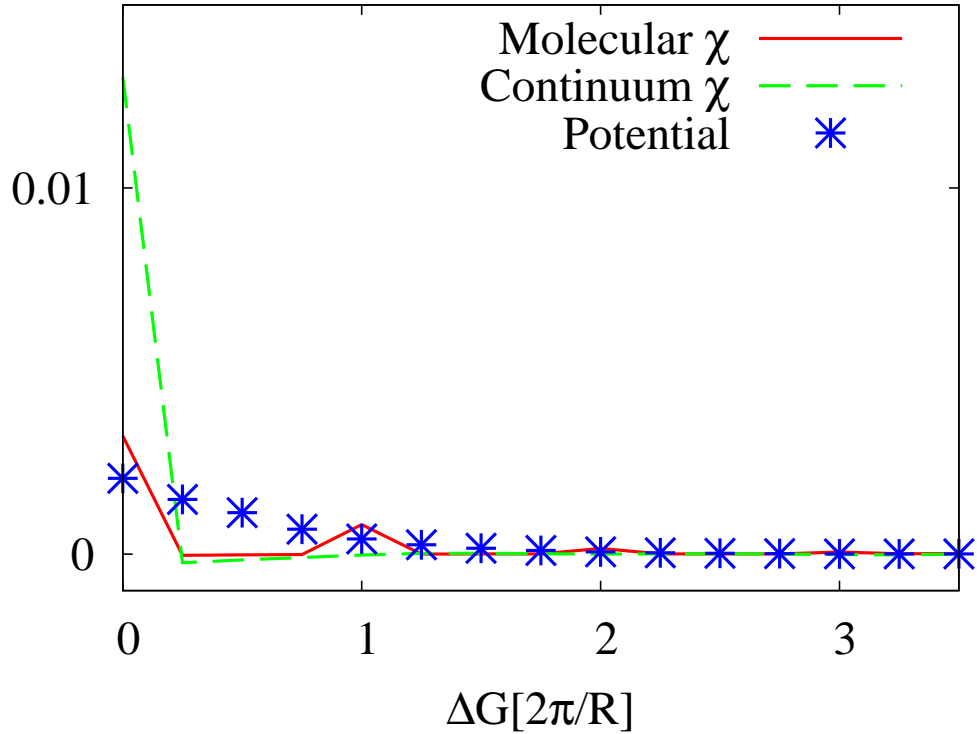


Figure 5.5: Weighted average of solvent response function  $\langle \chi_{env} \rangle$  and potential fluctuation weight  $\langle \phi \rangle$  as a function of momentum transfer  $\Delta G$ : continuum response (green dashed line), molecular response (red line), potential fluctuation weight (blue asterisks).

Figure 5.5 shows the averaged environment response  $\langle \chi_{env} \rangle (\Delta G)$  along with the potential fluctuation weights  $\langle \phi \rangle (\Delta G)$  as functions of  $\Delta G$ . The rapid decrease of the  $\langle \chi_{env} \rangle$  with  $\Delta G$  implies that the solvent effect is dominated by the  $\Delta G = 0$  term, which consists of the diagonal components of the solvent response  $\chi_{env}(G, G)$  and the weights  $\phi(G, \Delta = 0)$ . Figure 5.6, in turn, shows the behavior of these two quantities as functions of  $|G|^2$ . The potential weight factors  $\phi(G, \Delta = 0) \equiv |[V_c \rho]_G|^2$ , decay rapidly with  $G$  (in addition to the natural exponential decay in the density  $\rho_G$ , the two Coulomb factors contribute an additional decay factor  $1/G^4$ ). These results indicate that the solvent effect is governed by the diagonal, small wave-vector (long wave-length) components of

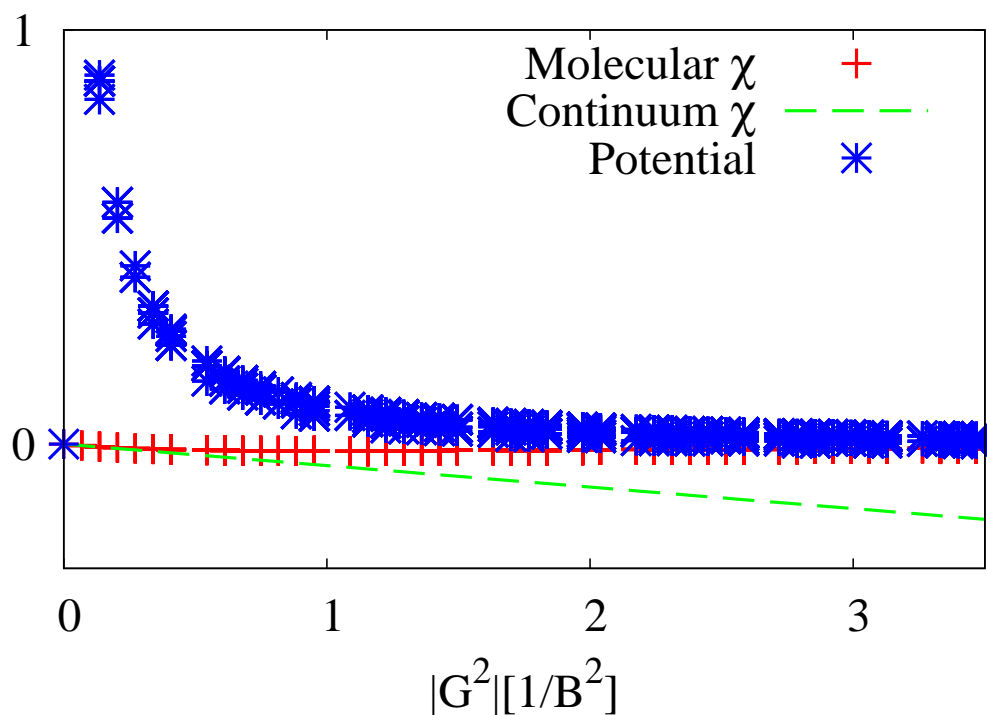


Figure 5.6: Diagonal components of solvent response and weights as functions of  $G^2$ : continuum response (green dashed line), molecular response (red +’s), potential weights (blue asterisks).

the response function, precisely those components at which the continuum and molecular response functions would be expected to most resemble each other. It is this localization of  $[[V_{c\rho}]_G]^2$  to small wave vectors, therefore, that explains the remarkable agreement in the solvent shifts for GW calculations within the two embedding approaches.

Figure 5.7 gives a more detailed view, focused on the relevant region of small wave vectors. The two methods are clearly consistent as  $G \rightarrow 0$ . However, the deviation between the two functions grows continuously with  $G$ . The continuum response, given by the Poisson equation to be  $\chi_{env}(G, G) = -(\epsilon(G = 0) - 1)G \cdot G/4\pi$ , grows linearly with  $|G|^2$ , whereas, the molecular embedding



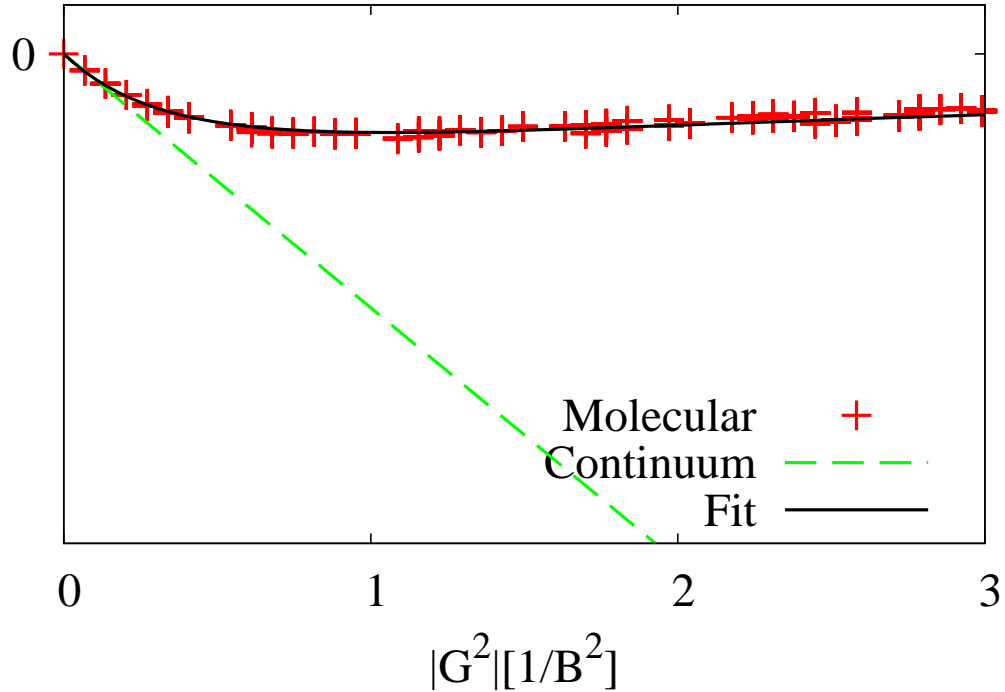


Figure 5.7: Diagonal components of solvent response and weights as functions of  $G^2$ : continuum response (green dashed line), molecular response (red +’s), fit to analytic form (black curve).

response converges to zero for wave vectors corresponding to length scales significantly smaller than the atomic orbitals making up the response function  $\chi_{env}$ . The erroneous divergence of the continuum response at large  $G$ , which ultimately stems from the fact that the description of the dielectric response  $\epsilon(r, r') = \epsilon(r)\delta(r - r')$  is purely local, could contribute significant errors in the GW corrections for systems with more highly localized orbitals, such as transition metals containing the  $d$ -orbitals.

For such systems with highly localized orbitals, the continuum response function  $\chi(G, G')$  can be corrected by replacing the quadratic ( $G^2$ ) dependence with a functional form such as  $(aG/1 + bG^2)^2$ , which is found to fit well to the

Table 5.7: Solvation shifts for individual contributions (DFT and the GW self-energy correction added to the DFT result) and total ionization potential (HOMO level) for H<sub>2</sub>O molecule and embedded in a continuum dielectric, a model molecular crystal (ice Ic), and within a specially constructed non-local dielectric continuum model (New model).

	DFT shift (eV)	GW shift (eV)	Total shift (eV)
Continuum	0.40	1.67	2.07
Molecular	2.18	1.60	3.78
New model	2.18	1.58	3.76

molecular embedding data, as seen in Figure 5.7. The advantage of using this particular functional form, in practice, is that it can be easily incorporated into the continuum Poisson equation as follows,

$$G \cdot \left( \frac{a}{1 + bG^2} \epsilon(G - G', \omega) \frac{a}{1 + bG'^2} \right) G' \phi(G', \omega) = 4\pi\rho(G, \omega), \quad (5.2)$$

where the expression within the large parentheses represents the Fourier transform of a non-local dielectric function,  $\epsilon(r, r') = \int dR f(r - R)\epsilon(R)f(r' - R)$ , where  $f(r)$  is the Fourier transform of  $a/(1 + bG^2)$ , as opposed to the local dielectric function  $\epsilon(r)$  in the standard continuum approach. A non-local continuum theory with this dielectric response then has the correct behavior for the short- and long-wavelength components of  $\chi$  with relevance to GW corrections.

Table 5.7 shows that this new continuum function reduces the discrepancy between the continuum and molecular GW shifts by more than a factor of three, but with almost negligible additional computational cost over the traditional continuum method. In combination with the use of molecular embedding for calculating the equilibrium electronic eigenvalues, this new non-local continuum approach yields solvent shifts significantly closer than traditional continuum methods to Pearson’s estimate of the experimental value!

## 5.8 Summary

We present two methods for calculating the quasiparticle states of solvated systems: the continuum embedding and the molecular embedding. The continuum embedding, which employs a predetermined macroscopic dielectric function for the environment, significantly improves both the solvent shifts and absolute values of the ionization potential for various organic molecules. It also successfully captures the general trend in the ionization potential shift, in which molecules with larger polarizabilities experience larger IP shifts, in a good agreement with Pearson’s estimates based on comparison of molecular and ionic solvation energies. Despite these above successes, the magnitudes of the overall shifts in ionization potentials, even though calculated at the GW level, turn out to be underestimated by about a factor of two, an effect we trace ultimately to the fact that, although the continuum approach captures polarization effects, it misses the potential shifts associated with the local molecular field of the solvent environment.

On the other hand, the molecular embedding method – a combination of the orbital-free embedding for computing the equilibrium state Kohn-Sham orbitals and eigenvalues with a cluster expansion of the microscopic response function for the environment  $\chi_{env}$  – successfully recovers the ionization potential shift by fully taking account the local molecular field effect of the surrounding environment. Surprisingly, for the GW self-energy correction, the continuum method gives results quite close to the molecularly detailed cluster expansion approach. Ultimately, we traced this coincidence to the importance of the long-wavelength, diagonal components of  $\chi_{env}$  in determining the GW correction. Such agreement suggests an efficient hybrid approach to such calculations in

the future, namely using the orbital-free molecular embedding at the DFT level to capture the crystal field effects, and then employing continuum embedding to compute the quasiparticle corrections.

Finally, our identification of the dominant components of  $\chi_{env}$  led to a simple approach for improving the continuum dielectric response at short wavelengths, which allows the molecular-embedded GW correction to be reproduced almost exactly within a non-local continuum dielectric approach.

This initial study, we believe, opens a pathway to the development of efficient excited-state methods for the study of systems in contact with environments such as liquids. Applications of this approach would include the study of solution effects on the spectra of dye molecules and tuning the band gaps of liquid-phase solar cells.

## CHAPTER 6

### SUMMARY/FUTURE WORKS

This thesis presents *ab initio* approaches to efficiently handle atomic subsystems in contact with various extended environments, including both defect-containing crystals and liquid environments. Chapter 2 explores the structural deformations associated with the various Ruddlesden-Popper (RP) phases that result from the presence of stacking faults in complex oxides. To perform this study, we introduced a Ginzburg-Landau Hamiltonian describing the structural phase transition observed in the *ab initio* calculations and with parameters determined from those calculations. This new Hamiltonian allows us to embed the *ab initio* behavior of oxygen-octahedral units into much larger systems by coupling them to elastic fields induced by the planar, stacking-fault defects of each RP phase. Despite its simplicity, this model predicts quantities beyond the computational reach of *ab initio* calculations, including the structural phase transition associated with an isolated stacking fault. This work suggests that such a model Hamiltonian, particularly those with inter-octahedral interactions, can form a fruitful platform for study of nano-structured and superlattice systems in the future. Future work should include generalizing such models to include other order parameters, such as ferro-electricity, to allow exploration of the full range of complex oxides.

Chapter 3 continues our embedding studies in the context of solid-state systems, taking on the difficult challenge of understanding the microscopic origins of two-level centers in a particular class of substitutionally mixed crystalline systems. Our *ab initio* study concluded that such centers arise from structural phase transitions induced by random local chemical strains induced by the

placement of surrounding substitutions. In particular, we found that, in the case of  $\text{Ba}_{1-x}\text{Ca}_x\text{F}_2$ , relatively small fluctuations in local chemical strain induce multiple minimum configurations for “di-substitution” defects (two substitutions occurring on neighboring substitutional sites). Toward confirming these defects as the origin of the observed two-level centers, we then turned to making quantitative predictions of actual observables such as the optical density of states. Making such predictions required again embedding of *ab initio* calculations into a long-range elastic continuum description through a modified Landau Hamiltonian, as direct *ab initio* study of these phenomena would be prohibitive. After determining the parameters of this Hamiltonian through *ab initio* calculations, the combination of a statistical theory for the local strain distribution with the Landau Hamiltonian successfully predicted two key observables in accordance with experiment: both the overall density of active two-level centers, and the distribution of excitation frequencies. Finally, our proposed mechanism, symmetry breaking driven by local strain fluctuations, is sufficiently generic that we believe it should be explored in the future for other systems exhibiting two-level center behavior. Future works should include several more detailed analyses to improve the quantitative predictions of this work, such as the possible contributions from larger defect clusters, or the strain-dependence of the coupling dipole, all of which could improve the quantitative agreement of the absorption spectrum with the experimental observations.

These successes in Chapters 2 and 3 suggest that the combination of *ab initio* calculation with Landau Hamiltonian modeling opens a promising pathway of handling atomic subsystems embedded in solid-state environments with long-range *elastic* interactions. This thesis next turns to the question of embedding where there is a need to couple *ab initio* studies to other types of long-range

interaction, in particular *electrostatic* interactions which can be present even in systems where the environment is not in the solid state. While there have been many previous studies of the coupling of ground-state calculations to dielectric environments, relatively little has been done in the field of excited-state studies. Accordingly, Chapters 4 and 5 explore the coupling of embedding excited state *ab initio* calculations into systems with strong electrostatic interactions.

Specifically, Chapters 4 and 5 develop new methods to apply many-body perturbation theory techniques (specifically, the GW method) to treat excited states for systems with strong electrostatic coupling to their environment. These chapters explore two approaches to the environment, a continuum model and a cluster expansion method, with Chapter 4 laying out the new formal groundwork and Chapter 5 focusing on the target application we have in mind, solvated molecular systems.

We find that the former approach to the coupling, the continuum embedding approach, improves significantly the solvent shifts of the ionization potential of organic molecules. Moreover, for the GW self-energy correction, the continuum approach gives results quite close to the more computationally demanding cluster-expansion approach. We succeeded in tracking down the origin of this somewhat surprising success of the continuum approach to the fact that the long-wavelength, diagonal components of  $\chi_{env}$ , which are reproduced well in the continuum approach, indeed dominate the GW correction, even in the cluster-expansion approach. For the uncorrected Kohn-Sham eigenvalues from density-functional theory, however, the continuum embedding method misses the local molecular field effect of the molecular environment, and consequently, turns out to significantly underestimate the overall solvent shifts. On the other

hand, a relatively computationally simple, orbital-free molecular embedding approach which we describe does capture this field effect quite well.

Finally, based on the discoveries outlined in the previous paragraph, we suggest an efficient hybrid approach to treatment of liquid environments which we recommend be studied more in depth in the future. Specifically, our results indicate that a promising procedure is to use the orbital-free molecular embedding for the density-functional theory parts of the calculation to capture the crystal field effects and, then, to use the continuum embedding approach to calculate the GW corrections. An additional area for future exploration would be to build on our observation that the continuum calculation of the GW corrections can be improved by over a factor of three by employing a relatively simple, non-local model for the dielectric response of the environment. These initial studies of the embedding of excited state calculation, we believe, open a pathway to the development of efficient environment treatments for situations in which the present state-of-the-art PCM+TDDFT method does not work, such as interfacial physics for systems with metal surfaces in contact with liquid solvents.



## BIBLIOGRAPHY

- [1] The LDA overbinding error may lead to an uncertainty in transition points as the AFD rotational instability is known to be overestimated.
- [2] Janaf thermodynamical tables. *J. Phys. Chem. Ref. Data*, 14:Suppl. 1, 1985.
- [3] P. W. Anderson, B. I. Halperin, and C. M. Varma. *Phil. Mag.*, 25:1, 1972.
- [4] C. A. Angell, K. N. Ngai, G. B. McKenna, P. F. McMillan, and S. W. Martin. *Appl. Phys. Rev.*, 88:3113, 2000.
- [5] T. A. Arias, M. C. Payne, and J. D. Joannopoulos. *Phys. Rev. Lett.*, 69:1077, 1992.
- [6] E. J. Baerends, D. E. Ellis, and P. Ros. *Chem. Phys.*, 2:41, 1973.
- [7] G. R. Barsch and J. A. Krumhansl. *Phys. Rev. Lett*, 53:1069, 1984.
- [8] M. Basletic et al. *Nature Material*, 7:621, 2008.
- [9] A. D. Becke. *J. Chem. Phys.*, 98:5648, 1993.
- [10] M. Benoit, M. Pöhlmann, and W. Kob. *Europhys. Lett.*, 82:57004, 2008.
- [11] J. A. Berger, L. Reining, and F. Sottile. *Phys. Rev. B*, 82:041103(R), 2010.
- [12] K. A. Brueckner. *Phys. Rev.*, 100:36, 1955.
- [13] F. Bruneval and X. Gonze. *Phys. Rev. B*, 78:085125, 2008.
- [14] F. Bruneval, N. Vast, and L. Reining. *Phys. Rev. B*, 74:045102, 2006.
- [15] Z.-L. Cai, K. Sendt, and J. R. Reimers. *J. Chem. Phys.*, 117:5543, 2002.
- [16] E. Cancs, B. Mennucci, and J. Tomasi. *J. Chem. Phys.*, 107:3032, 1997.
- [17] C. R. A. Catlow, J. D. Comins, F. A. Germano, R. Tharley, and W. Hayes. *J. Phys. C*, 11:3197, 1978.
- [18] J. R. Chelikowsky and M. L. Cohen. *Phys. Rev. B*, 14:556, 1976.

- [19] Y. Q. Cheng, E. Ma, and H. W. Sheng. *Phys. Rev. Lett.*, 102:245501, 2009.
- [20] M. Cobb, D. A. Drabold, and R. L. Cappelletti. *Phys. Rev. B*, 54:12162, 1996.
- [21] M. Cossi and V. Barone. *J. Chem. Phys.*, 115:4708, 2001.
- [22] M. Cossi, N. Rega, G. Scalmani, and V. Barone. *J. Comp. Chem.*, 24:669, 2003.
- [23] G. Csanyi, S. Ismail-Beigi, and T. A. Arias. *Phys. Rev. Lett.*, 80:3984, 1998.
- [24] J. Deslippe, G. Samsonidze, D. A. Strubbe, M. Jain, M. L. Cohen, and S. G. Louie. *Comput. Phys. Commun.*, 183:1269, 2012.
- [25] S. V. Faleev, M. van Schilfgaarde, and T. Kotani. *Phys. Rev. Lett.*, 93:126406, 2004.
- [26] C. J. Fennie and K. M. Rabe. *Phys. Rev. B*, 68:184111, 2003.
- [27] S. A. FitzGerald, J. A. Campbell, and A. J. Sievers.
- [28] F. Floris, M. Persico, A. Tani, and J. Tomasi. *Chem. Phys. Lett.*, 199:518, 1992.
- [29] T. L. Fonseca, K. Coutinho, and S. Canuto. *Chem. Phys.*, 349:109, 2008.
- [30] W. M. C. Foulkes, L. Mitas, R. J. Needs, and G. Rajagopal. *Rev. Mod. Phys.*, 73:33, 2001.
- [31] H. P. R. Frederikse and W. R. Hosler. *Physical Review*, 158:775, 1967.
- [32] C. Friedrich, M. C. Müller, and Stefan Blügel. *Phys. Rev. B*, 83:081101(R), 2011.
- [33] V. Garbuio, M. Cascella, L. Reining, R. Del Sole, and O. Pulci. *Phys. Rev. Lett.*, 97:137402, 2006.
- [34] A. M. Glazer. *Acta Cryst.*, B28:3384, 1972.
- [35] R. W. Godby, M. Schluter, and L. J. Sham. *Phys. Rev. B*, 37:10159, 1988.

- [36] M. Grätzel. *J. Photochem. Photobiol. A: Chem.*, 164:3, 2004.
- [37] C. Gros and R. Valenti. *Phys. Rev. B*, 48:418, 1993.
- [38] J. H. Haeni et al. *Nature*, 430:758, 2004.
- [39] P. H. Hahn, W. G. Schmidt, K. Seio, M. Preuss, F. Bechstedt, and J. Bernholc. *Phys. Rev. Lett.*, 94:037404, 2005.
- [40] L. Hedin. *Phys. Rev.*, 139:A796, 1965.
- [41] L. Hedin and S. Lundqvist. *Solid State Phys.*, 23:1, 1969.
- [42] A. Hermann, W. G. Schmidt, and P. Schwerdtfeger. *Phys. Rev. Lett.*, 100:207403, 2008.
- [43] A. Heuer. *Phys. Rev. Lett.*, 78:4051, 1997.
- [44] P. Hohenberg and W. Kohn. *Phys. Rev.*, 136:B864, 1964.
- [45] M. S. Hybertsen and S. G. Louie. *Phys. Rev. B*, 34:5390, 1986.
- [46] M. S. Hybertsen and S. G. Louie. *Phys. Rev. B*, 35:5585, 1987.
- [47] K. Ishida et al. *Nature*, 396:658, 1998.
- [48] S. Ismail-Beigi and T. A. Arias. *Computer Physics Communications*, 128:1, 2000.
- [49] S. Ismail-Beigi and T. A. Arias. *Phys. Rev. Lett.*, 84:1499, 2000.
- [50] S. Ismail-Beigi and S. G. Louie. *Phys. Rev. Lett.*, 90:076041, 2003.
- [51] S. Ispas, M. Benoit, P. Jund, and R. Jullien. *Phys. Rev. B*, 64:214206, 2001.
- [52] K. Johnston, X. Huang, J. B. Neaton, and K. M. Rabe. *Phys. Rev. B*, 71:100103(R), 2005.
- [53] L. Kleinman and D. M. Bylander. *Phys. Rev. Lett.*, 48:1425, 1982.
- [54] P. J. Knowles, C. Hampel, and H.-J. Werner. *J. Chem. Phys.*, 99:5219, 1993.

- [55] W. Kohn and L. J. Sham. *Phys. Rev.*, 140:A1133, 1965.
- [56] C. S. Koonce et al. *Physical Review*, 163:380, 1967.
- [57] S. Lebeque, B. Arnaud, M. Alouani, and P. E. Bloechl. *Phys. Rev. B*, 67:155208, 2003.
- [58] Y. L. Li et al. *Phys. Rev. B*, 73:184112, 2006.
- [59] G. V. Lier, C. V. Alsenoy, V. V. Doren, and P. Geerlings. *Chem. Phys. Lett.*, 326:181, 2000.
- [60] J. Lischner and T. A. Arias. *Phys. Rev. B*, 84:125143, 2011.
- [61] X. Liu, P. D. Vu, R. O. Pohl, F. Schiettekatte, and S. Roorda. *Phys. Rev. Lett.*, 81:3171, 1998.
- [62] S. G. Louie, S. Froyen, and M. L. Cohen. *Phys. Rev. B*, 26:1738, 1982.
- [63] R. M. Martin. *Electronic Structure: Basic Theory and Practical Methods*. Cambridge University Press, 2004.
- [64] L.-M. Martinez and C. A. Angell. *Nature*, 410:663, 2001.
- [65] J. C. Mauro and R. J. Loucks. *Phys. Rev. E*, 78:021502, 2008.
- [66] M. Micoulaut, Y. Guissani, and B. Guillot. *Phys. Rev. E*, 73:031504, 2006.
- [67] H. J. Monkhorst and J.D. Pack. *Phys. Rev. B*, 13:5188, 1976.
- [68] M. Musia and R. J. Bartlett. *Chem. Phys. Lett.*, 384:210, 2004.
- [69] H. Nakatsuji. *Chem. Phys. Lett.*, 59:362, 1978.
- [70] S. M. Nakhmanson. *Phys. Rev. B*, 78:064107, 2008.
- [71] S. M. Nakhmanson, K. M. Rabe, and D. Vanderbilt. *Phys. Rev. B*, 73:060101(R), 2006.
- [72] V. N. Nemykin, E. A. Makarova, J. O. Grosland, R. G. Hadt, and A. Y. Kuposov. *Chem. Phys.*, 349:109, 2008.

- [73] C. I. Nicholls, L. N. Yadon, D. G. Haase, and M. S. Conradi. *Phys. Rev. Lett.*, 59:1317, 1987.
- [74] A. Gaita-Ari no and M. Schechter. *Phys. Rev. Lett.*, 107:105504, 2011.
- [75] B. O'Regan and M. Grätzel. *Nature*, 353:737, 1991.
- [76] N. D. Orloff et al. *Appl. Phys. Lett.*, 94:042908, 2009.
- [77] M. C. Payne et al. *Rev. Mod. Phys.*, 64:1045, 1992.
- [78] R. G. Pearson. *J. Am. Chem. Soc.*, 108:6109, 1986.
- [79] J. P. Perdew. *Phys. Rev. B*, 33:8822, 1986.
- [80] J. P. Perdew, J. A. Chevary, S. H. Vosko, K. A. Jackson, M. R. Pederson, D. J. Singh, and C. Fiolhais. *Phys. Rev. B*, 46:6671, 1992.
- [81] J. P. Perdew and A. Zunger. *Phys. Rev. B*, 23:5048, 1981.
- [82] S. A. Petrosyan, A. A. Rigos, and T. A. Arias. *J. Phys. Chem. B*, 109:15436, 2005.
- [83] W. A. Phillips. *Rep. Prog. Phys.*, 50:1657, 1987.
- [84] W. E. Pickett. *Chem. Phys. Rep.*, 9:115, 1989.
- [85] G. D. Purvis and R. J. Bartlett. *J. Chem. Phys.*, 76:1910, 1982.
- [86] A. M. Rappe, K. M. Rabe, E. Kaxiras, and J. D. Joannopoulos. *Phys. Rev. B*, 41:1227, 1990.
- [87] P. J. Reynolds, D. M. Ceperley, B. J. Alder, and W. A. Lester. *J. Chem. Phys.*, 77:5593, 1982.
- [88] M. Rohlfing and S. G. Louie. *Phys. Rev. B*, 62:4927, 2000.
- [89] S. N. Ruddlesden and P. Popper. *Acta Cryst.*, 10:538, 1957.
- [90] R. Rulis, J. Chen, L. Ouyang, W.-Y. Ching, X. Su, and S. H. Garofalini. *Phys. Rev. B*, 71:235317, 2005.

- [91] J. Sarnthein, A. Pasquarello, and R. Car. *Phys. Rev. B*, 52:12690, 1995.
- [92] S. Sastry, P. G. Debenedetti, and F. H. Stillinger. *Nature*, 393:554, 1998.
- [93] K.-P. Schröder and J. Sauer. *J. Phys. Chem.*, 100:11043, 1996.
- [94] J. P. Sethna and K. S. Chow. *Phase Transit.*, 5:317, 1985.
- [95] B.-C. Shih, Y. Xue, P. Zhang, M. L. Cohen, and S. G. Louie. *Phys. Rev. Lett.*, 105:146401, 2010.
- [96] C.-K. Skylaris, P. D. Haynes, A. A. Mosto, and M. C. Payne. *J. Chem. Phys.*, 122:084119, 2005.
- [97] J. C. Slater. *Phys. Rev.*, 81:385, 1951.
- [98] J. M. Soler, E. Artacho, J. D. Gale, A. Garcia, J. Junquera, P. Ordejón, and D. Sánchez-Portal. *J. Phys.: Condens. Matter*, 14:2745, 2002.
- [99] J. Sponer and P. Hobza. *J. Phys. Chem.*, 98:3161, 1994.
- [100] R. Sundararaman, K. Letchworth-Weaver, and T. A. Arias. <http://jdftx.sourceforge.net>.
- [101] I. Tamblyn, P. Darancet, S. Y. Quek, S. A. Bonev, and J. B. Neaton. *Phys. Rev. B*, 84:201402(R), 2011.
- [102] W. Tian, X. Q. Pan, J. H. Haeni, and D. G. Schlom. *J. Mater. Res.*, 16:2013, 2001.
- [103] J. Tomasi, B. Mennucci, and E. Cancès. *J. Mol. Struct: THEOCHEM*, 464:211, 1999.
- [104] K. A. Topp, E. Thompson, and R. O. Pohl. *Phys. Rev. B*, 60:898, 1999.
- [105] R. E. Tribble, J. D. Cossairt, K. I. Kubo, and D. P. May.
- [106] H. Üstünel, D. Roundy, and T. A. Arias. *Phys. Rev. Lett.*, 94:025503, 2005.
- [107] M. van Schilfhaarde, T. Kotani, and S. Faleev. *Phys. Rev. Lett.*, 96:226402, 2006.

- [108] M. P. Warusawithana et al. *Science*, 324:367, 2009.
- [109] T. A. Wesolowski and A. Warshel. *J. Phys. Chem.*, 97:8050, 1993.
- [110] J. P. Wrubel et al. *Phys. Rev. Lett*, 96:235503, 2006.
- [111] H. Zhang, C.-X. Liu, X.-L. Qi, X. Dai, Z. Fang, and S.-C. Zhang. *Nature Phys.*, 5:438, 2009.
- [112] H.-J. Zhang, C.-X. Liu, X.-L. Qi, X.-Y. Deng, X. Dai, S.-C. Zhang, and Z. Fang. *Phys. Rev. B*, 80:085307, 2009.

## APPENDIX A

### TWO-LEVEL STATES HAMILTONIAN CONSTRUCTION

In Section 3.7 we introduced a free energy model Hamiltonian describing the spectral properties of di-substitution defects under the isotropic strain:  $\epsilon_{ii} = \epsilon_n, \epsilon_{i \neq j} = \epsilon_s$ . In this Appendix, we present detailed derivations for the spectral properties from the model Hamiltonian, and extend our model to include non-isotropic strain.

Full exploration within density-functional theory of the effects of strain with variations in all tensor components is extremely demanding computationally. Therefore, we employ our empirical potential model to explore the phase space more efficiently. Although the specific numerical results we obtain may not be reliable because they depend on the details of the interatomic forces, the analytic structure of the energy surface with varying strain depends not upon these details, but upon the symmetries of the system. Our aim, therefore, is to determine this analytic structure from the interatomic potential calculations, but then to calculate the relevant parameters *ab initio*.

To lowest relevant order, the Landau Hamiltonian satisfying inversion symmetry  $\vec{r} \leftrightarrow -\vec{r}$ , or, more specifically,  $(\epsilon_s, q) \leftrightarrow (-\epsilon_s, -q)$  and  $(\epsilon_s = 0, q) \leftrightarrow (-\epsilon_s = 0, -q)$  for shear strain  $\epsilon_s$  and order parameter  $q$ , has the following form

$$\begin{aligned} F(q) &= F_0(q) + \beta_s \epsilon_s q + O(\epsilon_s^{5/2}), \\ F_0(q) &= \frac{1}{4} A q^4 + \frac{1}{2} \gamma (\epsilon_c - \epsilon_n) q^2. \end{aligned} \tag{A.1}$$

Assuming sufficiently small shear strain, the solution  $q$  minimizing the free energy can be written in a series in terms of the shear strain at first order,



$q = q_0 + \epsilon_s \delta q$ , where  $q_0 = \sqrt{\gamma(\epsilon_n - \epsilon_c)/A}$  is the solution for the Hamiltonian for shear strain  $\epsilon_s = 0$ . To see this, we minimize the full Hamiltonian by setting its derivative to zero,

$$\begin{aligned} \frac{\partial F}{\partial q} \Big|_q &= \frac{\partial F_0}{\partial q} \Big|_{q_0} + \frac{\partial^2 F_0}{\partial q^2} \Big|_{q_0} \delta q + \beta_s \epsilon_s O(\epsilon_s^2) = 0 \\ &= \delta q [3Aq_0^2 + \gamma(\epsilon_c - \epsilon_n)] + \beta_s \epsilon_s + O(\epsilon_s^2), \end{aligned} \quad (\text{A.2})$$

which leads to the correction in  $q$ ,

$$\delta q = \beta_s \epsilon_s / (3Aq_0^2 + \gamma(\epsilon_c - \epsilon_n)) = \beta_s \epsilon_s / 2Aq_0^2, \quad (\text{A.3})$$

where  $Aq_0^2 = \gamma(\epsilon_n - \epsilon_c)$  is used in the last step. The resulting energy asymmetry  $\Delta$  can be obtained similarly,

$$\begin{aligned} \Delta(\epsilon_n, \epsilon_c) &= F(q) - F(-q) \\ &= F_0(q_0) + \frac{\partial F_0}{\partial q} \Big|_{q_0} \delta q + \beta_s \epsilon_s q_0 - \left( F_0(q_0) - \frac{\partial F_0}{\partial q} \Big|_{q_0} \delta q - \beta_s \epsilon_s q_0 \right) \\ &= 2\beta_s \epsilon_s q_0, \end{aligned} \quad (\text{A.4})$$

employing  $\frac{\partial F_0}{\partial q} \Big|_{q_0} = 0$ .

The above derivation is valid only when the shear  $\epsilon_{i \neq j} = \epsilon_s$  and normal  $\epsilon_{i=j} = \epsilon_n$  components of the strain tensor each have identical values so that shear and normal strain can each be single variables  $\epsilon_s$  and  $\epsilon_n$ , respectively. Let us now consider the general case where each independent component of the strain tensor has a different value,

$$\epsilon = \begin{pmatrix} \epsilon_{xx} & \epsilon_{xy} & \epsilon_{xz} \\ \epsilon_{xy} & \epsilon_{yy} & \epsilon_{yz} \\ \epsilon_{xz} & \epsilon_{yz} & \epsilon_{zz} \end{pmatrix}. \quad (\text{A.5})$$

One should expect, and our numerical interatomic potential calculations confirm, that the coupling strength of each strain tensor component depends

strongly on the defect geometry. In the fluorite lattice, neighboring cation sites are separated by  $\langle 110 \rangle$  directions that are contained in one of the  $xy$ ,  $xz$  or  $yz$  coordinate planes, leaving the third (perpendicular) direction ( $z$ ,  $y$ ,  $x$ , respectively) uniquely determined by the symmetry of the defect. Indeed, we find that the coupling to the diagonal (“normal”) strain component in the third direction is very weak. Similarly, shear strains in the corresponding coordinate plane couple only weakly to the defect. In this initial analysis, we ignore these weakly coupled components to make our model simple and only consider the effects of the remaining components. For example, in the case of a di-substitution oriented along the  $[110]$  direction (selecting the “xy” plane), the important components which we consider for the strain tensor are  $\epsilon_{xx}$ ,  $\epsilon_{yy}$ ,  $\epsilon_{xz}$ , and  $\epsilon_{yz}$ .

Focusing on these components, Figure A.1 shows a contour plot of the height of the tunneling barrier for a di-substitution defect as a function of both of the relevant normal components of strain we consider. Interestingly, the contours are nearly circular, indicating that the barrier seems to depend only on the root-mean-square of the two strain components, specifically in the form  $(\epsilon_{xx} - \epsilon_c)^2 + (\epsilon_{yy} - \epsilon_c)^2$ . These results are fully consistent with two independent degrees of freedom contributing to the underlying Landau Hamiltonian in the forms,

$$\begin{aligned} F_1(q_1) &= \frac{1}{4}Aq_1^4 + \frac{1}{2}\gamma(\epsilon_c - \epsilon_{xx})q_1^2 + \eta q_1 q_2 \\ F_2(q_2) &= \frac{1}{4}Aq_2^4 + \frac{1}{2}\gamma(\epsilon_c - \epsilon_{yy})q_2^2 + \eta q_1 q_2, \end{aligned} \quad (\text{A.6})$$

where  $\eta q_1 q_2$  represents coupling between two order parameters  $q_1$  and  $q_2$ . Assuming that this coupling strength is sufficiently smaller than the deformation instability, the minima for each equation becomes simply  $q_1 = \pm q_1^0 - \eta q_2^0 / 2\beta(\epsilon_{xx} - \epsilon_c)$ ,  $q_2 = \pm q_2^0 - \eta q_1^0 / 2\beta(\epsilon_{yy} - \epsilon_c)$ , where  $q_i^0 = \sqrt{\beta(\epsilon_i - \epsilon_c)/A}$ , and the resulting barrier is  $V = -\frac{1}{4}\beta[(\epsilon_{xx} - \epsilon_c)^2 + (\epsilon_{yy} - \epsilon_c)^2] + \eta \frac{\beta}{A} \sqrt{(\epsilon_{xx} - \epsilon_c)(\epsilon_{yy} - \epsilon_c)}$ , which well

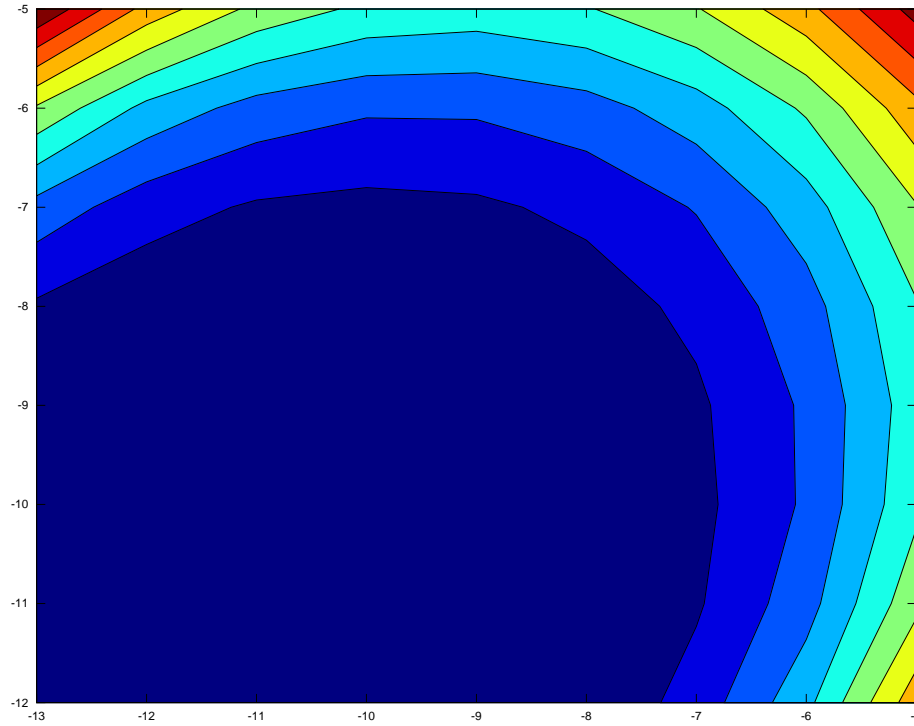


Figure A.1: Contour plot of the tunneling barrier associated with a di-substitution defect as a function of the two relevant diagonal components of the strain tensor, those in directions with projections along the line connecting the two substitutions.

agree to our interatomic potential results.

We have also explored the behavior of the asymmetry  $\Delta$  for the relevant shear components of the strain tensor, those whose plane does not contain the line connecting the two substitutions. Figure A.2 displays the contour plot of resulting asymmetry, which exhibits perfect linear dependence between the two components, *i.e.*,  $\Delta \propto \sum_{ij} \epsilon_{ij}$ .

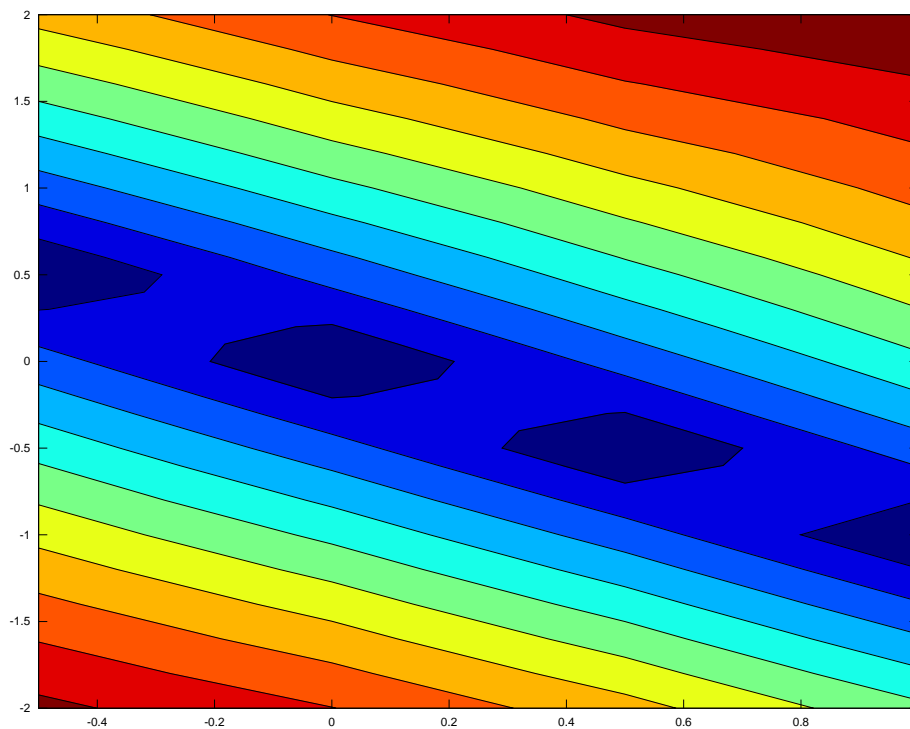


Figure A.2: Contour plot of the asymmetry  $\Delta$  (energies difference between minima) for a di-substitution defect as a function of the two relevant shear components of the strain tensor, those which do not contain the line connecting the two substitutions.

APPENDIX B  
FREQUENCY INTEGRAL OF GW METHOD

In this chapter we present a detailed procedure to evaluate the frequency integral in the GW method. The self-interaction kernel in the GW approximation is written as following:

$$\Sigma(E) = \frac{i}{2\pi} \int d\omega e^{-i\delta\omega} G(E - \omega)W(\omega), \quad (\text{B.1})$$

where  $\delta = 0^+$ ,  $G$  is single electron Green's function, and  $W$  is the screened Coulomb interaction. This integral is a major bottleneck in the entire GW method, because one should compute  $W$  for many points  $\omega$  as  $W$  is rather ragged along real axis with lots of singularities. One of the common approaches to avoid this bottleneck is to assume that the dynamic dependence of the charge response resembles that of the uniform electron gas, or the plasmon, and to construct dynamic part of  $W$  from the the plasmon spectrum[45]. This approach, named as the plasmon pole approximation, has been very successful for many semiconducting materials, however, the plasmon could not be assumed for localized systems including isolated molecules we consider in this work. Instead, we use the contour deformation techniques[57, 35], which obtains the integration as contributions from the poles of Green's function and an integral along imaginary axis, along which  $\tilde{W}$  is analytic and thus needed to be evaluated at a few points.

The integration procedure starts with separating dynamic and static components of the screened Coulomb interaction in Eq. B.1 as  $W(\omega) = V_c + \tilde{W}(\omega)$ , and the self-energy kernel  $\Sigma(\omega) = \Sigma_X + \Sigma_C(\omega)$ . The static component of the self-energy kernel  $\Sigma_X$  is contributed by electrons interacting with themselves

through bare Coulomb potential  $V_c$  and evaluated for  $n$ -th orbital as following:

$$\begin{aligned} \langle n | \Sigma_X | n \rangle &= \frac{i}{2\pi} \int d\omega e^{-i\delta\omega} \sum_G \sum_m \frac{1}{E - \omega - \epsilon_m - i\delta_m} \langle nm | V_c | mn \rangle \\ &= - \sum_m^{occ} \langle nm | V_c | nm \rangle \equiv - \frac{1}{\Omega} \sum_m^{occ} \sum_G |M_G^{nm}|^2 V_c(G), \end{aligned} \quad (\text{B.2})$$

where  $|nm\rangle = \psi_n^* \psi_m$ ,  $M_G^{nm} = \int e^{-iG \cdot r} \psi_n^*(r) \psi_m(r)$ , and ‘‘occ’’ refers to the group of occupied states. The second term  $\Sigma_C$  represents the frequency-dependent contribution of self-energy and written as:

$$\langle n | \Sigma_C(E) | n \rangle = \frac{1}{\Omega} \sum_{GG'} \sum_m [M_G^{nm}]^* M_{G'}^{nm} C_{GG'}^m(E) \quad (\text{B.3})$$

with the frequency integral term as

$$C_{GG'}^m(E) = \frac{i}{2\pi} \int_{-\infty}^{\infty} d\omega \frac{\tilde{W}_{GG'}(\omega)}{E - \omega - \epsilon_m + i\delta \text{sgn}[\epsilon_m - \mu]}, \quad (\text{B.4})$$

where  $\tilde{W}_{GG'} = (W - V_c)_{GG'}$  is the difference between the screened Coulomb and the bare Coulomb interaction in Fourier representation.

We obtain the dynamic charge response function  $\chi(\omega)$  from time-dependent perturbation theory[46] as the following form,

$$\begin{aligned} \chi(r, r'; \omega) &= \psi_c^*(r) \psi_v(r) \psi_v^*(r') \psi_c(r') \left( \frac{1}{\omega + \epsilon_v - \epsilon_c - i\delta} - \frac{1}{\omega - \epsilon_v + \epsilon_c + i\delta} \right) \\ &= \psi_c^*(r) \psi_v(r) \psi_v^*(r') \psi_c(r') \frac{2(\epsilon_v - \epsilon_c)}{(\epsilon_v - \epsilon_c)^2 - \omega^2}, \end{aligned} \quad (\text{B.5})$$

where the dynamic response  $\chi(\omega)$  rapidly decays as  $1/\omega^2$ . This decay results in  $\tilde{W}(\omega)$  to converge  $\propto 1/\omega^2$  for large enough  $|\omega|$ , which allows us handle the tedious singularities of  $\tilde{W}$  along the real axis by deforming the integration axis from the real axis to imaginary axis. In practice, we employ the contour deformation trick developed by Lebegue and coworkers[57], who split the integral as contributions from the poles of Green’s function and an integral along imaginary axis. The contributions from the Green’s function are obtained as a sum

over residues for poles located between  $E$  and  $\mu$ , *i.e.*,

$$\begin{aligned} & \sum_n \tilde{W}_{GG'}(E - \epsilon_n), E > \epsilon_n > \mu, \text{ if } E > \mu \\ & - \sum_n \tilde{W}_{GG'}(E - \epsilon_n), E < \epsilon_n < \mu, \text{ if } E < \mu. \end{aligned} \quad (\text{B.6})$$

To practically evaluate  $\tilde{W}$  at various frequencies, we first explicitly compute  $\tilde{W}$  on a given mesh of frequencies from 0 to  $\epsilon_c - \epsilon_v$ , in which  $\tilde{W}$  is analytic, fit them to a polynomial function, and use the polynomial function to evaluate. The integral part along imaginary axis is written as

$$\begin{aligned} C_{GG'}^m(E) &= \frac{i}{2\pi} \int_{-i\infty}^{i\infty} dz \frac{\tilde{W}_{GG'}(z)}{E - z - \epsilon_m + i\delta \text{sgn}[\epsilon_m - \mu]} \\ &= -\frac{1}{2\pi} \int_{-\infty}^{\infty} dz \frac{\tilde{W}_{GG'}(iz)}{E - iz - \epsilon_m + i\delta \text{sgn}[\epsilon_m - \mu]}, \end{aligned} \quad (\text{B.7})$$

where  $\tilde{W}(iz)$  is analytically continued  $\tilde{W}(\omega)$  at complex frequency  $iz$ . The analytic continuation technique is first applied to the dynamic charge response function in Eq. B.5 for which we know the analytic form as following,

$$\chi(i\omega) = \frac{2(\epsilon_v - \epsilon_c)}{(\epsilon_v - \epsilon_c)^2 + \omega^2}, \quad (\text{B.8})$$

which leads to the analytically continued  $\tilde{W}(iz) = (\chi(iz)^{-1} - V_c)^{-1} - V_c$ .

Since only the real part of self interaction  $\Sigma$  contributes to the quasiparticle energy (the imaginary part is the quasiparticle lifetime), we take the real part of the above integration, which, using the time-reversal symmetry  $\tilde{W}(iz) = \tilde{W}(-iz)$ , is written as following:

$$\begin{aligned} \text{Re}[C_{GG'}^m(E)] &= -\frac{1}{2\pi} \int_{-\infty}^{\infty} dz \frac{(E - \epsilon_m)\tilde{W}_{GG'}(iz)}{(E - \epsilon_m)^2 + z^2} \\ &= -\frac{1}{2\pi} \int_0^{\infty} dz \frac{2(E - \epsilon_m)\tilde{W}_{GG'}(iz)}{(E - \epsilon_m)^2 + z^2}, \end{aligned} \quad (\text{B.9})$$

The integration could be numerically evaluated using standard interpolation

techniques such as Gaussian quadrature[57], or even more simplified in the following form:

$$Re[C_{GG'}^m(E)] = -\frac{1}{\pi} \int_0^{\pi/2} du \tilde{W}_{GG'}(i(E - \epsilon_m) \tan(u)), \quad (\text{B.10})$$

where we used change of a variable  $\tan(u) = z/(E - \epsilon_m)$ .

Finally, we explicitly construct  $\tilde{W}(iz)$  along imaginary frequency axis from  $z = 0$  up to 5eV at 30 nonuniform grid points, and used its polynomial fit to re-evaluate the integrand at uniform  $u$  grids. Figure B.1 shows the explicit data and its polynomial fit on  $u$ -axis, which monotonically decreases and thus is easily integrable. As the imaginary frequency  $iz$  goes to infinite,  $u \rightarrow \pi/2$ , the screening rapidly converges to zero, as expected.



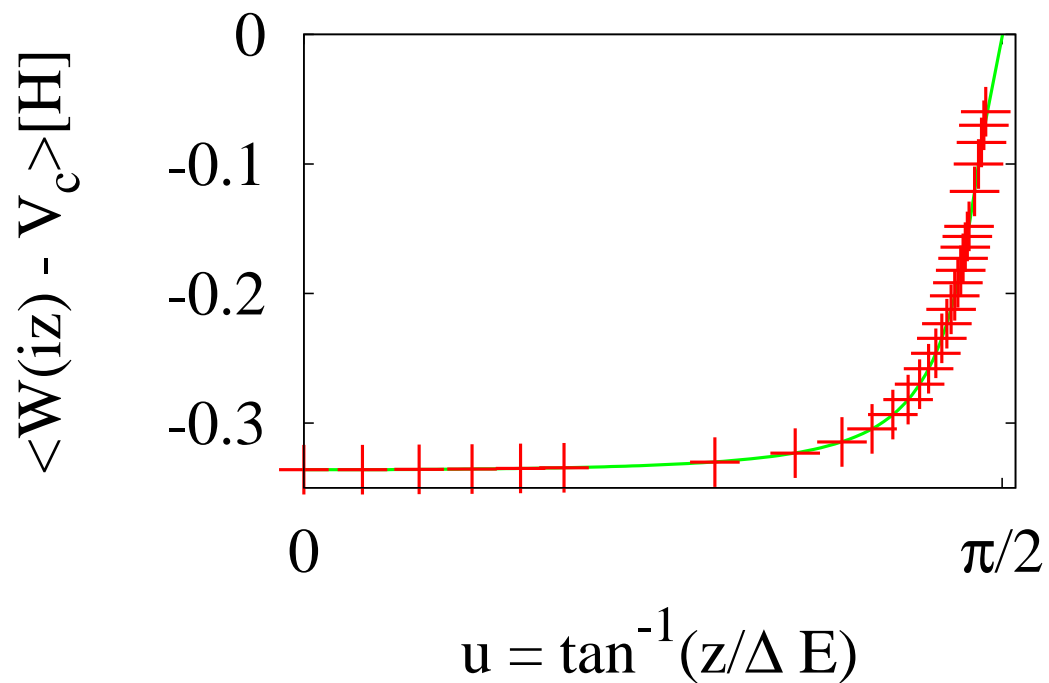


Figure B.1: The screened Coulomb energy between the highest occupied orbitals –  $\langle nm|\tilde{W}(iz)|nm \rangle$  with  $n$  and  $m$  are HOMO – for  $\text{H}_2\text{O}$  molecule embedded in ice crystal as a function of the rescaled imaginary frequency  $u = \tan^{-1}(z/(E - \epsilon_m))$ : explicit data (crosses), polynomial fit to data (green line).